Network Modeling of Motor Pathways from Neural Recordings

by

Geoffrey Newman

A dissertation submitted to The Johns Hopkins University in conformity with the requirements for the degree of Doctor of Philosophy.

Baltimore, Maryland

September, 2016

Abstract

During cued motor tasks, for both speech and limb movement, information propagates from primary sensory areas, to association areas, to primary and supplementary motor and language areas. Through the recent advent of high density recordings at multiple scales, it has become possible to simultaneously observe activity occurring from these disparate regions at varying resolution. Models of brain activity generally used in brain-computer interface (BCI) control do not take into account the global differences in recording site function, or the interactions between them. Through the use of connectivity measures, however, it has been made possible to determine the contribution of individual recording sites to the global activity, as they vary with task progression.

This dissertation extends those connectivity models to provide summary information about the importance of individual sites. This is achieved through the application of network measures on the adjacency structure determined by connectivity measures. Similarly, by analyzing the coordinated activity of all of the electrode sites simultaneously during task performance, it is possible to elucidate discrete functional units through clustering analysis of the electrode recordings.

In this dissertation, I first describe a BCI system using simple motor movement imagination at single recording sites. I then incorporate connectivity through the use of TV-DBN modeling on higher resolution electrode recordings, specifically electrocorticography (ECoG). I show that PageRank centrality reveals information about task progression and regional specificity which was obscured by direct application of the connectivity measures, due to the combinatorial increase in feature dimensionality. I then show that clustering of ECoG recordings using a method to determine the inherent cluster count algorithmically provides insight into how network involvement in task execution evolves, though in a manner dependent on grid coverage. Finally, I extend clustering analysis to show how individual neurons in motor cortex form distinct functional communities. These communities are shown to be task-specific, suggesting that neurons can form functional units with distinct neural populations across multiple recording sites in a context dependent impermanent manner.

This work demonstrates that network measures of connectivity models of neurophysiological recordings are a rich source of information relevant to the field of neuroscience, as well as offering the promise of improved degree-of-freedom and naturalness possible through direct BCI control. These models are shown to be useful at multiple recording scales, from cortical-area level ECoG, to highly localized single unit microelectrode recordings.

Primary Reader: Nitish Thakor

Secondary Reader: Nathan Crone

Acknowledgments

I would like to express my gratitude for my advisor, Dr. Nitish Thakor, and my thesis committee members, Dr. Nathan Crone and Ernst Niebur. Without your support and mentorship through the years, I would never have been able to accomplish what I have during my PhD.

I would like to thank the labmates through the years who have made working on my PhD a far more enjoyable experience than it should be. Vikram, Mohsen, Abhishek and Kartik helped me navigate the beginning of my Ph.D., and learn how to dive into research. Ryan, Heather, Elliot, Matt F, Kyle and Guy have all helped me develop my outlandish ideas into decent research directions. Griff, Yujing, Luke, Mike and Miaomiao have all provided fresh perspectives, and pleasant conversation. I'd like to give Ryan a second mention for introducing me to data science, and keeping a finger on the pulse of what's hot in industry. If not for him, I would have no hope in my search for a great career.

My appreciation also goes to those I've met during my time in Baltimore, for they've given me a more broad perspective of what life can be like outside of NYC. My old roommates: Catherine (Teng-Teng), Nam, Chris, Mike, and Eric have all been fun to hang out with in and outside the house. The BAD (Baltimore Anime Denizens): Phoebe, Charles, Jessie, Cara, Adam, and Chris have been great to hang out with at Otakon, and to talk about my hobbies with.

I'd also like to thank my friends from High School and Junior High School who've stuck around despite my inability to keep up contact: Lucy, Sandra, Karl, Aurelio, Joann, Jimmy and Gifta, just to name a few. It's always great to reminisce with them, or just hear about how things are going in the Big Apple.

My siblings Marc, Jessica, Joshua and Eric are fun to play video games with or watch a movie whenever I'm in the city. My nephews who, despite being several states away, contribute substantially to my upbeat mood: Orion, Aidan and Adrian. All of my family is in NYC, making it very convenient to see them all around holidays.

Lastly, I'd like to thank my parents Charmaine and Barry are as supportive and nonjudgmental as any I've known. There generosity and love has helped guide me through life. Now that I'm finishing my Ph.D., I hope to move nearer to them!

Dedication

To my nephews: Orion, Aidan and Adrian. It's amazing watching them learn to navigate through the world, and delight in all the things which I take for granted. Thanks for always putting a smile on my face.

Contents

3 Cerebellar ataxia patients are able to use motor imagery to modulate mu-band power in a pilot study of EEG-based brain-computer interface control 41

List of Tables

List of Figures

Chapter 1

Background and Motivation

1.1 Motivation

1.1.1 Problem Statement

It is estimated that the number of people in the United States in 2013 with spinal cord injuries (SCI) is between 238,000 and 332,000, with as much as 40% of the cases being a result of car accidents [Center et al., 2013]. Of these patients, the majority suffer from tetraplegia, and lose control of their limbs, as well as sensory afferents. Most of the remaining patients suffer from paraplegia, with a loss of control of their lower limbs, but an intact upper body [Sanchez et al., 2012]. Other neurological diseases which can induce limb motor and sensory deficits include stroke, traumatic brain injury, and ALS, with respective annual incidence per 100,000 of 183, 101, and

1.6 [Hirtz et al., 2007, del Ama et al., 2012].

1.1.2 Approaches

1.1.2.1 Functional Electrical Stimulation

For partially paralyzed patients, one promising method of restoring control to intact limb muscles is Functional Electrical Stimulation (FES). With FES, limb muscles that no longer receive efferent innervation are stimulated directly with electrodes. This technology has been used to restore limited walking and grasping capabilities to SCI patients [Popovic et al., 2001], both alone and with robotic assistance [del Ama et al., 2012]. There are limitations to FES, e.g., muscle fatigue occurs fairly rapidly, limiting the duration of restored movement in a particular session [Nangini et al., 2006]. One suggested solution to this problem is to create more natural muscle stimulation through the use of individual muscle groups [Lau et al., 1995].

1.1.2.2 Prostheses

Estimates based on data from 1996 suggest 1.2 million people suffer from limb loss [Ziegler-Graham et al., 2008], with approximately 185,000 people undergoing an upper or lower limb amputation each year [Owings and Kozak, 1998]. Recently developed artificial limbs allow for similar independent control to what is naturally present in healthy people, with individual finger joint flexion and extension (examples include:

the *i-Limb* from Touch Bionics (Mansfield, MA); the bebionic from RSLSteeper (Severn Road, Leeds, UK), and with arm and shoulder flexion, extension, and rotation (examples include: the APL *Modular Prosthetic Limb* (Howard County, MD); the DEKA *Prosthetic arm* (Manchester, NH)). The bottleneck with these prostheses is to allow subjects to control the dozens of degrees-of-freedom of the limb available with each device [Fougner et al., 2012].

1.1.2.2.1 Myoelectric Control

Myoelectric systems have been receiving widespread use as the control method for prosthetic devices by amputees [Parker and Scott, 1985, Scott and Parker, 1988]. Myoelectric systems are based on extracting control signals from existing electromyographic (EMG) signals produced by muscles remaining after the amputation. These control signals are called myoelectric signals (MES), and common processing techniques based on the time-domain features include measuring the voltage amplitude [Scott and Dorcas, 1966], or the rate of change of this amplitude to achieve control [Childress, 1969]. More recently implementations include time-scale feature analysis such as through the use of the short-time Fourier transform [Englehart et al., 1999b], or wavelet transform [Karlsson et al., 1999, Englehart et al., 2001]. Additional techniques are used to improve decoding the signals, such as projection into principal component space through the application of Principal Component Analysis (PCA) [Englehart et al., 1999a], or through the application of Linear Discriminant Analysis (LDA) as a dimensionality reduction method [Chu et al., 2007].

1.1.2.2.2 Targeted Nerve / Motor Reinnervation

Targeted nerve reinnervation (TNR), targeted motor reinnervation (TMR), or more simply, targeted reinnervation (TR), is a recently developed technique for allowing amputees to control prosthetic devices [Kuiken et al., 2004, Kuiken et al., 2007b, Kuiken et al., 2009]. The method consists of amputated brachial plexus nerves, which previously provided motor control and sensory feedback in the missing limb, being transferred to arm and chest muscles that remain after the amputation. After reinnervation, the EMG signals which are recorded from these reinnervated muscles still correspond to the amputees' intended activation of the phantom limb, as sent from the brain down to the brachial plexus nerve [Kuiken et al., 2007a]. This method allows for more natural control of prostheses by amputees, and could allow for an increase in the complexity of the control signals necessary for the prostheses these amputees can control [Miller et al., 2008].

1.1.2.2.3 Brain Computer Interface (BCI)

Brain Computer Interfaces allow a paralyzed user to control an end-effector purely based off of thought, or more specifically, through the controlled modulation of brain activation [Curran and Stokes, 2003, Allison et al., 2007]. BCI control may only be necessary for the most severely paralyzed, however, due to the advances in the previously stated techniques. Recently, the capabilities of BCIs for control have been extended by allowing for hybrid control for those who don't suffer from complete locked-in-syndrome [Katyal et al., 2013, McMullen et al., 2014, McMullen et al., 2015].

The techniques used, and some of their advantages and limitations for real-time prosthesis control, will be discussed in the next section.

Connectivity Based Features

Network methods are attractive because they could allow for independent control of multiple muscle groups through utilization of network properties specific to areas relevant to certain muscles. Network methods could also allow for an increased dimensionality in the decoded space, with individual groups being used to decode separate movement features, allowing for direct and natural neural control of multi-joint prosthetic devices. Since they inherently divide the neural signals into distinct groups based on the measure used, the network models could streamline the process of identifying neural ensembles to train for independent feature control, thus providing a more natural division of neurons into functional groups.

1.2 Background

1.2.1 Motor Pathways

Brain control of speech production is in many ways similar to that of limb movement, but the differences are still substantial [Grimme et al., 2011]. The departure between the two pathways, specifically for output control, is illustrated by the physical limitations of the two types of control.

Limb motor control requires the coordination of physical forces exerted by muscle groups. Speech control, however, is proportionately more cognition focused, with understanding and real-time processing of the complex rules of language a prerequisite for the creation of interpretable words and sentences [Brooks, 1986]. The similarities are apparent, however, when it is taken into account that speech production is also bound by physical laws, and requires motor control mechanisms for proper execution. This includes the active participation of the motor cortex (area M1) and its efferent pathways [Ackermann and Riecker, 2004].

While the execution of limb and speech movement is discussed in this section, the input pathways for both modalities bare considerable differences in both of the regions implicated, and the time-dependent cascade structure. Input modalities are not considered here.

1.2.1.1 Limb Position Control

Motor movement control of the hands and arms is not a simple mapping between the underlying neural activity and any obvious aspect of the resultant physical output [Lacquaniti, 1989]. In fact, while the somatosensory cortex shows somatotopic organization at the individual finger level, the mapping in motor cortex is considerably more complex, below the scale of the individual limbs [Schieber and Hibbard, 1993]. This is suggestive of an increase in the complexity of how the brain encodes individual movements over the processing of sensory stimulation [Schieber, 2001].

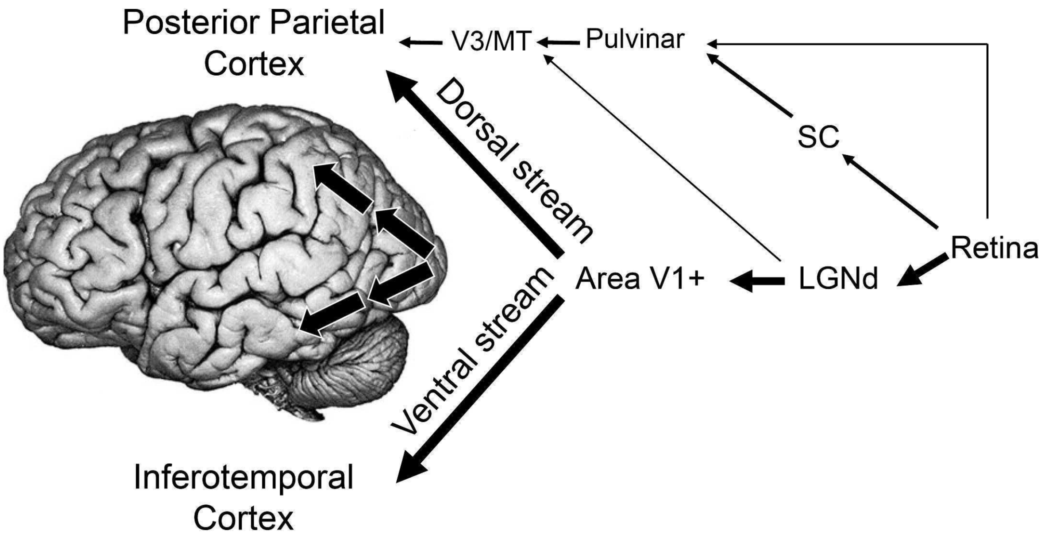

Figure 1.1: Two-stream hypothesis for visually-guided movement [Goodale, 2011]. (©Vision Research, 2011)

From a more global perspective, however, the motor output pathway during a visually-cued reach-to-grasp task, which the limb control experiments analyzed in this thesis all qualify as, is relatively well understood [Jeannerod, 1994].

Initially at the cortical level, task-specific visual cues are processed in visual cortex (area V1) [Zipser et al., 1996]. The neurons in this area represents complex stimulus properties, with a retinotopic organization of the visual field [Hubel and Wiesel, 1968]. At this point in a reach-to-grasp task, however, the processed information diverges, with the particular pathway chosen dependent on whether it will be used for determining where and how to reach toward, or how precisely to grasp (and subsequently manipulate) the object in the task-space [Ungerleider and Mishkin, 1982]. This separation of task-specific information flow is called the dual-stream hypothesis, separated into the ventral- object recognition component, and the dorsal- location guiding pathway [Goodale and Milner, 1992].

There is evidence, however, that the areas described in this section are not as segregated as previously believed [Goodale, 1998]. Mainly, areas previously believed to be strictly sensory are also implicated in direct efferent pathways [Milner and Goodale, 1995]. This should be kept in mind during the following overview of the more traditional feed-forward model of the motor pathways, as depicted in Figure 1.2.

1.2.1.1.1 Dorsal Visual Stream Hypothesis

Following processing in the visual cortex, objects are identified, and reach movement planning occurs along the dorsal stream [Chao and Martin, 2000]. Further semantic object information is processed and stored in posterior temporal cortex [Chao et al., 1999], but for my thesis work the focus is on motor planing. While there are many parallels in human anatomy, much of what is known about motor planning anatomy comes from studies in monkeys, so the specific areas described are specific to macaque monkeys.

The posterior parietal cortex (PPC), which receives input from the visual cortex, is involved with the multimodal representation of space, and is also implicated in movement planning [Andersen et al., 1997]. More specifically, the lateral intraparietal area (LIP) of PPC tracks eye position and forms plans for saccadic eye movements [Andersen et al., 1992], while medial superior temporal area (MST) guides visual motion processing [Beauchamp et al., 2002]. The dorsal area of MST (dMST) specifically is involved in tracking complicated movements of objects in the visual field [Graziano

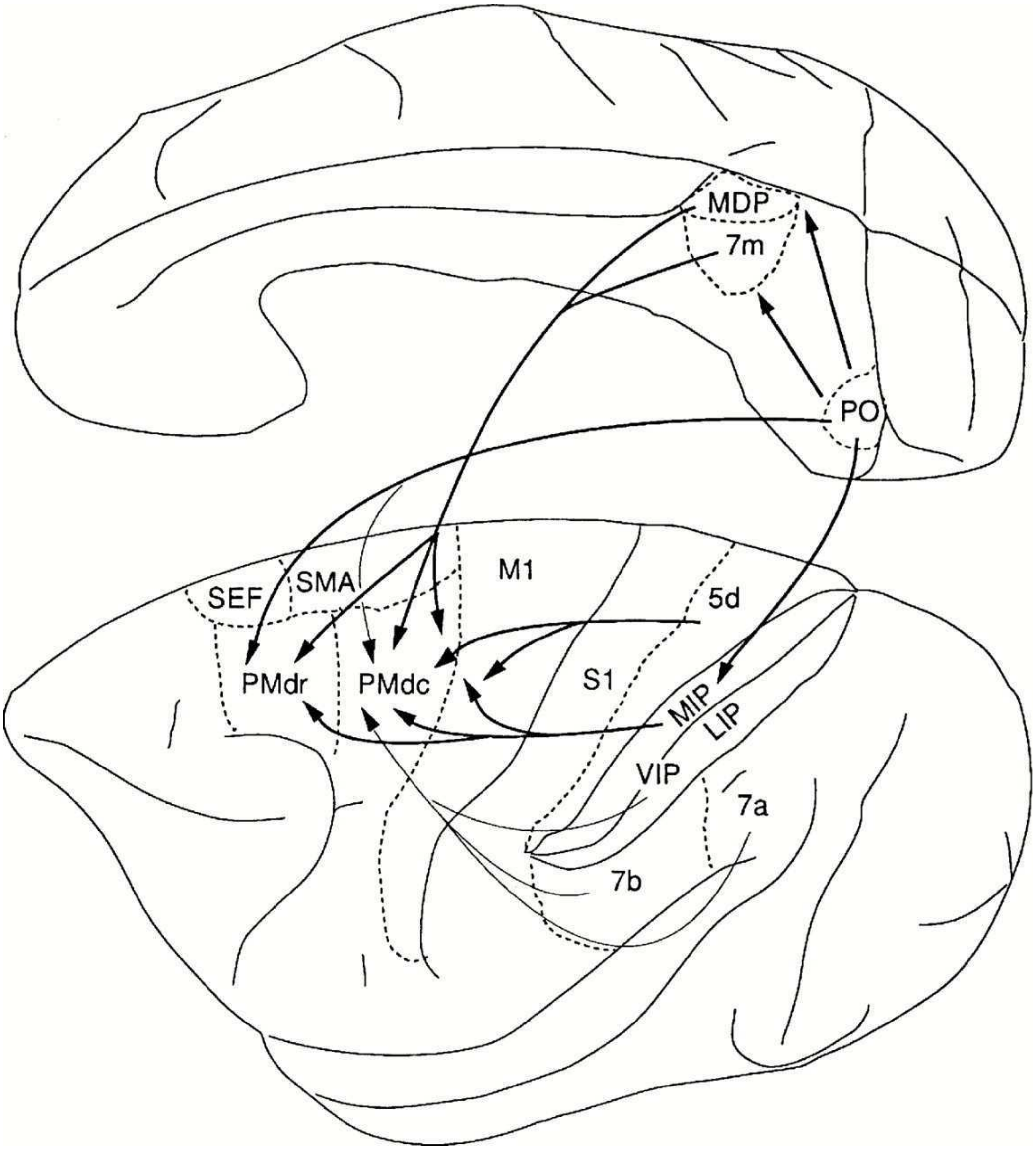

Figure 1.2: Post-visual cortex output: cortical motor-output pathway [Wise et al., 1997]. (©Annual Reviews Neuroscience, 1997)

et al., 1994], and for tracking self-guided movement's affect on the visual field [Komatsu and Wurtz, 1988, Thier and Erickson, 1992].

The PPC shows output-modality independent activation, e.g., the firing in PPC is not selective for planning of eye movement or hand movement [Robinson et al., 1978]. This task-independence suggests that PPC's role in movement planning is to mediate the visual response to selected stimuli [Bushnell et al., 1981].

The premotor dorsal cortex (PMd), along with supplementary motor area (SMA), upon receiving information concerning attention and the visuospatial representation of the object to be manipulated, produce output specific to the selection, preparation, and execution of movement [Wise et al., 1997, Kermadi, 2000, Cisek, 2006].

The output of PMd and SMA help guide the activation of motor cortex (M1), transitioning from a more abstract representation of the motor movements to specific control signals [KERMADI, 1997, Wu and Hatsopoulos, 2007]. This cortical output commonly enters the corticospinal tract (CST) to drive the motor output [Lemon, 2008]. There is more recent evidence, however, that these areas previously thought to function exclusively in motor planning have direct output projections to spinal motoneurons (PMd: [Dum and Strick, 2002], SMA: [Boudrias et al., 2006]).

1.2.1.1.2 Ventral Visual Stream Hypothesis

After early visual processing, object manipulation planning occurs along the ventral visual stream [Theys et al., 2015], where it inputs into the anterior intraparietal sulcus (AIP). AIP is implicated in visual control of grasping and manipulation of hand movements, controlling for specific aspects of the object such as size, shape, orientation in three dimensional space [Sakata and Taira, 1994, Murata et al., 2000].

The ouptut from the AIP informs the ventral premotor cortex (PMv), sthrough projections, of the three dimensional representation of the object [Theys et al., 2015]. Converting this task-independent visuospatial object representation into actionable motor planning most likely begins in PMv [Chao and Martin, 2000].

From PMv, the ventral pathway basically converges with the dorsal pathway, in that the output projections of both pathways run parallel through M1 and the CST [Lemon, 2008]. While the M1 hand area has been shown to have no clear somatotopy [Schieber and Hibbard, 1993], at a more gross level the pathways are segregated in which areas of the limb they control [Plow et al., 2010]. The pathways do maintain gross somatotopic specificity through M1, but there is substantial overlap at the level of individual spinal motoneuron innervation [Schieber, 2001], which then directly control muscle fibers for movement actuation [Wuerker et al., 1965, McPhedran et al., 1965].

1.2.1.2 Speech Control

There is a direct parallel to the dual-stream hypothesis for auditory information flow. Proceeding transduction by the ear and cochlea, properties of the aural stimuli are processed in the superior temporal gyrus (STG) and subsequently the superior

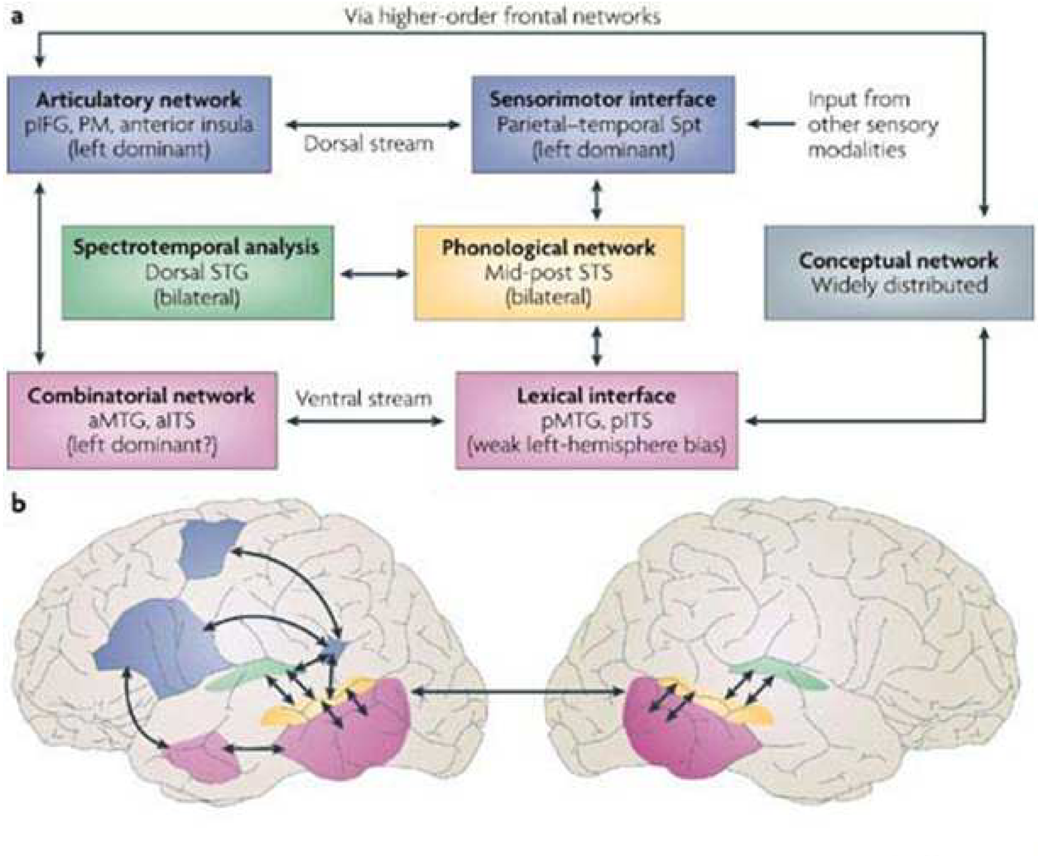

Nature Reviews | Neuroscience

Figure 1.3: Two-stream hypothesis for speech processing [Hickok and Poeppel, 2007].

(©Nature Reviews Neuroscience, 2007)

temporal sulcus (STS) before being divided up into the ventral and dorsal streams [Hickok and Poeppel, 2007].

While the ventral pathway processes the content of the aural information for interpretation, the dorsal pathway is implicated in response formation [Saur et al., 2008]. For the picture naming task used in this thesis, the dorsal pathway is of interest. Specifically, the experimental task involves the presentation of a picture, which a subject must then name.

1.2.2 Recording Methodology

In order to directly study the brain and motor control, recordings must be obtained during the execution of the task of interest. Imaging studies are popular due to their ability to capture 3-dimensional structure with high regional specificity. The work here is all limited to electrophysiological recordings, however, so the methodology and characteristics of various imaging techniques is not discussed here.

1.2.2.1 Electromyography (EMG)

For amputees who maintain control of remaining muscle activation, EMG is an effective approach to allowing them to control a prosthetic device. With EMG recordings, electrodes are placed on top of functioning muscles, and record voltage activity when contraction occurs [Ahmad et al., 2012]. Through the application of signal processing techniques, EMG approaches to prosthesis control determine how to move the limb

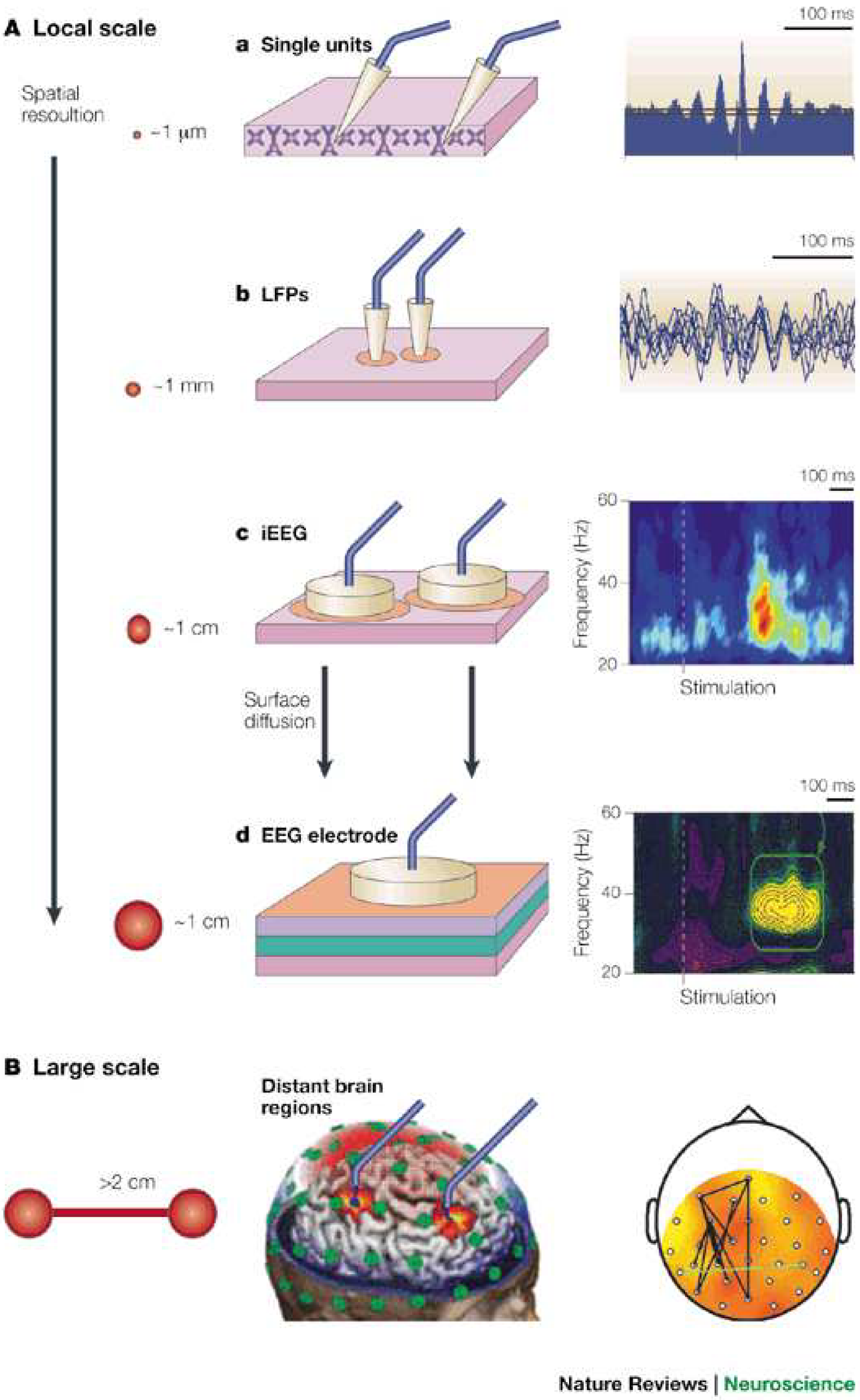

Figure 1.4: Comparison between scales of recording techniques [Varela et al., 2001]. (©Nature Reviews Neuroscience, 2001)

based on these recordings [Parker et al., 2006].

The application of sophisticated decoding techniques to the EMG signals has allowed for improved prosthesis control. One example is Support Vector Machine classification, which has allowed for three DOF control, including wrist flexion-extension, abduction-adduction and forearm pronation-supination [Ameri et al., 2014]. Another example is the implementation of pattern recognition techniques, which has been shown to improve accuracy in discrete and simultaneous movements [Young et al., 2013, Young et al., 2014]. Even individual finger positions have been shown to be decodable with EMG with high accuracy [Smith et al., 2008].

Other less algorithmic optimization have also been studied for EMG, for example, recent studies have been done to find the ideal electrode size and placement [Young et al., 2011, Young et al., 2012]. The previously mentioned TMR method allows for improved naturalness in control of prosthetics, due to the subject activating the same nerves which they had prior to amputation, and not having to learn to modulate other muscles as a surrogate. EMG based control still has to improve to restore natural control of all of the DoFs available, however, with the advanced prostheses already available on the market [Fougner et al., 2012].

1.2.2.2 Electroencephalography (EEG)

Brain-Computer interfaces (BCIs) use electrophysiological measures of brain function to enable individuals to communicate directly with their external world, bypassing normal neuromuscular pathways. Recently, noninvasive BCIs have used a variety of electroencephalography (EEG) based features to communicate the intent of the user, such as slow cortical potentials and event-related desynchronization via motor imagery. This noninvasive EEG-BCI has been a highly active research topic in neuroscience, engineering, and signal processing. One of the reasons for this development is the remarkable advances of BCI systems with respect to usability, information transfer, and robustness for which modern machine learning and signal processing techniques have been instrumental [Guger et al., 2003].

One of the most important characteristics of the EEG recorded over the sensorimotor cortex is linked to possible modulation of EEG rhythms through simple motor imagery, e.g., imagining a flexion of the right or left elbow. A widely used rhythm for control is the mu rhythm (812 Hz). The reason for utilizing the mu band is that it shows an increase in power during relaxation (event-related synchronization), and similarly, a decrease during real and imaginary motor movement performance (event-related desynchronization) [McFarland et al., 1997]. This characteristic can be utilized to control a cursor in at least one dimension. The two electrodes shown to have the largest weight of mu rhythm are located at C3 and C4 or adjacent positions, but recruitment of more electrodes could be necessary for control of more sophisticated movements.

EEG is a rough measure of neural activity, based on the voltages generated by the firing of large populations of neurons, as recorded over time from the scalp at discrete sites. As a result of the distance of the electrodes from the source of the signals, and the volume conduction effect of the scalp, skull and cerebral spinal fluid, the EEG signals are a low-pass filtered version of the summed activity from large sections of pyramidal cells in the cortex [van den Broek et al., 1998].

Despite the limits in frequency and spatial resolution of EEG, complex BCI control has been achieved through the use of intelligent task design, sophisticated signal processing techniques, thorough training paradigms. There are recent examples of practical control of BCI in 3D space through the intelligent use of two degrees-of-freedom (DoF), such as a virtual car [Zhao et al., 2009], and a virtual helicopter [Royer et al., 2010], in virtual reality environments. At the most advanced, EEG BCI has been shown to control a computer cursor in three dimensions through having patients train initially in one dimension, and scale up over time to the full three dimensions of independent control [McFarland et al., 2010].

Nevertheless, the following invasive techniques provide far greater spatial and temporal resolution, allowing for much more sophisticated control in practical BCI devices, due to their closer proximity to the source signals being acquired.

1.2.2.3 Electrocorticography (ECoG)

ECoG, also known as intracranial-EEG, involves the implantation of a grid of electrodes directly on the exposed surface of the brain. Because of this, it is an invasive procedure, and so limits the set of subjects which can perform experiments. The closer contact to the source of the voltage signals generated by the brain, however, allows ECoG to record much signals with higher spatial resolution, due to the decreased volume conduction effect [Buzsáki et al., 2012]. This also results in the presence of high frequency features. The skull acts like a low-pass filter, blocking signals above 30Hz from being measured on the surface of the skull [Srinivasan et al., 1998]. Because the skull is no longer between the source of the signals (the brain) and the recording sites (electrodes), ECoG no longer has this limitation.

ECoG signal analysis is generally performed on specific frequency bands, including: mu (7-12 Hz), beta (12-30 Hz), or high gamma (70-120 Hz). It has been suggested that high-gamma power modulations are the result of the interactions between neural populations, such that high-gamma activity recorded at the ECoG scale may be a representation of the underlying neuronal population dynamics [Crone and Hao, 2002, Crone et al., 2011]. Additionally, high-gamma power changes are detectable in single trials, and have been used for online movement decoding in real-time tasks [Schalk et al., 2008].

1.2.2.4 Microelectrode neural recordings

With Microelectrode recordings, arrays are implanted into the cortical surface, and depth penetrating electrodes record the activity generated around individual neurons, ideally around the pyramidal neurons in layer V of the cortex [Buzsáki et al., 2012]. The signals acquired off of the individual electrodes can be processed in order to separate out distinct activity:

- The excitatory post-synaptic potentials of one to a few neurons can be measured at the individual sites recording from extracellular voltages.
  - The units can be high-pass filtered to separate out 'multi-unit activity' and can provide insight into very localized activity [Stark and Abeles, 2007].
  - Single unit activity can be separated out by using methods such as template matching [Kim and McNames, 2007], Principal Component Analysis [Adamos et al., 2008, Jung et al., 2006], or a wavelet approach [Letelier and Weber, 2000].
- The signals can be low-pass filtered to reveal the summed discharge of populations of neurons as they modulate the extracellular potential [Donoghue et al., 1998, Scherberger et al., 2005].

1.2.2.4.1 Single Unit / Multiunit Activity

Cortical neural prostheses based on spike decoding have the potential to restore movement to amputees and the paralyzed [Schwartz, 2004, Schwartz et al., 2006, Nicolelis and Lebedev, 2009]. Recently, they been developed to successfully decode upper arm movements of monkeys in both open-loop [Taylor et al., 2002] and with real-time feedback [Velliste et al., 2008].

Traditionally, BCI researchers have recorded from single cortical sites and been limited to decoding from individual neurons that are found to be tuned to the movement or otherwise task-related [Schwartz et al., 2001]. However, recent advances in neural recording now allow for single session datasets with multiple signals obtained at high sampling rates using microelectrode arrays. This increased data has led to the decoding of more complex, multiple-DoF movements [Vargas-Irwin et al., 2010]. Neuronal ensembles can be trained to encode unique movement parameters, suggesting the dimensionality of the control achieved could be limited only by the number of ensembles [Lebedev et al., 2005, Nicolelis and Lebedev, 2009].

Even in cases where multiple neurons are decoded, only individual contributions to the decoding accuracy are considered and not how neurons function as a group. Neuronal interactions are generally assumed to be stationary, and their groupings constant. In order to extend the capabilities of BCIs, the behavior of neurons as dynamically evolving communities must be considered. For example, although a particular group of neurons may show the highest decoding accuracy during one component of a task, there is no reason to expect the same group will decode a different component similarly well. Furthermore, not all single units from multichannel recordings are task-related and thus potentially contribute only noise to the decoding filter. Presumably, neurons that are not relevant to the task would exhibit different firing rate profiles and could thus be identified and pruned from the input space ahead of time.

1.2.2.4.2 Local Field Potentials (LFP)

Recent studies have shown tuning in Motor cortex (M1 area) of the LFP feature to reach direction [Heldman et al., 2006], and with individual finger movements [Mollazadeh et al., 2008]. This tuning was manifested as changes in signal amplitude with task parameter. This tuning was found to augment the information provided by spike activity alone, even when recorded from the same electrodes, suggesting LFP recordings could be utilized to enhance BCI control with out further implantation [Mollazadeh et al., 2008, Bansal et al., 2012].

LFP recordings are more robust than spike activity, since the they are not dependent on the electrode being nearly in contact with the same neuron over multiple sessions [Ceyssens et al., 2013]. This robustness suggests LFP could be used for BCI control with chronically implanted microelectrode arrays, without requiring substantial retraining or readjustment.

Despite these benefits, no group to date has reported utilizing LFP recordings for BCI control [Moran, 2010]. This is partly due to LFPs not previously being thought of as contributing unique information over spikes. Additionally, other less-invasive recording methodologies have gained in popularity due to the advancement of processing techniques in the field.

1.2.3 Continuous signal decoding techniques

1.2.3.1 Frequency features

Analysis of ECoG signals often focuses on activity in specific frequency bands, for example: mu (7-12 Hz), beta (12-30 Hz), or high gamma (70-120 Hz). High gamma power modulation has been shown to reflect firing rate changes underlying neuronal populations and has been demonstrated across many functional domains to be a robust index of cortical activation [Crone et al., 2011]. Additionally, changes in high gamma power are detectable in single trials [Flinker et al., 2010a], and are commonly used as inputs to decoding models for brain-machine interfaces (BCIs) [Schalk et al., 2008]. High gamma power exhibits robust task-related changes in effective connectivity during language and motor tasks [Sinai et al., 2005, Towle et al., 2008, Korzeniewska et al., 2011, Marsden et al., 2000] and coupling to theta band (4-8 Hz) oscillations during a variety of tasks [Canolty et al., 2006].

1.2.4 Connectivity methods

Connectivity methods are a way of modeling activity at one site as it is influenced by, or influences, the activity at other sites which are simultaneously being recorded. While pairwise similarity measures such as correlation [Melssen and Epping, 1987], and cross-power [Arslan and Sakarya, 2000], can be considered network models for neural signals, in this thesis I focus on Granger Causal methods. Granger causality is a definition of connectivity that is used to suggest the influence one node exerts on another in a network, in a Bayesian sense [Granger, 1969a, Granger, 1988, Granger, 1969b, Brovelli et al., 2004]. Alternatively, a measure of Granger causality indicates how much one signal can influence the activity of another. In this sense, if the measure is positive, the first signal can be said to be Granger causal of the second one.

The planning and execution of complex movements involves the precise coordination of multiple cortical regions [Tanji, 2001]. An understanding of the functional relationships between brain areas and their role in motor tasks may be obtained from models of connectivity between distinct regions [Rubinov and Sporns, 2010]. If such information was available for clinical decision-making, it might be used to assess or quantify the importance of a region to normal function prior to epileptic resection surgery. Likewise, connectivity methods and network measures may be used to characterize seizure activity generated by epileptogenic cortical networks [Franaszczuk et al., 1994, Baccalá et al., 2004, Ortega et al., 2008, Wilke et al., 2011].

Investigation of the relative timing of high gamma signals across multiple sites has revealed robust task-related changes in functional connectivity between distinct cortical sites (in a language task, examined in isolation [Korzeniewska et al., 2011], and in a range of tasks, shown to be coupled to theta band (4-8 Hz) oscillations [Canolty et al., 2006]). Investigation of the relative timing of high gamma signals across multiple sites has revealed robust task-related changes in functional connectivity between distinct cortical sites [Korzeniewska et al., 2011].

Connectivity models based on Granger causality [Granger, 1969a, Geweke, 1982] have been applied to electrocorticographic (ECoG) data to model the dynamics of functional interactions during different cognitive and motor tasks [Baccala et al., 1998, Wilke et al., 2009]. The direct transfer function (DTF) [Kaminski and Blinowska, 1991], is one extension of Granger causality, in which a signal of interest is represented with a multivariate autoregressive (MVAR) model estimated from the history of each neural signal. This approach has also been implemented non-parametrically using Fourier and wavelet transforms [Dhamala et al., 2008].

While the aforementioned Granger causality models are informative, they require data from multiple trials and are therefore incompatible with real-time measurement and single-trial analysis. A recently developed technique for computing dynamic connectivity in single trials, called time-varying dynamic Bayesian network (TV-DBN) modeling performs computationally efficient estimation of first-order MVAR model parameters, which can be used as an estimate of inter-electrode connectivity [Song et al., 2009, Benz et al., 2012b].

The true utility of connectivity models lies in their ability to map the recruitment of cortical populations and their functional interactions during specific tasks. A growing body of literature indicates that cortical functions are not carried out by single areas, but are instead accomplished by cortical networks involving many regions [Knight et al., 2007]. Decoding movements using connectivity information has been shown in ECoG and MEG recordings to outperform changes in spectral power at individual nodes [Benz et al., 2012b, Sugata et al., 2014]. Identifying salient connections from a connectivity map, however, requires either post-hoc manual selection by a trained observer or pre-selection of regions of interest. Additionally, due to the exponential increase in dimensionality from nodes to connections ($n \rightarrow n^2$), connectivity models should only be trained on a limited set of electrodes to prevent over-fitting. What follows is a short description of the connectivity models underlying much of the analysis in this thesis.

1.2.4.1 Event Related Causality (ERC)

ERC is a method of estimating the time-varying connectivity in a multichannel network. It has been described in full detail in [Korzeniewska et al., 2008]. The subset of electrodes chosen for network analysis are fitted with a multivariate autoregressive (MVAR) model of the form:

$$x(t) = -\sum_{j=1}^{p} A_j(t-j) + e(t) \tag{1.1}$$

where $x(t)$ is the time series of data, A_j is the matrix of MVAR coefficients, p is the model order, and $e(t)$ is the residual. The frequency domain representation of this equation is:

$$X(f) = H(f)E(f) \tag{1.2}$$

where f is the frequency and $H(f)$, the transfer function, is given by:

$$\left(\sum_{j=0}^{p} A_j e^{-i2\pi f \delta t} \right)^{-1} \tag{1.3}$$

The elements of the transfer function are used to find the short time direct directed transfer function (SdDTF), which gives directed flows in short windows between signals:

$$\zeta_{kl} = \frac{|h_{kl}(f)||\chi_{kl}(f)|}{\sqrt{\sum_{f}\sum_{kl} |h_{kl}(f)|^2 |\chi_{kl}(f)|^2}} \tag{1.4}$$

Here χ is the partial coherence, which gives direct flows between signals.

ERC is then calculated by comparing each element of the SdDTF time-frequency matrix to the baseline period to find only statistically significant event-related flows.

1.2.4.2 Time-Varying Dynamic Bayesian Networks (TV-DBN)

TV-DBN is a method of estimating, within single trials, the time-varying connectivity within a multichannel network. Here we use this method to investigate frontal-parietal networks that have previously been shown to vary with hand and finger movements [Benz et al., 2012b, Benz et al., 2012a]. Within a sliding window ending at sample t, weights $A(t)$ from the following equation were fit using linear regression with ℓ^2-norm regularization:

$$x(t) = A(t)x(t-1) + \epsilon(t),\ \epsilon \sim \mathcal{N}(0, \sigma^2 \mathbf{I}). \tag{1.5}$$

where $x(t)$ contains the vector of high gamma power at sample t of each ECoG channel after convolution with a radial basis function kernel.

The solution was found through the approximation:

$$\hat{A}(t) = \underset{A(t) \in \mathbb{R}^{1xn}}{argmin} \frac{1}{T} \sum_{t=1}^{T} w(t)\{x(t) - A(t)x(t-1)\} + \lambda \left\| A(t) \right\|_2, \tag{1.6}$$

where $\lambda = 100$, as suggested by [Benz et al., 2012b] to prioritize small coefficient values relative to modeling accuracy.

A Gaussian Radial Basis Function (RBF) kernel, notated $w(t)$, was used to incorporate additional neural data from previous samples in estimating $A(t)$, reducing noise and providing more stable estimates [Song et al., 2009].

The weight of an observation at time t^* is given by $w^t(t^*)$, defined as:

$$w^t(t^*) = \frac{K_h(t^* - t)}{\sum\limits_{t^*=1}^{T} K_h(t^* - t)}, \tag{1.7}$$

where K_h is an RBF kernel of width h:

$$K_h(t) = exp(\frac{-t^2}{h}). \tag{1.8}$$

Unlike ERC, TV-DBN does not use partial coherence to limit the resulting connectivity only to direct connections.

1.3 Summary and Dissertation Organization

Brain-Machine Interface (BCI) controlled dexterous motor prostheses are being developed to restore multi-joint movement to amputees, as well as quadriplegics. Earlier work has shown that multiple degrees-of-freedom movements are decodable in human and animal models, allowing for control of computer cursors, as well as robotic arms.

In order to improve both the degrees-of-freedom of control, as well as the intuitive nature of neuroprosthetic control, an increase in the information extracted from neural signals for use in control is necessary. Additionally, by utilizing those neural signals to gain a more complete understanding of the function of cortical areas, specific control methods which match the task-specific role of those areas may be employed. Network measures use inferred relationships between the brain signals to determine properties of the underlying connections between the sources of those signals. Current state-of-the-art BCI control methods do not use network measures to model neural data. This has limited the DoF of control obtained, as well as decoding accuracy achievable. The goal of this research is to develop a systematic way to apply network methods to BCI data analysis, control methods, and implantation guidance.

An introduction to the network methods used in this thesis follows (Chapter 2). For the first part of this work, I analyzed the performance of patients suffering from Spino-Cerebellar Ataxia and control patients during performance of a non-invasive EEG BCI control task (Chapter 3). To extract further information from electrophysiological recordings, the methodology was transitioned to invasive recordings for the remainder of the work. To find task-specific network engagement, I analyzed network measures based on connectivity analysis during the performance of a center-out reach-to-grasp task performed during ECoG recordings (Chapters 4 and 5). To determine more holistically how the task-relevant networks evolve over time, clustering analysis was performed in an unsupervised fashion using stability k-means clustering (Chapter 6). To explore the fine-grained details of single neuron network formation during a movement task, eigenspectral clustering was performed on spike data acquired from multi-electrode arrays in monkey (Chapter 7). Chapter 8 summarizes the work, and discusses the limitations and future directions.

Chapter 2

Network Measures

Network measures were originally developed for the analysis of social networks in the field of social sciences [Wasserman and Faust, 1994, Hall and Wellman, 1985]. The methods have been generalized to apply to many fields outside of the social sciences, however, such as physics, and biology. As suggested by the underlying equations, the analytic methods are generally applicable to any dataset in which the connectivity structure of the underlying network can be determined.

Efforts has been made to quantify the flow of information in the brain through the application of network measures [Rubinov and Sporns, 2010]. These methods are applied to connectivity measures taken on multi-channel neural recordings, or images, in order to quantify the strength of connections between distinct brain regions, and make inference based on them [Bullmore and Sporns, 2012]. The impetus behind much of this research is an interest in quantifying normal functioning behavior in order to detect dysfunction in patient populations with neurodegenerative diseases, quantified through differences in these network measures [Van Den Heuvel and Pol, 2010].

2.1 Centrality Measures

A centrality measure is a quantification of the importance a node contributes to a network. In the case of neural imaging studies, the nodes are voxels or regions of voxels with anatomical continuity, and the edges are functional connections [Smith et al., 2011]. With neural microelectrode or surface recordings, however, the nodes are the individual electrode voltages or frequency feature power.

For an in-depth introduction to centrality measures, see chapter 7 of [Newman, 2010].

For the remainder of the chapter, it will be assumed that we have a network consisting of the connections between n nodes, or recording sites. Further, it is assumed that an adjacency matrix, $A \in \mathbb{N}^{nxn}$, has already been found for this network. The i, j-th element of A represents the connection strength from node i in the network to node j. Thus, the centrality measure of A determines how important the contribution of each node, or row in the matrix A is to the network.

2.1.1 Degree

Degree is the most basic measure of centrality [Freeman, 1979]. It is simply the row sum of the adjacency matrix. Intuitively, each degree centrality value represents the total strength of all of the connections which the corresponding node forms.

2.1.2 Betweenness

Betweenness centrality, while also being a fairly basic measure, is based on addressing the question of which nodes are important to a network with sparse connectivity, i.e., many of the entries in the adjacency matrix are valued at 0 [Anthonisse, 1971].

To quantify this importance, betweenness centrality represents which nodes in the network have the most shortest-path connections passing through them. In the case where there are multiple shortest paths for two nodes, the weight of the intermediary node is diminished proportionately by the number of possible shortest paths (i.e., geodesic paths).

The method is fairly straightforward, as implemented by Freemen [Freeman, 1977]. First, the betweenness measure for the individual node k is determined using the fraction of geodesic paths from node i to node j that pass through k, as in:

$$b_{ij}(p_k) = \frac{g_{ij}(p_k)}{g_{ij}}, \tag{2.1}$$

where b_{ij} is the betweenness measure of k on the paths between nodes i and j.

Finally, this measure for each node k is summed up over all possible source and target nodes in the network to form the centrality measure c_B through the following equation:

$$c_B(p_k) = \sum_{i=1}^{n-1} \sum_{j=i+1}^{n} b_{ij}(p_k). \tag{2.2}$$

The output from this equation, c_B, is a n-length vector consisting of the betweenness centrality values for each node.

2.1.3 Closeness

A similar measure to betweenness centrality, which also involves calculating the geodesic paths, is closeness centrality [Stephenson and Zelen, 1989]. Closeness centrality is a measure of the mean distance from each vertex to the other nodes in the network.

The mean distance for each node is determined by:

$$l(i) = \frac{1}{n-1} \sum_{j(\neq i)} d_{ij}, \tag{2.3}$$

where d_{ij} is the adjacency of nodes i and j.

While this measure is actually a distance measure, the closeness centrality value is easily computed by inverting the equation:

$$C_i = \frac{1}{l(i)} = \frac{n}{\sum_j d_{ij}}. \tag{2.4}$$

2.1.4 PageRank

An eigenvector-based centrality measure, PageRank is a quantification of how many connections each node forms, whether directly or indirectly, i.e., of arbitrary path-length. Originally PageRank centrality was developed for the Google web search engine, but it has been directly applied to various networks. Common examples include social networks, such as Twitter [Ghosh et al., 2012], and Slashdot [Kunegis et al., 2009]. The method has similarly been applied to ranking academic journal citation importance [Chen et al., 2007], to semantic processing for word sense disambiguation [Mihalcea et al., 2004], and to image processing for ranking images [Jing and Baluja, 2008].

The rows of the adjacency matrix are divided by their individual sums to create a Stochastic matrix, labeled S. The matrix must be stochastic to ensure that a stationary vector exists for any S.

The Google matrix G, which describes the directional interactions of the network [Ermann et al., 2013], is formed. The Google matrix consists of the linear combination of S with a matrix consisting of 1's for all elements ($\mathbf{1}$) [Page et al., 1999, Austin, 2006],

$$G = \alpha S + (1 - \alpha)\frac{1}{n}\mathbf{1}, \tag{2.5}$$

where n is the number of rows in S, and α is a weighting parameter allowing for an emphasis on either direct connections, or the equal probability of randomly jumping to another node. Commonly, $\alpha = 0.85$ is used as an adequate trade-off between the probability of following the adjacency matrix, and the probability of transferring to a random node. Different fields may have their own standard value.

If the adjacency matrix has non-negative elements, the Google matrix will have all positive elements. This implies that G is a primitive matrix, meaning that it is possible to find an indirect connection from one node to another of any arbitrary length. This is necessary for the power method to work, which determines the stationary vector with a low number of matrix multiplications (extended in [Haveliwala et al., 2003, Kamvar et al., 2003]). For sufficiently large networks, the power method may be advantageous for time-constrained calculations.

Eigenvector decomposition is performed on the Google matrix, G, and the eigenvector corresponding to the maximal eigenvalue of G is denoted C^1. Thus, the following equation is solved for the time-varying Google matrix G:

$$GC^1 = \lambda^1 C^1, \tag{2.6}$$

where λ indicates the eigenvalues in descending order, and C is the corresponding eigenvector. The centrality vector is notated C^1. The entries in C^1 indicated the total information flow to each node in the network.

2.1.5 Eigenvector

The subsequent methods, Eigenvector and Katz centrality predate PageRank, and are actually specialized cases of PageRank. Eigenvector centrality replaces Equation 2.5's stochastic matrix S with the adjacency matrix directly, and sets the α-value to 1. This has the effect of eliminating the impact of random jumps.

2.1.6 Katz

Similar to Eigenvector centrality, Katz centrality replaces Equation 2.5's α-value with the number 1. It still uses the stochastic matrix S in the calculation, however.

2.1.7 Centrality Comparison

Table 2.1 demonstrates the differences between the three eigenspectral centrality measures, and their relationship to the most basic degree centrality. The matrix D is diagonal, and is made up of the degree of each node i along the diagonal: $D_{i,i} = k_i$.

2.2 Clustering

Clustering is the unsupervised segmentation of data sets into distinct groups [Jain et al., 1999]. This is useful for determining the underlying activation patterns for distinct neural states during the complex tasks analyzed in this thesis.

Table 2.1: Centrality Methods Comparison (Modified from [Newman, 2010]).

	$0 <= \alpha <= 1$	$\alpha = 1$
Stochastic matrix	$x = D(D - \alpha A)^{-1}\mathbf{1}$ PageRank	$x = AD^{-1}x$ Degree
Adjacency matrix	$x = (I - \alpha A)^{-1}\mathbf{1}$ Katz	$x = \kappa_1^{-1}Ax$ Eigenvector

Throughout this thesis, two broad categories of clustering methods are performed. The first, centroid based clustering, is done using the features directly. Most commonly, High-gamma power is used as the input to the clustering techniques. The dimensionality of the input space is (n x t): the number of electrodes by the time-window segmentation.

The second technique, connectivity based clustering, involves finding the connectivity between each pair of electrodes, using the techniques listed in chapter 1. The adjacency matrices provided by these techniques are then clustered on directly.

2.2.1 Centroid based clustering

Due to its clustering on the features directly, centroid based clustering results in easier to interpret segmentation of neural data than connectivity based clustering. Since they don't require the computation of a adjacency matrix, these methods are less configurable, but still have many aspects that can be modified depending on the form

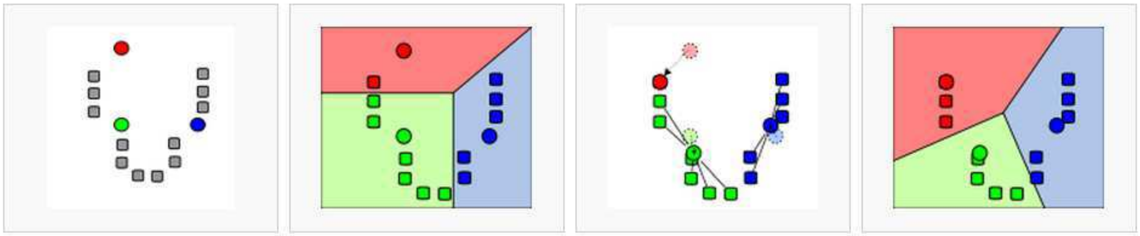

1. *k* initial "means" (in this case *k*=3) are randomly generated within the data domain (shown in color).

2. *k* clusters are created by associating every observation with the nearest mean. The partitions here represent the Voronoi diagram generated by the means.

3. The centroid of each of the *k* clusters becomes the new mean.

4. Steps 2 and 3 are repeated until convergence has been reached.

Figure 2.1: Demonstration of the k-means algorithm. (©Wikimedia Foundation, 2016)

of the data or the intended analysis.

2.2.1.1 K-means

K-means is an unsupervised clustering technique with a hyper parameter K, representing the number of clusters. for a specific K, K-means finds the centroid of each cluster which minimizes the total distance from all features to the nearest cluster. This is commonly achieved using EM (expectation maximization), since the exact solution is NP-hard, through the steps illustrated in Figure 2.1.

Since K-means looks to minimize the distance from the centroid to each group member in the high-dimensional space of the underlying data, different distance functions can be used, and may impact the results. Commonly, square Euclidean distance is used, but alternative distance metrics include taxicab (Manhattan) distance, cosine distance, Minkowski distance and cluster symmetry (an extension of point symmetry)

[Aggarwal et al., 2001, Su and Chou, 2001, Modha and Spangler, 2003, Patel and Mehta, 2012].

Similarly, the location of the centroids is not necessarily the mean of the coordinates of its members. A popular alternative, K-medoids, is based on the median of each cluster's members location in high-dimensional space [Singh and Chauhan, 2011].

2.2.2 Connectivity based clustering

Clustering on connectivity structure requires the prior formation of an adjacency matrix using the selected connectivity measure. The adjacency matrix is then used directly with the clustering methods. This has the implication that if the connectivity measure does not contain information about the features of interest for the analysis, it is not possible to make conclusions based on those features using connectivity clustering. While the clusters may still provide interesting insight, they won't contain structure relating to the property of interest.

2.2.2.1 Spectral clustering

While there are multiple approach to spectral clustering [Ng et al., 2002, Zelnik-Manor and Perona, 2004, Von Luxburg, 2007], for the purposes of this thesis an adaptation of [Newman, 2006] is used, with a modification to optimize the number of clusters found [Humphries, 2011].

For this section, the similarity matrix (denoted by C; for consistency with [Newman,

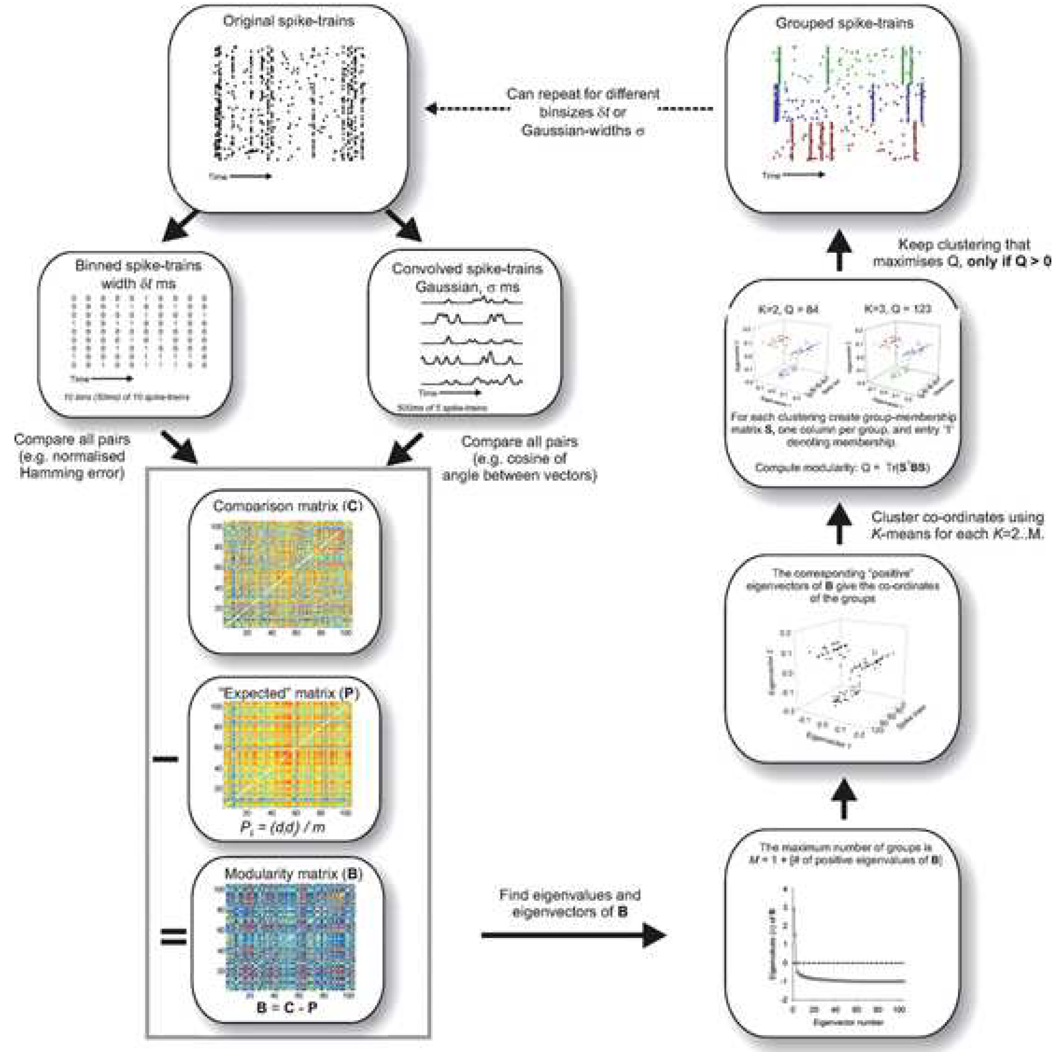

Figure 2.2: Flow chart for spectral clustering technique as applied to spike data [Humphries, 2011]. (©Society for Neuroscience, 2011)

2006]) is non-directional. The diagonal of C is set to zero, so that self-similarity will not influence grouping. The goal of the approach is to maximize the modularity Q over all possible divisions of the network,

$$Q = trace(S^T(C - P)S), \tag{2.7}$$

where C is the similarity matrix from before; P is the null-network model that captures the expected number of links within each community, and S is a matrix denoting which group a node belongs to. In other words, P represents the pair-wise probability of a connection between two nodes. S represents the grouping matrix, where each row contains a 1 for the column corresponding to that node's group.

Rather than fixing the number of groups a priori, both the group count and group memberships of all nodes is determined iteratively. To determine an upper bound on the number of possible groups, singular value decomposition is performed on the modularity matrix $B = C - P$, and all N eigenvectors with positive eigenvalues is retained. K-means clustering for $K = 2...N + 1$ possible groupings is then be performed, and Q_K for each case is calculated.

The clustering that provides the largest value for Q_K indicates the most natural grouping structure for the given adjacency matrix. While for multiple numbers of clusters there may be interpretable grouping structure, the $max_K Q$ is the one best supported by the method.

Chapter 3

Cerebellar ataxia patients are able to use motor imagery to modulate mu-band power in a pilot study of EEG-based brain-computer interface control

3.1 Abstract

Cerebellar ataxia is a steadily progressive neurodegenerative disease associated with loss of motor control, leaving patients unable to walk, talk, or perform activities

of daily living. Direct motor instruction in cerebellar ataxia patients has limited effectiveness, presumably because an inappropriate closed-loop cerebellar response to the inevitable observed error confounds motor learning mechanisms. However, open-loop reinforcement of motor control programs may hold promise as a technique to improve motor performance. Recent studies have validated the age-old technique of employing motor imagery training (mental rehearsal of a movement) to boost motor performance in athletes, much as a champion downhill skier visualizes the course prior to embarking on a run. Could the use of EEG-based BCI provide advanced biofeedback to improve motor imagery and provide a backdoor to improving motor performance in ataxia patients? In order to determine the feasibility of using EEG-based BCI control in this population, we compare the ability to modulate mu-band power (8-12 Hz) by performing a cued motor imagery task in an ataxia patient and healthy control.

3.2 Introduction

Brain-computer interfaces (BCIs) use electrophysiological measures of brain function to enable individuals to communicate directly with their external world, bypassing normal neuromuscular pathways. Recently, noninvasive BCIs have used a variety of electroencephalography (EEG) based features to communicate the intent of the user, such as slow cortical potentials and event-related desynchronization via motor imagery. This noninvasive EEG-BCI has been a highly active research topic in neuroscience, engineering, and signal processing. One of the reasons for this development is the remarkable advances of BCI systems with respect to usability, information transfer, and robustness for which modern machine learning and signal processing techniques have been instrumental [Guger et al., 2003].

One of the most important characteristics of the EEG recorded over the sensorimotor cortex is linked to possible modulation of EEG rhythms through simple motor imagery, e.g., imagining a flexion of the right or left elbow. A widely used rhythm for control is the mu rhythm (8-12 Hz). The reason for utilizing this is that it shows an increase in power during relaxation (event-related synchronization), and similarly, a decrease during real and imaginary motor movement performance (event-related desynchronization) [McFarland et al., 1997]. This characteristic can be utilized to control a cursor in at least one dimension. The two electrodes shown to have the largest weight of mu rhythm are located at C3 and C4 or adjacent positions, but recruitment of more electrodes could be necessary for control of more sophisticated movements.

EEG mapping may be distorted in the setting of neurologic disease, which may affect the ability of ataxia patients to use EEG-based BCI. EEG is a rough measure of neural activity, based on the voltages generated by the firing of large populations of neurons, as recorded over time from the scalp at discrete sites. Although the literature states that the EEG pattern is normal in cerebellar degeneration, this presumably refers to the lack of heightened epileptogenic potential, which does not necessarily indicate that the EEG is comparable to that of unaffected individuals.

Diaschisis (the loss of function in a distant portion of the brain that is connected to an area of injury) is a well-established phenomenon, with transneuronal degeneration in many neurodegenerative processes. We hypothesize that cortical regions of the corticocerebellar circuit may show functional abnormalities when they are connected to areas of primary cerebellar degeneration. The strong interconnections between the cerebellum and the cerebral cortex most likely contribute to the distortion in the processing of sensory feedback.

Electrophysiological studies in ataxia are rarely performed as early EEG studies were reportedly normal [Brown, 1959, Liversedge and Emery, 1961]. There are, however, some disease-specific differences in visual evoked potentials, [Schöls et al., 2008] auditory evoked potentials, [Arai et al., 2003] and auditory brain stem response [Abele et al., 1997, Schöls et al., 1997] suggestive of white matter disease located outside of the cerebellum and its direct connections. Seizures are not a common clinical manifestation, except in certain rare subtypes, such as acetazolamide-responsive paroxysmal ataxia [Zasorin et al., 1983, Van Bogaert and Szliwowski, 1996] or spinocerebellar ataxia type 10 [Rasmussen et al., 2001]; EEG findings are consistent with the epileptic phenotype.

Electrophysiological biomarker studies in other neurodegenerative diseases demonstrate that EEG measures are useful for detecting clinically relevant, disease-specific differences. Notably, power spectral density analysis of EEG in schizophrenia variously shows frequency-specific depression [Kwon et al., 1999] or failure of suppression [Clementz et al., 1997] of acoustic responses. The positive peak P300 elicited in response to acoustical stimuli with the so-called oddball paradigm has great potential to be used as a diagnostic tool in a wide range of clinical conditions, such as schizophrenia, autism, severe depression, dementia, and Alzheimers disease [Dawson et al., 1988, Blackwood, 2000, Frodl et al., 2002] Along the spectrum of normal and abnormal function, EEG measures can be used to distinguish children with low arithmetic performance [Grunau and Low, 1987].

There is some evidence that motor imagery is affected in cerebellar ataxia. In a study of people with unilateral cerebellar stroke, patients attempting motor imagery showed decreased motor evoked potential facilitation in the associated motor cortex [Battaglia et al., 2006]. In a second study, patients that had apparently recovered from a unilateral cerebellar stroke showed a marked slowing of motor performance in both hands (ipsi- and contralateral to lesion). This effect was accompanied by a similar slowing of motor imagery, suggesting that the cerebellum, traditionally implicated in the control of motor execution, is also involved in nonexecutive motor functions such as the planning and internal simulation of movements [González et al., 2005].

Thus, it remains to be proved that cerebellar ataxia patients are capable of using cued motor imagery to effect EEG changes that can be interpreted by a standard BCI system.

3.3 Methods

3.3.1 Study Subjects

One patient with cerebellar ataxia and one control subject provided informed consent according to a protocol approved by the Johns Hopkins University Institutional Review Board. Both subjects were self-reported right-handed.

3.3.2 Test Paradigm

During each trial, the subject was cued to either relax, or perform a motor imagery task (without actually moving). A three-state (move up, move down, remain still) EEG-based BCI was used to control the position of a cursor in one dimension on a computer screen. EEG signals were acquired at 250 Hz. Every 500 ms, the common average referenced signals in a 500 ms window from two electrodes (C3 and C4) were modeled as an autoregressive (AR) process [Chatterjee et al., 2007],

$$y_E[n] = \sum_{k=1}^{K} a_k y_E[n-k] + \epsilon[n], \tag{3.1}$$

where E was the electrode of interest, a_k were the autoregressive coefficients, K was the model order, and $\epsilon[n]$ was an independent identically distributed stochastic sequence with zero mean and variance 2 [Bos et al., 2002]. K was choosen to be 15. Burg's method was used to estimate the time-varying AR coefficients.

The power spectral density (in dB) of the AR processes for both electrodes was computed as,

$$P(\omega) = dB\left(\frac{\sigma^2}{|1-(a_1e^{-i\omega}+...+a_Ke^{-iK\omega})|^2}\right), \tag{3.2}$$

and the mu-band power was determined at discrete times tk as the mean of the $P(\mu)$, where μ is the mu-band frequency range (8-12 Hz).

The sum of the mu band power of the C3 and C4 electrodes were used to train a two stage hierarchical linear classifier. A gating classifier G was designed to identify significant modulations of power due to intention,

$$G(t_K) = \begin{cases} 1, & \text{if } |w_G^1 P_{C3}(t_k) + w_G^2 P_{C4}(t_k) + B_G| > T_G \\ 0, & \text{otherwise} \end{cases} \tag{3.3}$$

where w_G^1, w_G^2, B_G, and T_G were the weights, bias, and threshold respectively, as determined online for both subjects. A second movement classifier was designed to distinguish between the relaxation and the motor imagery task,

$$M(t_K) = \begin{cases} +1, & \text{if } |w_M^1 P_{C3}(t_k) + w_M^2 P_{C4}(t_k) + B_M| > T_M \\ -1, & \text{otherwise} \end{cases} \tag{3.4}$$

where w_M^1, w_M^2, B_M, and T_M were the weights, bias, and threshold respectively, as determined online for both subjects. The final output $F(t_k)$ was the product of the two classifiers,

$$F(t_k) = G(t_k) \times M(t_k), \tag{3.5}$$

where +1 corresponds to relaxation, -1 to motor imagery, and 0 to no task. If the cursor reached a target 7 steps away from the center where trials start, within 15 seconds, the trial was considered a success. To achieve a trial success case, the sum of $F(t_k)$ over all tk within that trial must equal +7 in the relaxation trials, and -7 in the motor imagery trials before 15 seconds elapse. The control subject underwent 6 sets, and the ataxia subject underwent 10 sets, of 16 trials each (8 relaxation and 8 movement imagery trials), with a pseudorandomized order of presentation within each set.

3.3.3 Data Acquisition

Signals were acquired using a QuickCap 64-channel EEG cap (modified 10-20 system, referenced between Cz and CPz, and grounded anteriorly to Fz; Compumedics, El Paso, TX). The amplifier and signal processing modules were connected through client-server architecture, with a Neuroscan SynAmps2 64-channel amplifier system from Compumedics (El Paso, TX) acting as the server, and the signal processing module running on a separate client computer. Data were sampled at 250 Hz, with a band-pass filter applied between 0.1 and 30 Hz, and transmitted over a TCP/IP protocol to the client PC for storage and real-time signal processing using a custom BCI platform.

3.3.4 Data Analysis

EEG signals were spatially filtered using common average referencing. The C3 and C4 electrodes, which generally overlap with the hand-area of the primary motor cortex, were then used in a 15th order autoregressive model to determine the power spectrum. Frequency-specific modulation was observed for C3 and C4. Topographic power spectral maps were generated for the mu frequency band.

3.4 Results

Our primary endpoint was to evaluate the possibility that ataxia patients could achieve control of a BCI using cued motor imagery. Indeed, both subjects were able to achieve mean trial success of greater than 13.21% (chance performance rate) on their first session. (Table 1). Chance performance was calculated as the probability of reaching the target based on an equal probability of performing any of the three possible movements with each step, up to the maximum allowable 30 steps. The average successful chance trial duration was determined as the first moment of chance successes rates for the allowable step counts.

Figure 1 suggests that both the ataxia patient and control subject show an increased difference in power in the mu range (8-12 Hz), between relaxation and motor imagery. This difference is greater in the control subject as compared to the ataxia patient. Although trials continued on beyond 4 seconds, the power difference between the

Subject Condition	ICARS score	Trial success rate	Average successful trial duration
Control		91.7%	7.8s
SCA6	45.5	63.1%	6.6s
Simulated Chance		13.21%	14.7s

Table 3.1: Trial performance reveals ataxia patients have the ability to perform the BCI task with significantly greater efficacy than chance. International Cooperative Ataxia Rating Scale (ICARS) score is used to determine severity of an ataxia diagnosis, out of 100, with a higher number indicating an increased severity [Trouillas et al., 1997].

two tasks is not as obvious, due to the inability of subjects to maintain the required imagination throughout the task duration. The Ataxia subject had higher power activity in low frequency bands, which is most likely due to movement artifacts.

Scalp maps representing mu band power during the task are shown (Figure 2), separated by subject. These demonstrate that the control subject increased mu power specifically over the C3 and C4 electrodes, with a bias toward the left side, during the relaxation condition. The ataxia patient appeared to show a similarly originating increase in mu power during relaxation, but at a lower amplitude, and on the right side. In the ataxia patient, the more modest increase in power is a less localized phenomenon; it appears to extend further posteriorly.

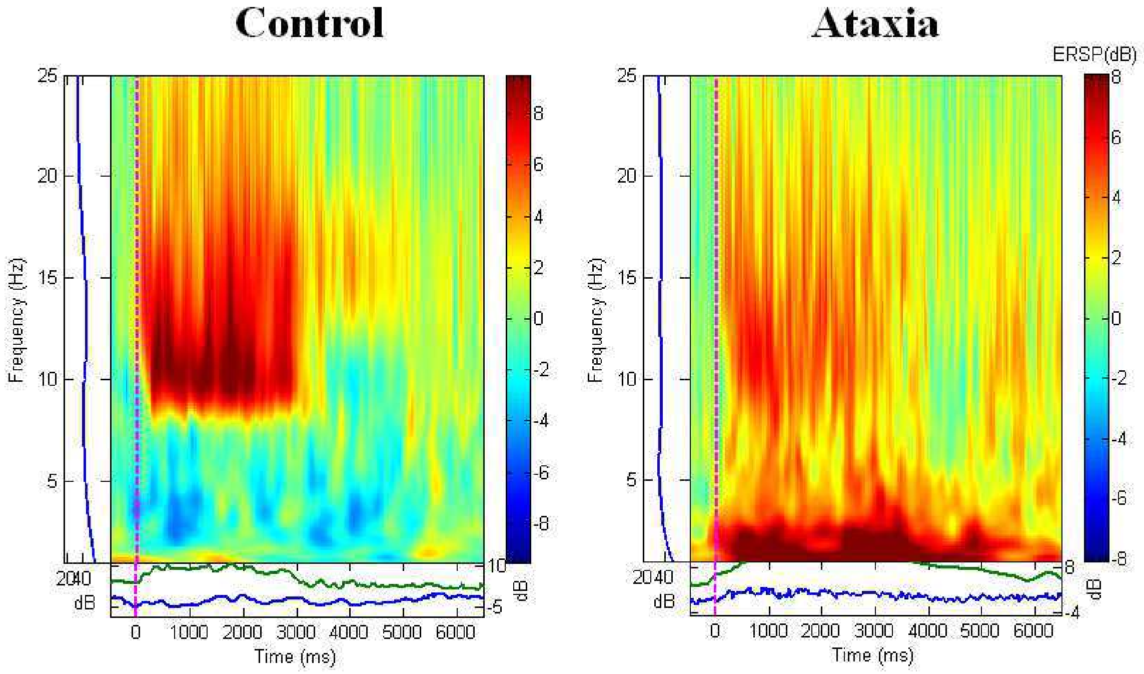

Figure 3.1: The event related spectral power (ERSP) differences between the averages of the two task conditions are displayed for the control (left) and ataxia (right) subjects from the C3 electrode. Darker shades of red represent an increase in power during the relaxation task over the motor imagery task at the same time point and frequency band within the trial. The blue trace on the left indicates average power of each frequency. The bottom blue trace indicate minimum power over the range of frequencies at each time point, while the bottom green trace indicates maximum power at each time point.

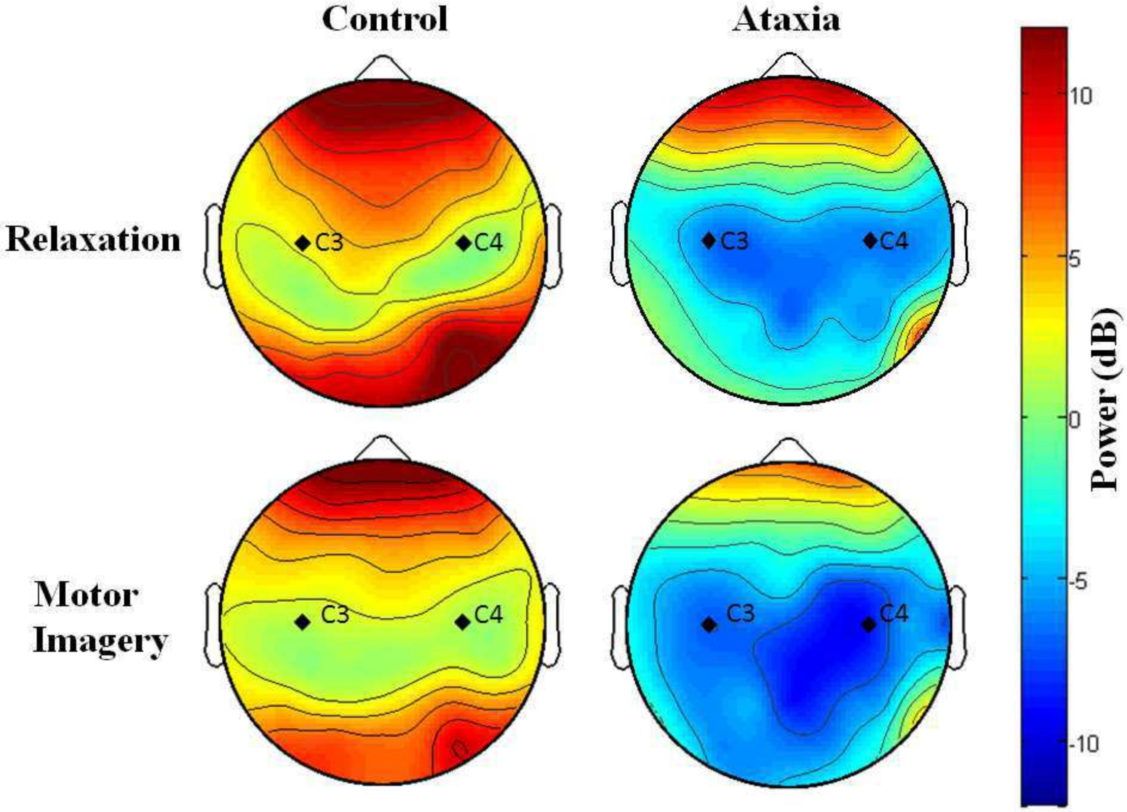

Figure 3.2: Topographic maps of mu power distribution in control (left) and ataxia (right) subjects during the two different tasks (relaxation and motor imagery). Power was determined as the average over all trials during 2-5 seconds after task cue. Both subjects show modulation with task condition by the change in color for a given electrode between the two task conditions. Selectively unilateral changes, in C3 for the control, and C4 for the ataxia patient, are made less obvious by the presence of significant power in frontal electrodes in both task conditions, possibly due to extraoculogram artifact. Mu power was determined as the power at 10 Hz using Welch's method to estimate the power spectral density.

3.5 Discussion

Our results demonstrate that despite the theoretical possibility that patients with severe ataxia may have impaired motor imagery and abnormal cortical rhythms, an ataxia patient is capable of generating sufficient changes in cortical rhythms to achieve voluntary control of an EEG-based BCI using cued motor imagery. Success and learning rates do not appear to be directly related to the clinical diagnosis of the subject.

Although the control has a higher success rate than the ataxia patient, this is most likely due to the control showing an uncommon natural ability to modulate mu rhythm, when compared to other control subjects' performance (unpublished results). Although these success rates may seem low, it may partly be due to the subjects having only completed one session of BCI control.

There are, nonetheless, observable differences between ataxia subjects and control subjects. The ataxia patient appeared to have a smaller increase in mu band power during relaxation, compared to the control. This is consistent with the possibility that ataxia patients are unable to properly modulate the synchronous firing of large groups of neurons in the motor cortex due to a deterioration of feedback pathways from the cerebellum. While overall activity in this area may be increased, this lack of increased synchronization results in attenuation of the peak in the mu band.

More global changes in power in the ataxia patient were also observed. This suggests that ataxia subjects may use a strategy of increasing global activity in order to compensate for the inability to generate synchrony with spatial or frequency specificity.

It may be possible to take advantage of these differences to create a BCI that ataxia patients would be able to control more easily, perhaps by determining the average power over several centrally focused electrodes, instead of just C3 and C4. By creating a BCI specific to ataxia patients, we may be able to increase their ability to naturally control an end-effector, and with continuous training, improve their motor control skills. For severe ataxia patients, this could mean a significant improvement in quality of life.

3.6 Conclusions

Our current setup allows ataxia patients to control a BCI with similar efficacy to control participants. The neural method of control, however, may be different between the populations. Thus, in order to improve efficacy and usability of a BCI system, it may be necessary to tailor the decoding algorithm to the more diffuse spatial response and the smaller amplitude response found in ataxia patients. The EEG differences we have uncovered could be used as a diagnostic tool, and may find a role in rehabilitation therapy.

Chapter 4

Eigenvector centrality reveals the time course of task-specific electrode connectivity in human ECoG

4.1 Abstract

Connectivity measures provide a quantification of information flow across electrodes in human subject electrocorticography (ECoG). They do not, however, lend themselves to direct interpretation due to the combinatorial size increase of the feature space. We utilize time-varying dynamic Bayesian networks (TV-DBN) as a model

of the individual ECoG electrode activity based on the activation of the electrode array. Using the high gamma power TV-DBN connectivity matrices, we determine if eigenvector centrality can objectively highlight the important interactions between electrodes. The statistically thresholded centrality measure reveals task-related differences in the significant electrode subsets during distinct task phases ($p<0.05$; 13 significant electrodes overall: 2 exclusive to the cue processing phase, 3 exclusive to the motor output phase). These results suggest that TV-DBN and centrality analysis can be used in an online brain-mapping system to show regions of the brain relevant to real-time task performance.

4.2 Introduction

The organization and execution of complex movements involves the precise coordination of multiple cortical regions [Tanji, 2001]. An understanding of the functional relationships between brain areas, and their role in the motor task, may be obtained from models of the connectivity as inferred from temporal dependence between distinct regions [Rubinov and Sporns, 2010].

While providing an interpretable measure of cortical interactions, the resultant exponential increase in dimensionality with connectivity measures causes these models to be difficult to manually parse, e.g., for clinical analysis. Fortunately, the network involvement of each electrode can be described using network measures based on the electrode connectivity. Network measures provide a summary of the activity between all of the electrodes forming a network in an abbreviated form.

To form the connectivity models, separation of the feature of interest from the raw data is required. ECoG signal analysis is generally performed on specific frequency bands, including: mu (7-12 Hz), beta (12-30 Hz), or high gamma (70-120 Hz). It has been suggested that high-gamma power modulations are the result of the interactions between neural populations, such that high-gamma activity recorded at the ECoG scale may be a representation of the underlying neuronal population dynamics [Crone et al., 2011]. Investigation of the relative timing of high gamma signals across multiple sites has revealed robust task-related changes in functional connectivity between distinct cortical sites [Korzeniewska et al., 2011]. These findings suggest high gamma band modulation could be used as a feature in network model analysis of ECoG.

Connectivity methods have been applied to ECoG connectivity to characterize seizure activity, which is believed to originate within epileptogenic cortical networks [Baccalá et al., 2004]. There are also examples of network measures being applied to neural data. The betweenness centrality of the correlations [Ortega et al., 2008] and DTF components [Wilke et al., 2011], in addition to the eigenvector centrality of the coherences [Burns et al., 2012] have been used to identify seizure networks. Eigenvector centrality, which will be used in this paper, is a measure that quantifies the information received by each node in a network through direct and indirect connections [Page et al., 1999].

In this work, we determined the network properties of the time-varying dynamic

Bayesian network (TV-DBN) connectivity of high gamma power between each electrode pair [Song et al., 2009]. TV-DBN estimates how strongly each electrode's current activity is modulated by the activity of the other electrodes in the previous sample window. Centrality, a quantification of the information each electrodes receives, is proposed to determine which neural populations receive substantial information during distinct phases of movement planning and execution. This method will allow for a more compact subset of information flows between channels to be displayed for interpretation, or to be used in further processing.

The TV-DBN and eigenvector centrality methods were applied to data obtained from a patient suffering from intractable epilepsy while performing a reach and grasp task, followed by object manipulation. To quantify the changes in network structure with task performance, entropy of the centrality vector was measured over time, and compared between task types. Additionally, the spatial distribution of the highly central electrodes was examined over time. The temporal modulation of centrality within functional networks has not previously been described during the performance of a motor task. This method may eventually improve cortical resection planning and brain-computer interface control.

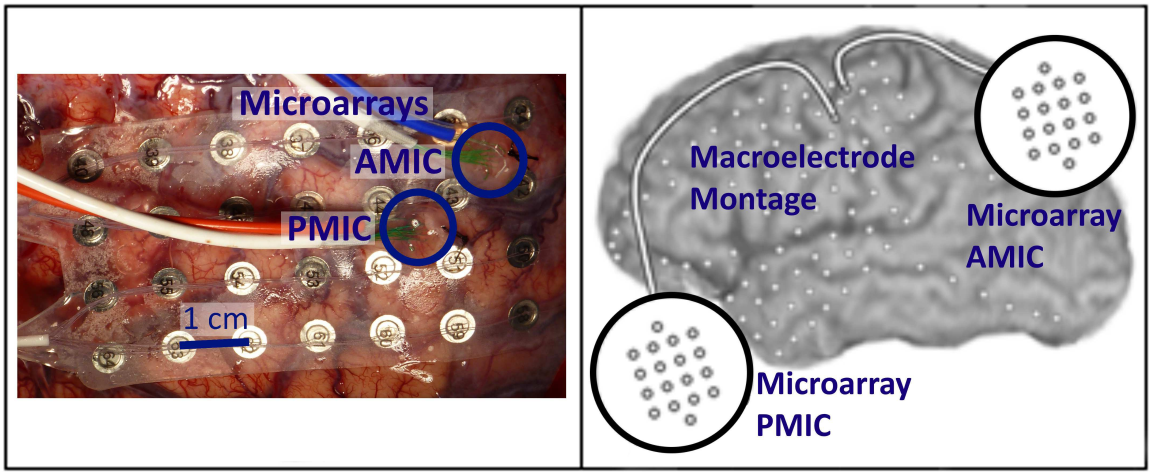

Figure 4.1: Macroelectrode and microelectrode ECoG array placement. Two microelectrode arrays were inserted within the macroelectrode grid. Additional recordings were obtained from macroelectrode strips placed on superficial layers of cortex. Intra-operative photo (left), 3D MRI reconstruction of electrode sites (right).

4.3 Methods

4.3.1 Task Participants

One 61 year old male subject was implanted with subdural ECoG macroelectrodes and microelectrodes in his left hemisphere (Fig. 6.1) for seizure focus and eloquent cortex mapping prior to epilepsy resection surgery. Electrode implantation location was determined solely based on clinical need. Data from this study were recorded from 94 ECoG macroelectrodes from two 4x8 grids and seven strips each consisting of either four or six electrodes (0.23 cm diameter, 1 cm center-to-center). Data were also recorded from 32 ECoG microelectrodes (75 micron diameter, 900 micron center-to-center) from two 4x4 grids centered between four adjacent macroelectrodes.

The subject gave informed consent to participate in this study, which was done in accordance with a protocol approved by the Institutional Review Board of Johns Hopkins University.

4.3.2 Experimental Design

The apparatus for cue presentation was placed on a table within reach of the subject, who reclined on his hospital bed for the duration of the experiment. The subject rested his right hand on an electronic home switch in his lap for monitoring movement onset. The apparatus had four objects: a push button, a key, a doorknob, and a ball, fixed to an octagonal board at 0, 90, 180, and 270 degrees 8 inches from the center of the board. LEDs surrounding the specific objects were used to cue the subject to reach and perform the following manipulations: 1) push the push button, 2) turn the key, 3) turn the doorknob, 4) and pull on the ball. For this analysis, the push button and key were grouped as dexterous manipulations while the doorknob and ball were classified as gross manipulations.

The subject completed 76 experimental trials, 34 of which were successful gross movements, and 37 of which involved successful dexterous movements. The remaining 4 trials were failures in which the subject could not complete the manipulation in under 4 seconds. The different manipulations were interleaved in pseudorandom order.

4.3.3 Signal Acquisition and Preprocessing

ECoG data were recorded with a 128-channel Neuroport system (Blackrock Microsystems; Salt Lake City, UT) at 1 kHz. Data were common average referenced, then digitally bandpass filtered from 70-120 Hz. The TV-DBN connectivity was computed in 200 ms sliding windows with a slide size of 8 ms, from 1 s before the cue onset to 4 s after the cue onset. This connectivity was computed for the 21 electrodes across the microelectrode and macroelectrode arrays which showed task related high gamma modulation.

4.3.3.1 Time-Varying Dynamic Bayesian Networks (TV-DBN)

TV-DBN is a method of estimating, within single trials, the time-varying connectivity within a multichannel network. Here we use this method to investigate frontal-parietal networks that have previously been shown to vary with hand and finger movements [Benz et al., 2012b, Benz et al., 2012a]. Within a sliding window ending at sample t, weights $A(t)$ from the following equation were fit using linear regression with ℓ^2-norm regularization:

$$x(t) = A(t)x(t-1) + \epsilon(t),\ \epsilon \sim \mathcal{N}(0, \sigma^2\mathbf{I}). \tag{4.1}$$

where $x(t)$ contains the vector of voltage values at sample t of each ECoG channel after convolution with a radial basis function kernel.

The TV-DBN coefficients, $A(t)$, were calculated for a subset of the electrodes that were found to have task-related modulation in the high-gamma band during post-hoc analysis.

4.3.3.2 Centrality

An eigenvector-based centrality measure, that quantifies the total strength of connections in the entire network each site receives, was used to describe the modulation of network activity during the movement planning and execution phases [Freeman, 1979, Page et al., 1999].

The Google matrix $G(t)$ was formed as the linear combination of the row-sum normalized TV-DBN connectivity matrices as they varied in time, $(S(t))$, with constant value matrix $\mathbf{1}$, allowing all electrodes a small presumed influence on other electrodes in the network [Page et al., 1999, Austin, 2006]:

$$G(t) = \alpha S(t) + (1 - \alpha)\frac{1}{n}\mathbf{1} \tag{4.2}$$

where n is the number of rows in S, and $\alpha = 0.85$ was used as an adequate compromise between the connectivity of the actual network, and the situation where all of the nodes are connected with equal strength.

The eigenvector corresponding to the maximal eigenvalue of G was denoted $C^1(t)$. The entries in $C^1(t)$ indicated the total information flow to each electrode in the network at sample t.

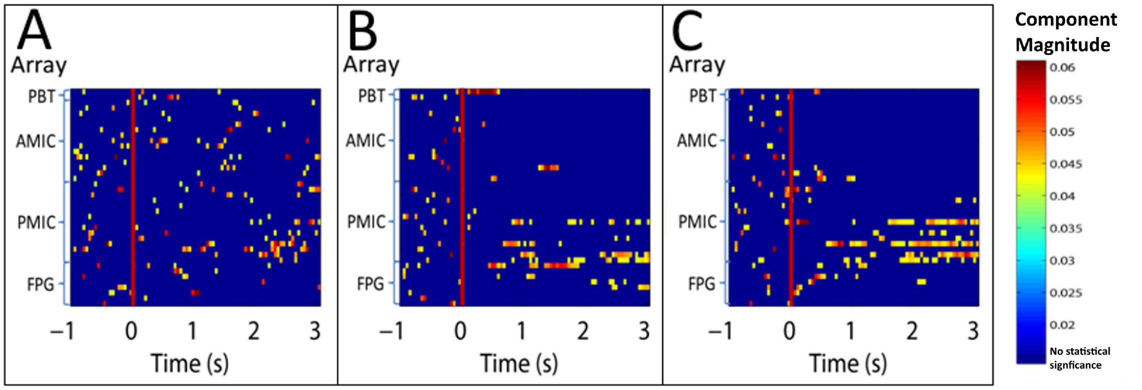

Figure 4.2: Task-related changes in centrality by electrode. The windowed TV-DBN coefficients were used to find the centrality vector. The time-varying values were compared to baseline with a two-tailed t-test ($p < 0.05$). Centrality values that were not statistically significantly different from baseline are colored dark blue. (A) the average failed trial results, (B) the gross object manipulation category and (C) the fine object manipulation categories are shown. The color is scaled by the centrality values.

4.4 Results

4.4.1 Task-related changes in network centrality

The centralities of the averaged TV-DBN coefficients over all successful trials were determined. A two-tailed t-test was used to compare the centrality at each sample for each channel to the total pre-cue samples' distribution over all channels ($p < 0.05$) (Fig. 4.2).

From the 21 high-gamma modulated electrodes, task-related changes in centrality were observed in a subset of 13 electrodes, beginning 0.4-0.6 s following cue presentation. The increased connectivity lasted for approximately 3 s, which encompassed the entirety of the forward reach, the manipulation, and the return to the home location. Of the 13 electrodes with task-related changes in centrality, two showed this activity only early during trials (earlier than .75s post-cue), suggesting they may be relevant to motor planning. Three were limited to the later task phase (later than .75s post-cue), potentially relating to motor output. The remaining 8 electrodes showed modulation during both of these phases of the task.

4.4.2 Time-Varying Centrality Distribution

To quantify the differences between the trial-independent noise in the centrality measure and the task-related centrality modulation, the entropy of the eigenvector cen-

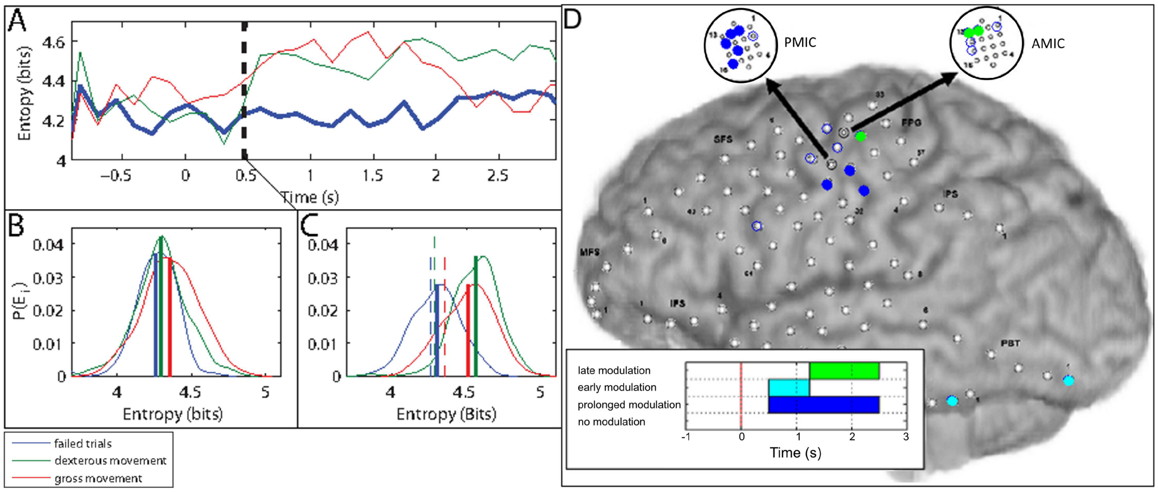

Figure 4.3: (A) The entropy of TV-DBN coefficients in each sample window for the three trial types (failed trials, dexterous and gross manipulation trials). The empirical PDF of the entropy for the three trial types for the pre-reach phase of the task (B) and the movement phase (C). The mean of each distribution is represented by a thick vertical line. The mean of the pre-reach phase is overlaid in (C) for comparison using dashed lines. (D) The electrodes containing statistically significant modulation of centrality over all of the successful trials are filled with color indicating the timing of the increased modulation. Electrodes anterior to the central sulcus appear to have earlier network modulation, while dorsal electrodes show later network modulation.

trality $H(C^1(t))$ was measured in each sample window, as given by the equation:

$$H(C^1(t)) = -\sum_i P(c_i^1(t)) \log P(c_i^1(t)), \tag{4.3}$$

where C^1 is the eigenvector centrality and $P(C^1)$ is the empirical probability mass function of C^1. The entropy represents the information content of the eigenvector centrality, as shown in Fig. 4.3(A-C).

Failed trials and successful trials have substantially overlapping empirical distributions prior to the movement onset. This finding suggests that there were no statistically-significant task-related network differences in the neural data prior to the initiation of movement. This serves as a control, since the randomized trial start time was expected to result in no task-related activity, which is necessary for task-related network changes to occur, prior to cue processing.

After the subject initiated the movement, however, the successful trials of both types showed considerable increases and differing entropy values of their corresponding centrality vectors. This increased entropy was not observed in failed trials, suggesting the network behavior was not modified for these trial types in a consistent manner.

4.4.3 Spatial Distribution of Connectivity Information

Differences in the timing of the significant centrality modulation are shown based on observation in Fig. 4.3-D. Electrodes in adjacent locations showed similar timing in their network modulation. Specifically, the microelectrode PMIC grid and its neighboring macroelectrodes, which were anterior to the central sulcus, showed prolonged network modulation following movement onset. Dorsal electrodes, both on the microelectrode AMIC grid and its neighboring macroelectrodes, had modulation with a later onset, which was sustained for a much shorter duration.

Temporal lobe electrodes showed the earliest modulation, as soon as 100 ms after cue onset (Fig. 4.3-D, light blue). The earlier onset of this modulation relative to motor area activation may be due to the latency of information transfer from visual processing areas into the motor stream. This modulation decreased approximately 1 s after cue onset, consistent with reduced demands of the task on visual processing at the completion of the reach and onset of the grasp.

4.5 Discussion

This study examined the properties of the connectivity measures of neural data obtained using ECoG during a fine motor control task. Eigenvector centrality was used to show importance of individual electrodes to overall network dynamics, which might not be apparent from visual inspection of the connections themselves.

We studied task-related changes in eigenvector centrality to determine the role of sites with high centrality in different phases of the task. The interactions within the microelectrode array, within the macroelectrode grid, and between the two arrays had similar properties. Specifically, the microelectrode task involvement, as inferred from the connectivity timing, was similar to that of the macroelectrodes situated near them (Fig. 4.3-D).

Since the surface area of cortex covered and the inter-electrode distances varied, it is surprising that the networks between and across electrode array types appeared to be comparable.

4.6 Conclusions

Network measures, specifically eigenvector centrality, are shown to have utility in post-hoc analysis of neural activity in this work. In an online system, however, network-based feature selection could be performed after a few trials of performance of the task of interest. Determination of the network measure from these training trials would permit the use of only the connections with the most central nodes for input into a decoder for online control, or for targeted surgical resection planning.

Chapter 5

Task-specific sensorimotor networks revealed by eigenvector centrality in human ECoG

5.1 Abstract

Connectivity measures have recently been used to estimate the propagation of neural activity between recording sites in human electrocorticographic (ECoG) recordings. The high dimensionality of connectivity information resulting from combinatorial explosion with increasing electrode density, however, complicates its interpretation. In this study, we used time-varying dynamic Bayesian network (TV-DBN) connectivity models to estimate task-related neural propagation in ECoG signals as human subjects reached for, grasped, and manipulated different objects. We then used eigenvector centrality, an estimate of the influence each electrode has on the network, to reduce the dimensionality of the results and to study the spatial and temporal distribution of critical nodes in the observed connectivity networks. We observed significant changes in centrality at times near reach onset and during object manipulation ($p < 0.05$), but not immediately following the cue, for both subjects. This suggested that the reach execution concurrent with grasp planning elicited distinct object-type dependent network structure in both subjects. Additionally, the usefulness of centrality as a feature selection technique was shown with an LDA classification model. For both subjects, the decoder using centrality features was shown to outperform the control condition ($p < 0.05$). Our results illustrate the use of network centrality analysis as a tool for comparing and summarizing the complex, high-dimensional spatiotemporal dynamics of movement-related functional networks recorded by human ECoG.

5.2 Introduction

The planning and execution of complex movements involves precise coordination between multiple cortical regions [Tanji, 2001]. An understanding of the functional relationships between brain areas and their role in motor tasks may be obtained from models of connectivity between distinct regions [Rubinov and Sporns, 2010]. If such information was available for clinical decision-making, it could be useful for quantifying the importance of a region to normal function prior to epileptic resection surgery.

In addition, connectivity methods and network measures may be used to characterize seizure activity generated by epileptogenic cortical networks [Franaszczuk et al., 1994, Baccalá et al., 2004, Ortega et al., 2008, Wilke et al., 2011].

Connectivity models based on Granger causality [Granger, 1969a, de Vico Fallani et al., 2015] have been applied to electrocorticographic (ECoG) data to model the dynamics of functional interactions during different cognitive and motor tasks [Baccala et al., 1998, Wilke et al., 2009]. The direct transfer function (DTF) [Kaminski and Blinowska, 1991] is one extension of Granger causality, in which a signal of interest is represented with a multivariate autoregressive (MVAR) model estimated from the history of each neural signal. This approach has also been implemented non-parametrically using Fourier and wavelet transforms [Dhamala et al., 2008].

While the aforementioned Granger causality models are informative, they require data from multiple trials and are therefore incompatible with real-time measurement and single-trial analysis. A recently developed technique for computing dynamic connectivity in single trials called time-varying dynamic Bayesian network (TV-DBN) modeling performs computationally efficient estimation of first-order MVAR model parameters, which can be used as an estimate of inter-electrode connectivity [Song et al., 2009, Benz et al., 2012b].

The true utility of connectivity models lies in their ability to map the recruitment of cortical populations and their functional interactions during specific tasks. Recent literature indicates that cortical functions are not carried out by single areas, but are instead accomplished by cortical networks involving many regions [Knight et al., 2007]. Decoding movements using connectivity information has been shown in ECoG and MEG recordings to outperform changes in spectral power at individual nodes [Benz et al., 2012b, Sugata et al., 2014]. Identifying salient connections from a connectivity map, however, requires either post-hoc manual selection by a trained observer or pre-selection of regions of interest. Additionally, due to the exponential increase in dimensionality from nodes to connections ($n \rightarrow n^2$), connectivity models should only be trained on a limited set of electrodes to prevent over-fitting.

Analysis of ECoG signals often focuses on activity in specific frequency bands, for example: mu (7-12 Hz), beta (12-30 Hz), or high gamma (70-120 Hz). High gamma power modulation has been shown to reflect firing rate changes underlying neuronal populations and has been demonstrated across many functional domains to be a robust index of cortical activation [Crone et al., 2011]. Additionally, changes in high gamma power are detectable in single trials [Flinker et al., 2010a], and are commonly used as inputs to decoding models for brain-machine interfaces (BMIs) [Schalk et al., 2008]. High gamma power exhibits robust task-related changes in effective connectivity during language and motor tasks [Sinai et al., 2005, Towle et al., 2008, Korzeniewska et al., 2011, Marsden et al., 2000], supporting its use in connectivity model analysis.

In this study, we quantified the network properties of task-related high gamma connectivity estimated with a TV-DBN model. We then used a centrality measure [Freeman, 1979, Bonacich, 1987] to further analyze the spatial and temporal properties of connectivity between ECoG sites. The measure of Eigenvector centrality reveals which neural populations contributed substantial information during distinct phases of movement planning and execution. The specific implementation of centrality works well in networks where select nodes have no connectivity, which could otherwise be problematic for ECoG connectivity analysis. Our results suggest that eigenvector centrality can provide a concise representation of the cortical networks recruited during different tasks and which electrodes overlay regions of cortex which help drive that network activity. With additional validation in the future, such a representation could be of potential use in surgical planning or in feature selection for neural decoding models for brain-computer interfaces.

5.3 Methods

5.3.1 Task Participants

Two male, right handed adult subjects were included in this study. ECoG grid implantation was performed for mapping seizure focus and eloquent cortex prior to epilepsy resection surgery. Electrode implantation locations were determined solely based on clinical need.

Subject 1 was a 30-year-old right-handed male who had previously undergone partial resection of his right post-central gyrus and superior parietal lobule. He was implanted with seven eight-contact (2.41-mm length, 6.5-mm center-to-center spacing) platinum depth electrodes placed medially in his right premotor, motor, somatosensory, and posterior parietal cortices. One hybrid-scale depth electrode contained eight 1.57-mm length (5-mm center-to-center spacing) platinum macroelectrode contacts, as well as four microelectrodes interposed between each of the five most distal contacts. The patient also had an eight-contact ECoG strip placed over motor and sensory cortices laterally, with 2.3-mm-diameter exposed recording surface on each contact with 10-mm center-to-center spacing.

Subject 2 was a 20-year old right-handed male implanted with an 8x16 hdECoG electrode grid (Adtech; Racine, WI; 1mm diameter, 3 mm center-to-center spacing) over left sensorimotor cortex for mapping the seizure focus and eloquent cortex prior to epilepsy resection surgery. Placement of the high-density grid was determined based on the semiology of the patients seizures, which consistently began with tingling in the right forearm and spread proximally to the rest of the right upper arm. In addition to the high-density grid, a 2x5 macro grid was placed in left inferior parietal cortex, three 1x4 macro strips were placed in left posterior parietal cortex, left posterior superior temporal gyrus and left middle temporal gyrus, in addition to four eight-contact macro depth electrodes inserted in left inferior frontal and parietal cortices.

Neuronavigation, via the Cranial Navigation Application (BrainLab; Westchester, IL, USA), was used during placement of the depth electrodes. Electrode locations were confirmed by volumetric co-registration of the subject's pre-implantation magnetic resonance image (MRI) with the post-surgical computed-tomography (CT) using the BioImage Suite [Duncan et al., 2004]. For Subject 2, the reconstruction of the high-density grid's electrode locations was modified using intraoperative photos from the implantation and explantation of the high density grid. The electrode locations on a two-dimensional snapshot of the reconstruction were manually adjusted relative to the underlying cortex via rotation, scaling, and translation of the grid in the GNU Image Manipulation Program (GIMP) to optimize the alignment between the grid and prominent gyral and sulcal landmarks present in both the 3D reconstruction and the intraoperative photos. The subjects gave informed consent to participate in this study, which was done in accordance with a protocol approved by the Institutional Review Board of Johns Hopkins University.

Figure 5.1 *(following page)*: (a,b) Implantation location for ECoG arrays. Subject 1 had seven depth electrodes, one hybrid-scale depth electrode, and eight strips. Subject 2 had one high-density grid, one macro grid, three macro strips, and four macro depths. (c) Experimental setup (experimenter pictured). The subject sat in front of the object presentation apparatus, with a platform containing the home sensor placed on the subject's lap. LED lights embedded in the apparatus indicated when the subject should begin a reaching movement, followed by manipulating the indicated object and returning the arm to the rest position to complete a trial. Labels next to electrode arrays indicate the naming convention used to locate them. The labels are used for convenience in the text when indicating relevant electrodes, and do not necessarily refer to the correct anatomical location.

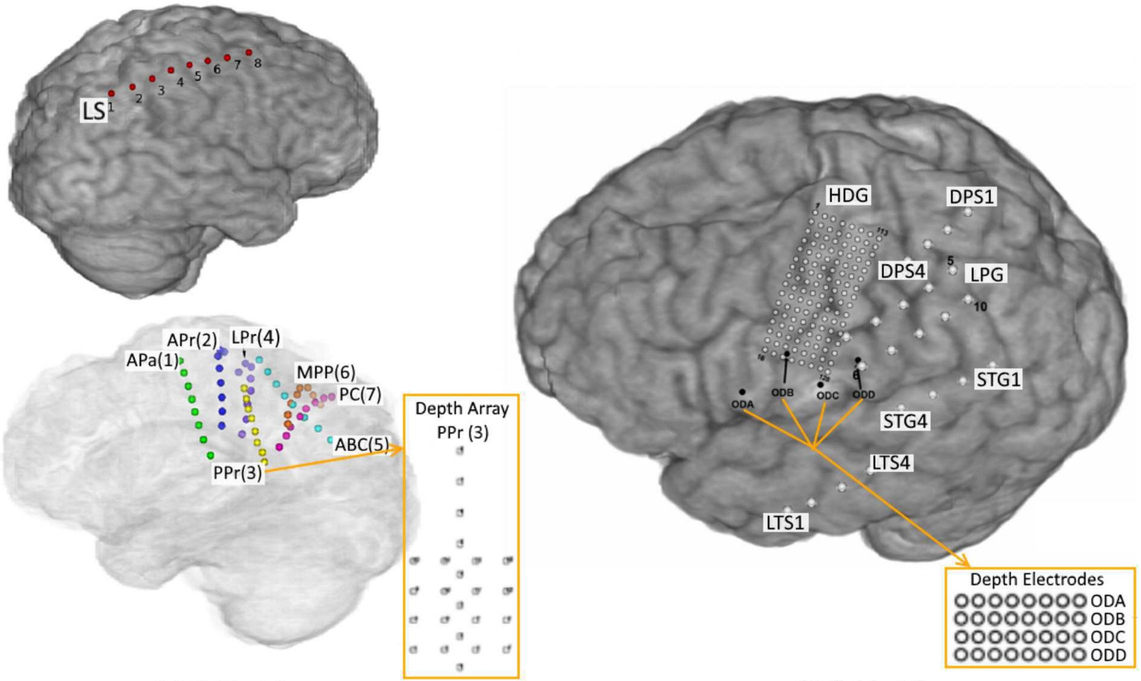

(a) Subject 1

(b) Subject 2

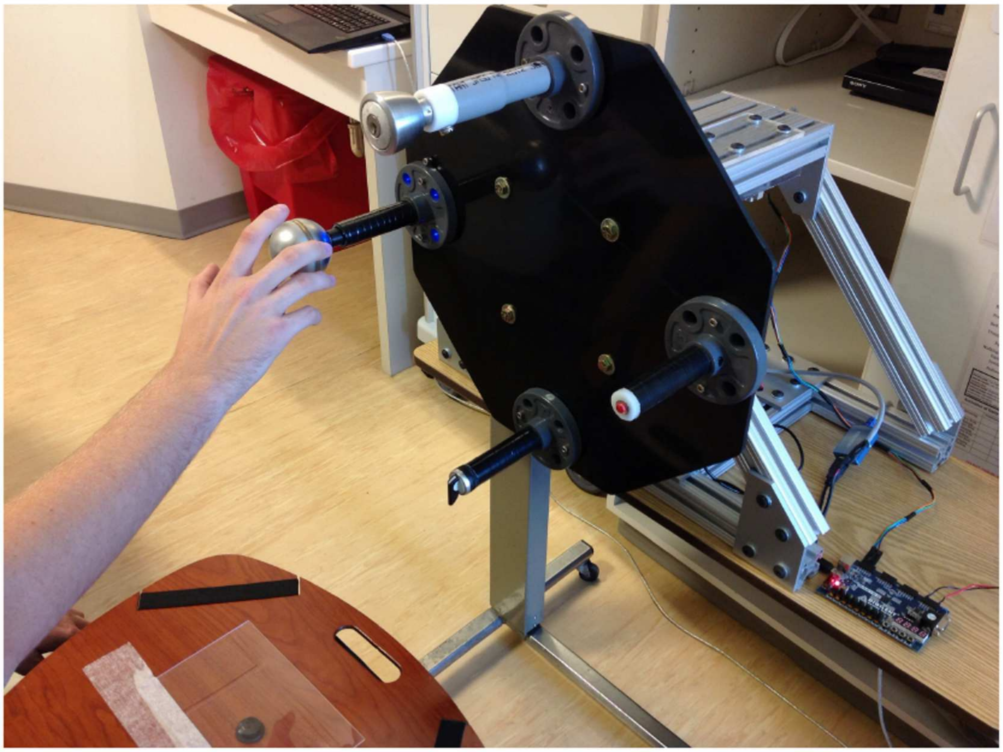

(c)

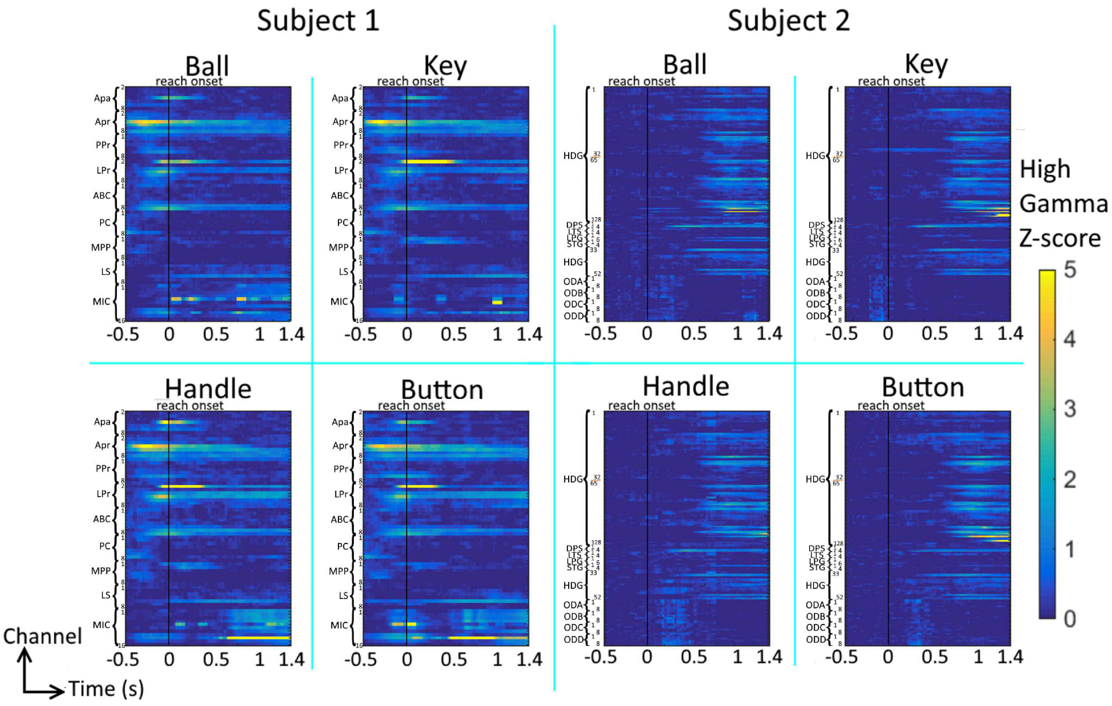

Figure 5.2: High gamma feature modulation. Individual trials were separated by object type and aligned to reach initiation (black vertical line). High gamma power was z-scored to the pre-cue baseline period over all trials before averaging by object type.

5.3.2 Experimental Design

The apparatus for cue presentation had four objects: a push button, a key, a doorknob, and a ball, fixed to an octagonal board at 0, 90, 180, and 270 degrees clockwise from vertical. The apparatus was placed on a table within reach of the subject, who reclined on his hospital bed for the duration of the experiment. Each subject rested his right hand on an electronic home switch in his lap for monitoring movement onset. Each object's attachment to the board was approximately 8 inches from the board's center. The objects were rotated in 90 degree increments between trial blocks in a pseudo-random fashion, presenting each object at four separate positions, but all presentations of each object (i.e., regardless of location) were grouped together for this study. LEDs surrounding the specific objects were used to cue the subject to reach and perform one of the following manipulations: 1) push the button, 2) turn the key, 3) turn the doorknob, or 4) and pull on the ball. The home switch recorded the time of the start of the reach and a switch on the apparatus recorded when each object was manipulated. The task manipulandum and subject implantations are pictured in Figure 5.1.

Subjects 1 and 2 completed 193 and 235 successful trials, respectively. The different manipulations were interleaved in pseudo-random order. Trials were finished when subjects manipulated the object and returned their hand to the home position switch on the base resting on their lap. The inter-trial interval was randomly distributed between 2.5 and 3.5s. Trials had an average duration of 3.5s with a standard deviation of 0.5s between initial release of the home switch and subsequent return.

5.3.3 Signal Acquisition and Preprocessing

ECoG data were recorded with a 128-channel Neuroport system (Blackrock Microsystems; Salt Lake City, UT). Signals were initially recorded at 30 kHz and filtered with a third-order Butterworth analog bandpass filter with cutoffs of 0.3 Hz and 7.5 kHz. Noisy channels were visually identified and excluded from subsequent analysis. Common average referencing was used to remove noise common to all channels. Trials were aligned to one of three task phases for analysis: cue presentation, reach initiation, and manipulation completion. Signals were subsequently digitally band-passed filtered between 16 and 200 Hz. The high gamma spectral power was extracted using the multitaper method [Cox, 1996,Freeman and Zhai, 2009,Yazdan-Shahmorad et al., 2013]. High gamma power was z-scored relative to the pre-cue baseline, for all three types of trial alignment. Trial averaged power modulation centered on reach initiation is shown in Figure 5.2. The TV-DBN connectivity was computed in 128 ms sliding windows with a slide size of 16 ms, from 1.5 s before the cue onset to 1.5 s after the cue onset on the high gamma power signal. Connectivity was computed for all the channels not containing noise. The computed high gamma power was downsampled to 1KHz for subsequent analysis.

5.3.4 Time-Varying Dynamic Bayesian Networks (TV-DBN)

TV-DBN is a method of estimating, within single trials, the time-varying connectivity within a network [Song et al., 2009]. Here, each node in the network is the smoothed high gamma power at a different ECoG electrode. A detailed description of applying TV-DBN models to human ECoG data can be found in [Benz et al., 2012b]. In brief, TV-DBN calculates the time-varying weights by modelling the smoothed high gamma power at each node as a linear function of all of the remaining nodes' smoothed high gamma powers at a fixed time lag:

$$x(t) = A(t)x(t-1) + \epsilon(t),\ \epsilon \sim \mathcal{N}(0, \sigma^2\mathbf{I}). \tag{5.1}$$

where $x(t)$ is the high gamma power of each channel at time t. $A(t)$ is the time varying connectivity weights, and $\epsilon(t)$ is Gaussian distributed noise. Gaussian smoothing is used to reduce noise and provide more stable estimates.

Connectivity weights were z-scored to the mean and standard deviation of the 1.5s to 0s prior to cue period distribution of connectivity values over all trials, performed separately for each channel. This resulted in individual connectivity values representing the number of standard deviations above the baseline average in the strength of individual connections.

5.3.5 Centrality

Each site's total strength was summarized using eigenvector centrality. Eigenvector centrality quantifies each site's total strength of connections to the entire network [Freeman, 1979, Page et al., 1999] through a recursive process. The connectivity matrices were averaged for each object type and alignment parameter, then the centrality vector of the connections was determined at each time point, t. The rows of the connectivity matrix, $A(t)$ were divided by their individual sums to create a stochastic matrix, $S(t)$, which ensured that a centrality vector exists for any S.

To guarantee a minimal amount of connectivity from all nodes, the Google matrix $G(t)$was formed. This matrix describes the directional interactions of the network [Ermann et al., 2013]. The Google matrix consists of the linear combination of $S(t)$ with a matrix consisting of 1's for all elements ($\mathbf{1}$) [Page et al., 1999, Austin, 2006]:

$$G(t) = \alpha S(t) + (1 - \alpha)\frac{1}{n}\mathbf{1}, \tag{5.2}$$

where n was the number of rows in S, and $\alpha = 0.85$ was used as an adequate compromise between the connectivity of the actual network, and the situation where all of the nodes were connected with equal strength [Whang et al., 2015].

Eigenvector decomposition was performed on the Google matrix, G, and the eigenvector corresponding to the maximal eigenvalue of G was denoted $C^1(t)$. Thus, the following equation is solved for the time-varying Google matrix $G(t)$:

$$G(t)C^1(t) = \lambda^1(t)C^1(t), \tag{5.3}$$

where λ indicated the eigenvalues in descending order, and C was the corresponding eigenvector. The time-varying centrality matrix was notated $C^1(t)$. The entries in $C^1(t)$ indicated the total information flow from each electrode in the network at sample t. This analysis was limited to output centrality, as a means of quantifying the influence each electrode had on the network, but could be trivially modified to apply to electrode inputs.

To compute the statistical significance of centrality values at each time point, the centrality of the z-scored TV-DBN connectivity ($A(t)$ matrix) weights was first computed separately for each trial. Trials for each object type were then grouped together, and the distribution of each (channel, time) pair was compared to a baseline distribution of centrality values. The baseline distribution was composed of connectivity weights calculated from non-overlapping windows of data prior to cue presentation. A two-tailed Student's t-test was used separately for each (channel, time) pair to find significance at the $p < 0.05$ level, after false discovery rate (FDR) correction for multiple comparisons.

5.3.6 Central Electrode Subset Comparison

The time-varying centrality vector directly reveals modulation with task execution, but we were also interested in seeing differences in this vector with task conditions, i.e., with different objects being manipulated. Electrodes with significant centrality at any time point during the performance of the task were added to an object-specific list of electrode subsets. Separate lists were generated for the three different trial alignments: cue presentation, reach initiation, and object manipulation. To compare the cortical network involvement for different object types, and separate task phases, the overlap of the electrode subsets with significant centrality for each object type was computed by the Jaccard distance [Jaccard, 1912, Strehl et al., 2000]:

$$d_j = \frac{|set_{cond1} \cup set_{cond2}| - |set_{cond1} \cap set_{cond2}|}{|set_{cond1} \cup set_{cond2}|}, \tag{5.4}$$

where set_{cond1} and set_{cond2} were the subsets of electrodes with significant centrality in any time-point for the specific trial conditions $cond1$ and $cond2$. The Jaccard distance normalizes the similarity of subsets such that identical sets had a Jaccard distance of 0, and sets with no overlap had a value of 1.

The Jaccard distance revealed total differences in central electrode sets, but the timing information of those differences was lost. To elucidate timing-related differences in centrality, the pairwise Pearson's linear correlation coefficient (r-value) was computed separately for each pair of objects' centrality vectors.

A nonparametric permutation test was performed to determine the significance of differences between subsets of highly-central electrodes [Rokni et al., 2007]. The test was performed by permuting the labels for the trial types of the TV-DBN matrices before averaging. Centrality was then computed on the permuted averages. Statistical testing was then performed for each time-window's centrality vector, and similarity was found between pairs using either the Jaccard distance or correlation for the respective test. The resultant matrix of centrality vector similarity values was stored for 5,000 randomized permutations.

5.3.7 Object Classification

To assess the utility of the centrality method for improving decoding accuracy, Linear Discriminant Analysis (LDA) was used to classify the object type for each trial [McLachlan, 2004]. The high gamma power at the time of object contact was used as the input to the LDA classifier. The electrodes used as the input were varied between:

1. The control case: any electrode which did not contain obvious noise
2. Electrodes with significant *high gamma power* within this time-window relative to baseline
3. Electrodes with significant *centrality* within this time-window relative to baseline

Significance was determined by a t-test which compared the distribution of each channel's high gamma power in the selected time-window over all trials to its baseline distribution. Significance was determined at the 0.05 level after a Bonferroni correction was used. A subset of these three electrodes sets was compared as the input to the model for an increasing number of selected electrodes, up to the full sets. Ten-fold cross-validation was used to prevent over-fitting and provide a reliable measure of decoding accuracy, consistent with what would be expected if the method were used online. The cross-validation was repeated 100 times for a different subset of n electrodes within each category, where $1 <= n <= N_c$, where N_c is the number of electrodes within category c.

5.4 Methods validation - Centrality of TV-DBN simulation

5.4.1 Model construction

To validate the TV-DBN and eigenvector centrality method, the network measures were compared for synthesized ECoG signals generated to be neurophysiologically realistic [Crone et al., 1998]. The simulation was separated into two separate phases of differing structure within a 4-node network. Each channel consisted of three seconds of sixth-order AR-model generated data, using randomly generated AR coefficients. The data was then bandpass filtered to extract the high-gamma component using multi-tapers. The simulated network initially consisted of the first channel influencing the three other channels exclusively. After three seconds of simulated time, the structure was switched to a network where the channels cascade. Signals were then contaminated with Gaussian-distributed white noise, delayed by 16 ms (so as to be physiologically reasonable) and added to the signals they influence. Influence is related to noise magnitude by the following equation:

$$x_t(w) = infl_{s,t}(w) * x_s(w) + (1 - infl_{s,t}(w)) * \mathcal{N}(0, 1), \tag{5.5}$$

where $infl_{s,t}(w)$ represents the fraction of influence the source node has on the target within window w. This simulated the effect of the source channel driving the activity of the target channel in the high-gamma band.

In the second network, the signals were defined by the following steps, with the addition of a 16 ms delay between each step: 1) channel 1 contributed equally to all of the other channels' signals, 2) channel 2 then contributed equally to the signals at channel 3 and 4, 3) channel 3 contributed to channel 4's signal. TV-DBN was then calculated with a 128 ms window size and a 16 ms slide size. The results of the TV-DBN calculations were averaged over the three second trial period. The simulations were repeated 50 times for each level of noise. The distribution of centrality values over all runs was computed separately for each level of noise. The average coefficient magnitudes were plotted as the size and red saturation of the arrows in Figure 5.3. Centrality values for individual channels with a significantly different distribution than the control case ($p < 0.01$; Bonferroni corrected) were indicated with stars in the figure.

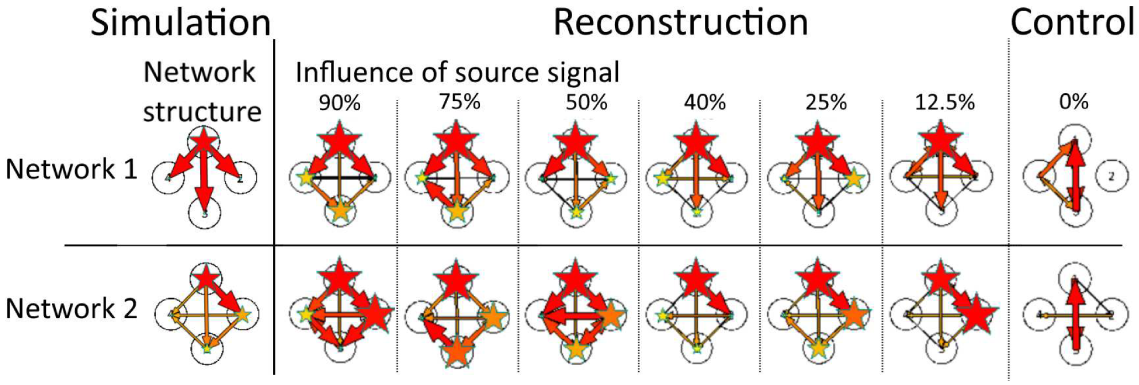

Figure 5.3: Comparison of the underlying network to the TV-DBN calculated for the simulated data, averaged over 3 second windows. The simulated data consists of four randomly generated sixth-order AR signals, with an influence on each other as illustrated by the first column. The first network was simulated for 3 seconds, then transitioned to the second network and sustained for 3 more seconds. For the 2nd - 7th columns, the source signals influenced a percentage of the target signals as indicated by the column heading. The TV-DBN measures within these periods were then determined, and the connection strengths were averaged, and displayed as arrows with the width and red saturation indicating connectivity strength. Stars indicate centrality of each node in these networks. The final column shows these measurements under the control condition, where none of the nodes' signals has any influence on the other nodes.

5.4.2 Interpretation

TV-DBN was able to reproduce the simulated network structure with good fidelity, even with increasingly weak network influence. While the first and simpler network was robust to the presence of noise, showing connectivity and centrality closely matching the original structure while the influence was at or above 25%, the second network was less consistent. For the second network, the fourth node (clockwise from the top) consistently shows the lowest centrality, but the second node is often more central than the first node after the simulation. Both nodes have large influence on all of the remaining nodes, so this is not unreasonable given the extent of noise in the signals. Although none of the components were of zero magnitude, this was to be expected because of the addition of a constant value weight to the stochastic matrix, allowing for spurious connections between nodes.

5.5 Results

Trials were separated into those corresponding to each of the four objects, irrespective of presentation location. Trials were aligned separately for this analysis according to the timing of three events: cue presentation, reach initiation, and onset of object manipulation.

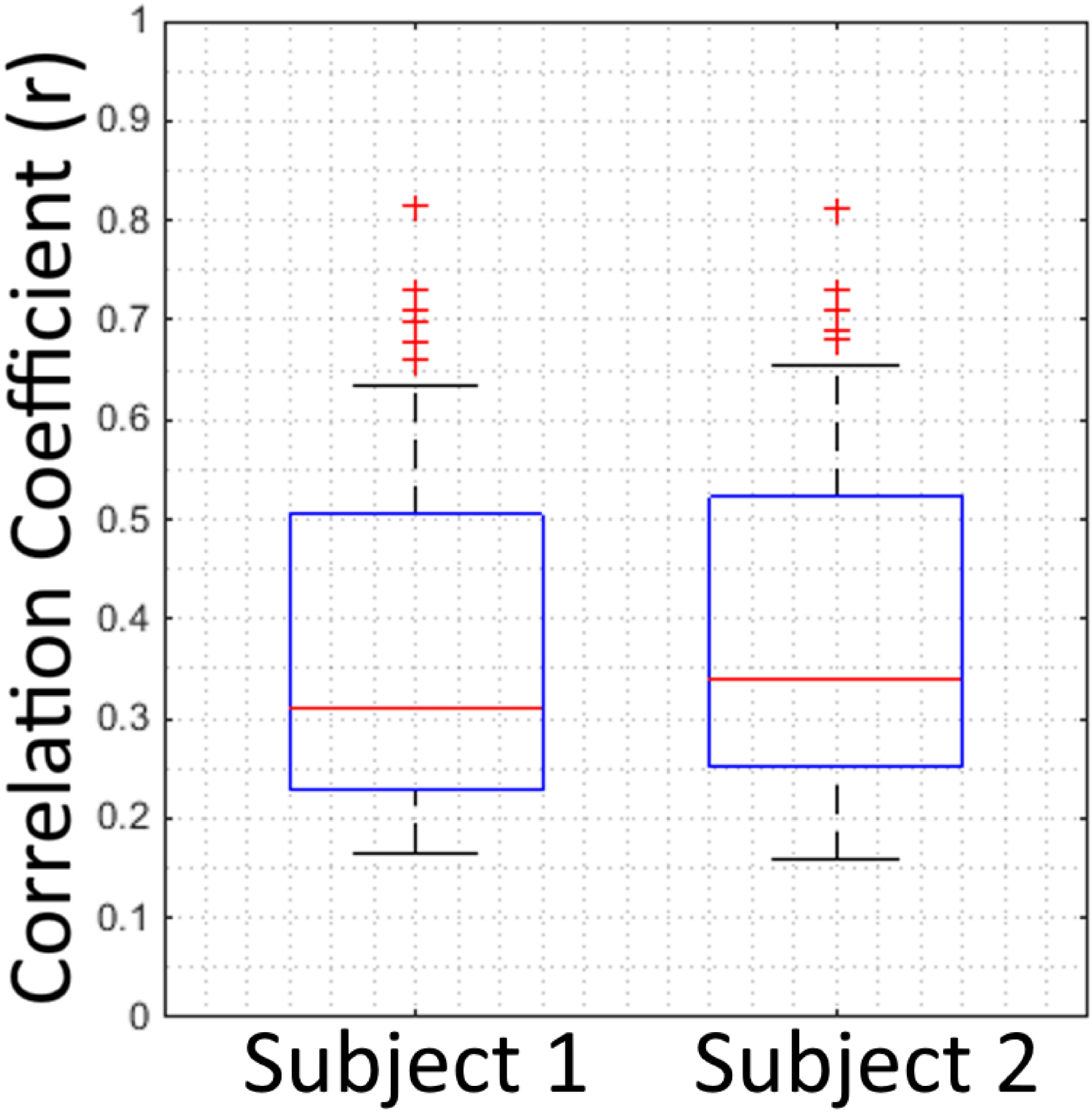

Figure 5.4: Distribution of the single channel correlations between the centrality and high gamma power feature for each subject.

5.5.1 Correlation between centrality and high gamma power

To determine if centrality represents more than a simple linear transformation from high gamma power, the cross-correlation with no lag was taken between the individual high gamma power features and the corresponding centrality features (Figure 5.4). the r-value of Pearson's correlation coefficient was used to allow for the detection of negative correlations. For both subjects, r-values ranged between 0.15 and 0.85, with a median value near 0.35. This suggests that the correlation varied considerably across channels, but none of the centrality features were directly dependent on the high gamma power for the same electrode.

5.5.2 Changes in network centrality during different task phases and object types

Figure 5.5 compares the statistically significant trial-averaged TV-DBN centralities observed using different phases for alignment. Task-related changes occurred in a subset of ECoG sites, beginning no sooner than 250 milliseconds following cue presentation. For Subject 1, this subset contained 28 of the 70 ECoG sites. For Subject 2, this subset contained 60 of the 162 ECoG sites. For both subjects these subsets contain electrodes which may or may not be present in all three of the alignment periods. The increased connectivity lasted for approximately 1.5 s, which encompassed the en-

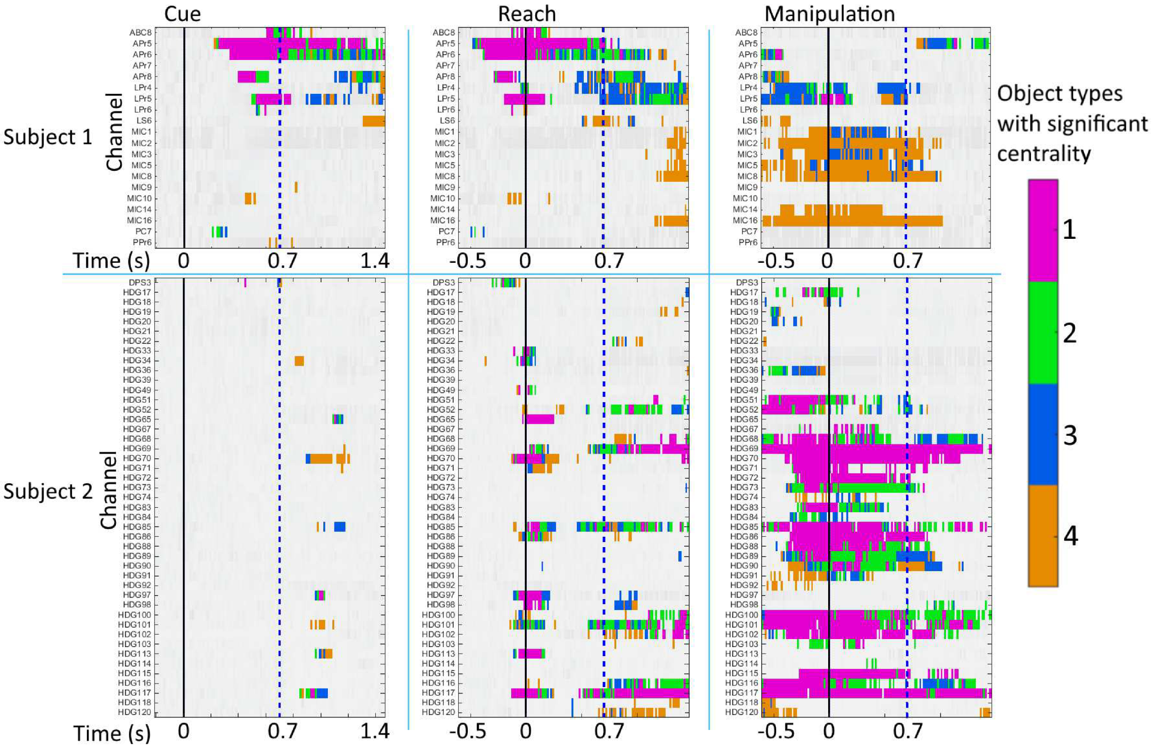

Figure 5.5: Time-varying centrality vector over channels with significant modulation for both subjects for the button object. Centrality was calculated for the trial-averaged TV-DBN matrices. Colors indicate the number of objects (of 4 total, including button) that exhibited significant activation at a given (channel, time) pair. Only the channels which had significant activation for the button object are shown. Electrodes with centrality vector values which were statistically significant (t-test; $p < 0.05$; FDR corrected for multiple comparisons) are represented by colored pixels. The overlap in object types that had statistically significant centrality for a particular time window and channel pair is indicated by the color of those pixels. Vertical dash blue lines indicate the timing of the centrality shown on the electrode layout in Figure 5.6.

tirety of the task performance. For Subject 2, 13 electrodes had significant changes in centrality during the cue-aligned period, all following the cue presentation. This increased centrality was very transient, only lasting for tens of milliseconds at a time. Subject 1, however, had sustained increases in centrality following cue, lasting for 200 – 500 ms in each central electrode.

One clear object-related difference can be seen for Subject 1 in Figure 5.6, where the button, and to a lesser extent the handle, had significant centrality in several of the hybrid macro-micro depth electrodes. This depth array was placed ventral relative to the other electrodes on the cortex. The handle's spatial distribution was more constrained in these depth electrodes, relative to the button. Similarly, the number of successive time-windows containing significant centrality is more limited, as seen in Figure 5.5.

Figure 5.6 *(following page)*: Significance of the centrality of the four object types is indicated at the alignment points, shown in Figure 5.5 with vertical lines, laid-out spatially. The object type of each electrode which had statistically significant centrality at the specified time-point is indicated by the markers. These shapes correspond to the object type indicated by the legend on the right. The specific alignment point and time-window relative to the trigger are shown above each column.

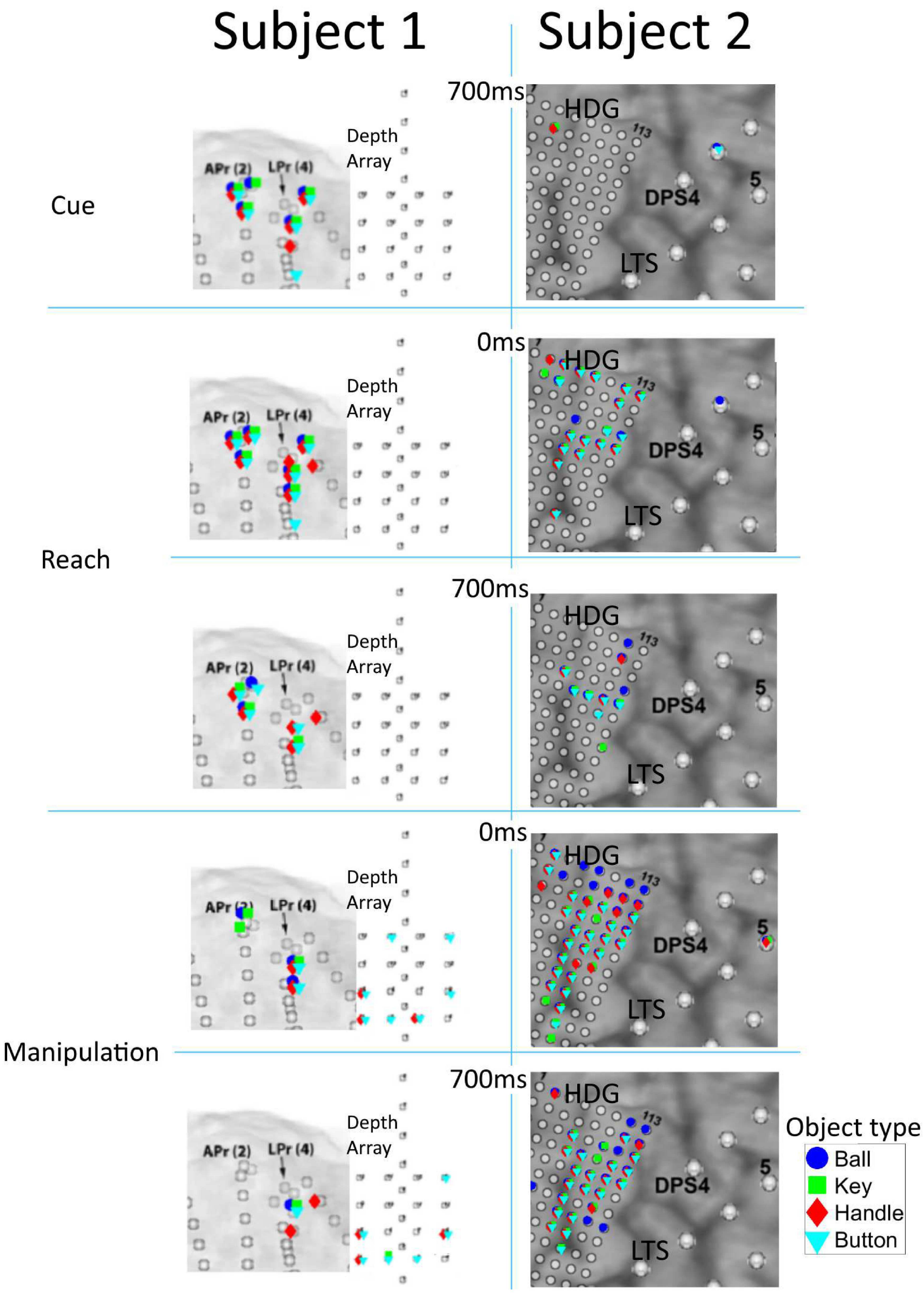
Subject 1
Subject 2
Cue
Reach
Manipulation
700ms
0ms
700ms
0ms
700ms
Depth Array
APr (2)
LPr (4)
HDG
113
DPS4
5
LTS
Object type
● Ball
🟩 Key
♦ Handle
▼ Button

5.5.3 Behavioral phase selectivity of centrality spatial distribution

Many of the electrodes with significant task-related changes in centrality were the same across task phase and object type. Figure 5.7 illustrates the degree of uniqueness in membership among these subsets of electrodes for different object types. Pairs of object types with statistically significant differences in the central electrode sets are overlaid with asterisks ($p < 0.05$; Bonferroni corrected for multiple comparisons). Significant differences for both subjects were only seen during the active movement phases of task performance, and not between all pairs of object types. There is no obvious pattern in which object types had the greatest specific differences, however.

The coverages differed between the two patients and the types of arrays implanted were different. However, both subjects showed similar trends in the properties of their centrality vectors. In particular, after the cue, both subjects had a sparse set of central electrodes which only had significant centrality for a few consecutive time windows. The sets of these electrodes with significant centrality for at least one time window for specific alignment points and object types are called the central subets. During the reach phase, the central subsets became larger for both subjects, and the centrality was maintained for a longer period of time. The manipulation phase showed the most centrality for both subjects, and it was sustained for a major portion of the task performance.

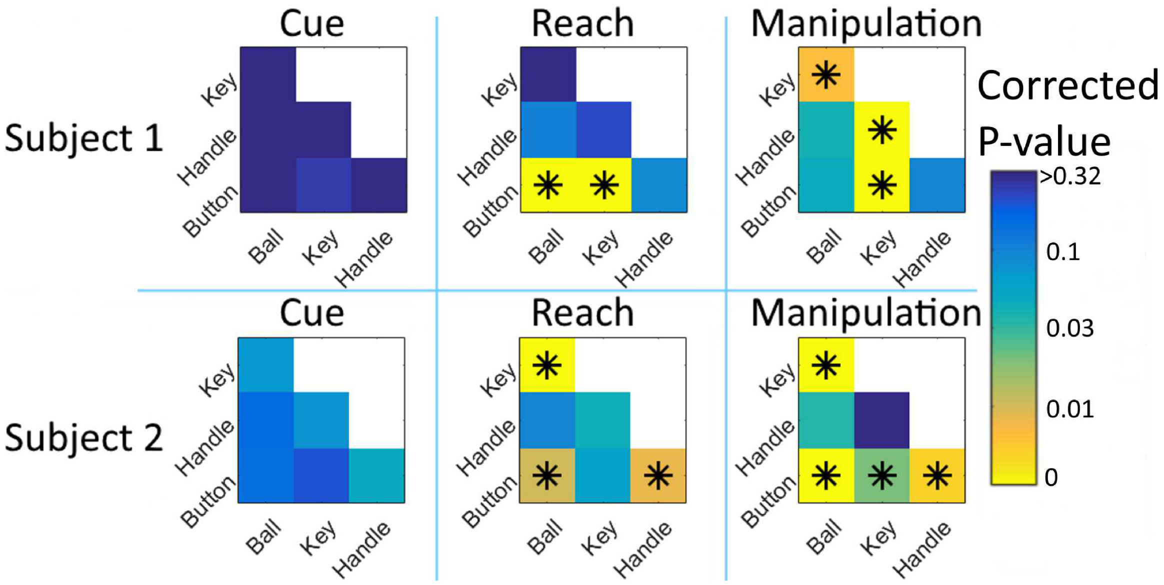

Figure 5.7: Statistical significance of the task-specificity of the electrode subsets. Central electrode subsets were those with statistically significant centrality values, calculated separately for each object type. Task-specificity was determined as the Jaccard distance between the sets of central electrodes for each alignment period and object type. The three columns represent windows averaged from 1.5s before to 1.5s after the cue, reach, and manipulation events, from left to right. Significant differences between sets of electrodes are indicated with asterisks (Permutation test; $p < 0.05$; Bonferroni corrected for multiple comparisons). The color-bar indicating significance is on a logarithmic scale to accentuate very small p-values. Object type self-comparisons would have a p-value of 1, since they contain the same electrode sets, and are not shown.

5.5.4 Absence of object selectivity specific to centrality time course

For both subjects, the cue period showed no statistically significant differences in centrality correlation. This suggests that the network connectivity at this phase of the task was not object dependent. Subject 2 showed significant centrality differences starting with reach onset and continuing through object manipulation. Subject 1 only showed significant differences during physical contact with the object, starting later in the trials.

The correlation analysis did not deviate substantially from the Jaccard distance seen in Figure 5.7. This is in support of the previous observation that centrality is sustained with a similar time-course in the central electrodes, irrespective of object type. This does not contradict the finding that the central electrode subsets themselves vary with object type.

5.5.5 Object Classification

The reliability of centrality as a method for feature selection was determined for both subjects, as shown in Figure 5.8. For subject 1, high gamma and centrality electrode selection performed comparably. For subject 2, however, centrality electrode selection generally outperformed high gamma electrode selection. With a larger portion of the selected electrodes used as input, centrality does significantly better than high gamma selection. For subject 2, decoding accuracies decreased beyond 90 electrodes up to all 162 channels. High gamma and central sets contained at most 50 electrodes up to which point the trend of accuracy increase with added input features was maintained. For subject 2, with 20 or more central electrodes used in the model, control electrodes always performed worse on average over 100 runs with any number of input features.

5.6 Discussion

In this study, we have described a method to determine the important sites of network activity based on the connectivity information from multi-site neural recordings. We

---

Figure 5.8 *(following page)*: **Decoding comparison.** An LDA decoder was trained to predict task-type based on the high-gamma power present in a subset of electrodes. The centrality subset was determined based on the presence of centrality > 0.75 standard deviations when compared to the baseline. The high gamma subset was determined based on the presence of high gamma power > 0.5 standard deviations when compared to the baseline. The horizontal axis indicates how many of the electrodes contained in the subset were used for each decoder. The members in these subsets were randomized 100 times, and the distribution of decoding accuracies over these runs is indicated by the lightly colored shaded regions. Statistical significance is indicated by asterisks, based on a one-tailed Student's t-test with Bonferroni multiple comparison correction ($p < 0.05$).

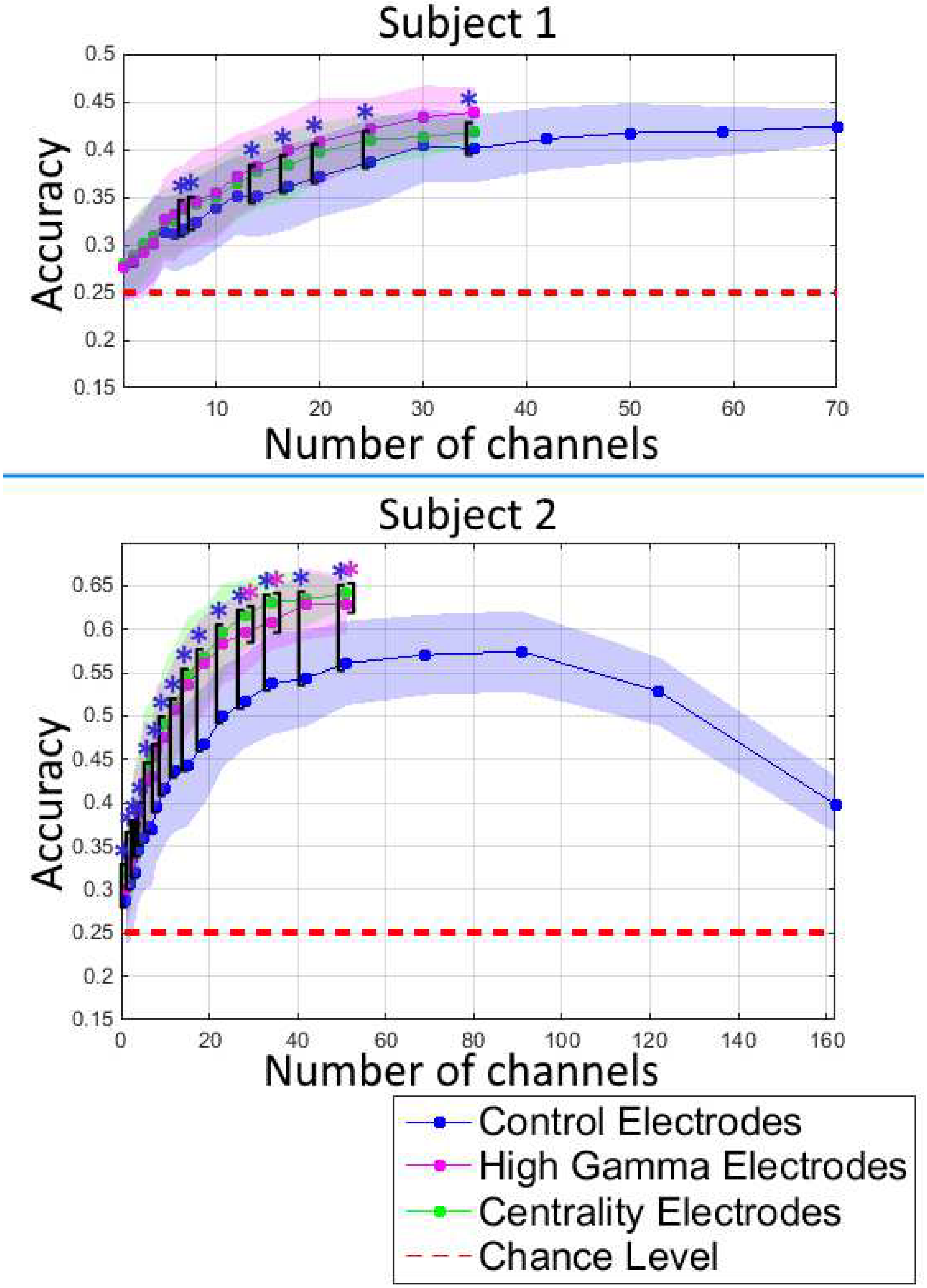
Subject 1
Accuracy
0.5
0.45
0.4
0.35
0.3
0.25
0.2
0.15
10
20
30
40
50
60
70
Number of channels
Subject 2
Accuracy
0.65
0.6
0.55
0.5
0.45
0.4
0.35
0.3
0.25
0.2
0.15
0
20
40
60
80
100
120
140
160
Number of channels
Control Electrodes
High Gamma Electrodes
Centrality Electrodes
Chance Level

have analyzed ECoG data obtained during the performance of a reach-to-grasp task. By applying the centrality measure to connectivity coefficients from the TV-DBN model, we have shown task-related differences in the performance of the task.

5.6.1 Centrality of Electrodes

Time-averaging of the TV-DBN connectivity matrices locked to different phases of the task reveals that different electrodes have unique time-courses of centrality modulation for sustained periods (Figure 5.5). Perhaps more interestingly, some electrodes only show pronounced centrality for certain trial phases, and with certain object types. A good example of this is in the micro-electrodes(PPr(3); Figure 5.6) for Subject 1, with the hybrid depth electrodes showing only manipulation-related centrality, mainly for the button or handle objects. Conversely, for Subject 2, electrode DPS3, which is posterior to primary somatosensory cortex, shows only modulation prior to reach onset, and only for the ball or button objects (Figure 5.6). The time course of DPS3's centrality, along with its anatomical location, suggest that it's involved in cue processing or motor planning, Overall, this supports the claim that those electrodes only become important to the network during a specific behavioral stage in the performance of the motor task.

5.6.2 Task-related Network Evolution

Both subjects showed remarkable task-related changes in both the time-course of centrality modulation (Figure 5.5, as well as the localization of highly central electrodes (Figure 5.6). The robustness of this result when considering that the electrode placement differed between the two patients and the types of arrays implanted were different is supportive of the general applicability of the methodology to similar datasets. This was seen consistently in both the tightly constrained cue-related activity, as well as the stable increases in centrality with task progression. These patterns were present across both reach and manipulation, with less constrained localization of central electrodes in the later task-phase. It has been shown that ECoG spectral features can represent task specifics at the resolution of individual fingers in somatosensory areas [Miller et al., 2009]. The networks used were modeled on high-gamma spectral features, as was the input to our connectivity model.

Subject 2 also had many of the same central electrodes across both reach and manipulation alignment. The cue alignment relative to both of these phases, however, had a unique set of central electrodes. The lack of the reach and movement central subsets being represented during cue is most likely due to the extensive peri-Rolandic coverage of Subject 2. While this configuration allows for a strong representation of the network activity involved in both movement and sensory feedback, it precludes earlier areas of the visuo-motor pathway from being represented in these results, due to the lack of Occipital and posterior Parietal lobe coverage. Though much is still unknown concerning the neural representation of motor control [Koike et al., 2015], it has been shown that high-gamma activation in these areas occurs prior to movement onset [Sun et al., 2015].

5.6.3 Object Related Network Differences

Both subjects had clear object related differences in centrality distribution (Figure 5.7). The electrodes which had significant centrality modulation show object related differences (Figure 5.6). The time-course of this activation did not show clear object-related differences outside of those contained in the central subsets' spatial distribution, however (Figure 5.5).

Despite different electrode placements, there was still a clear dorsal-ventral distribution of central electrodes along the sensorimotor cortices for both subjects, which suggests a somatotopy. Ball manipulation trials had a more dorsal representation of central electrodes, while handle and button trials had more ventral centrality along the electrode arrays. The key object did not show consistent trends across both subjects (subject 1 appears to have had a dorsal representation of the key trials, while subject 2 had a more ventral one, around the initiation of object manipulation). This may be due to differences in how the two subjects performed the different manipulations. ECoG spectral features have previously been shown to contain grasp specific information correlating hand posture to neural activity [Pistohl et al., 2012, Chestek et al., 2013]. The exact localization of task-modulation with distinct complex movements, however, has been shown to be inconsistent across patients [Pfurtscheller et al., 2003], fitting with our results.

Subject 1 showed substantially increased cue-aligned centrality that carried over into the reach-aligned centrality. This centrality was activated in a nearly identical manner in terms of location and time-course for all four object types, as indicated by the prevalence of statistically significant centrality values in Figure 5.5. Subject 2 generally showed less central electrode set overlap across object types with cue-alignment than Subject 1. This reduced overlap was in part due to the shorter time-course of cue-aligned centrality for this subject, in addition to the reduced electrode sets included in the cue-period activation patterns. Conversely, Subject 2 had far more centrality activation with manipulation than Subject 1. This may have been a result of the dense coverage of sensorimotor areas provided by Subject 2's high density grid, which allows for more fine-grained differences in network structure to be represented.

5.6.4 Decoding

We have shown the feasibility of centrality as a down-selection technique for input selection to a classifier. While similar grasp decoding studies have had higher accuracies /citemarquez2009control, pistohl2012decoding, these studies were not limited to using the high gamma feature and in general had better hand-area motor cortical coverage.

Both subjects showed continued improved decoding accuracies with a larger subset of high gamma or central electrodes. In both cases, the intelligent electrode selection always performed similarly, or outperformed naive electrode selection. Even in the best case, subject 1 had an accuracy rate of 45%, while subject 2 had an accuracy of 65%. While this suggests that these electrodes contain discriminative information for the grasp category in the high gamma band, it would not be practical to implement the method directly in a BCI, due to the high error rate.

The eventual decrease in decoding accuracy with added channels for subject 2 suggests that much of the information contained in the electrodes is not useful for object type decoding. This suggests that a dimensionality reduction technique used on the input features, such as principal component analysis, such as that used in [Wang et al., 2009] could improve accuracies. That would be outside the scope of this article, however, since the goal was to see if highly central electrodes contain task-discriminative activity.

5.6.5 Applications

Network measures, specifically eigenvector centrality, are shown to have utility in post-hoc analysis of neural activity in this work. In an online system, however, network-based feature selection could be performed after a few trials of performance of the task of interest. Determination of the network measure from these training trials would permit the use of only the connections with the most central nodes for input into a decoder for online control, or be used for providing highly relevant analysis prior to targeted surgical resection planning. The Google matrix G used in finding the centrality vector has all positive elements, making it a primitive matrix for which it is possible to find an indirect connection from one node to another of any arbitrary length. This is a necessary precondition of the power method for computationally efficient calculation of the stationary vector (extended in [Haveliwala et al., 2003, Kamvar et al., 2003]). As electrode density increases, the power method allows the algorithm to continue to be feasible for time-constrained (e.g., real-time) calculations.

Our results suggest potential usefulness in brain-machine interfaces with the use of ECoG signals for control of a prosthetic device. The methods presented here may be extended to local field potential recordings, or applied to different task paradigms such as language processing. Centrality measures could potentially be used to select a subset of network nodes from all recording sites for which network dynamics could be computed much more efficiently for real-time control of a prosthetic limb. While we have shown that using the high gamma power of the most central electrodes always outperforms a naive electrode selection technique, it is possible that using the centrality features directly could further improve decoding accuracies.

5.7 Conclusions

We have used eigenvector centrality to better understand the complex dynamics of functional connectivity in human ECoG recordings during cued reaching and manipulation of different objects. In particular, centrality estimates the importance of individual recording sites to overall network dynamics. This information may not be apparent from visual inspection of the connections themselves. Application of the centrality method results in a substantial reduction in the dimensionality of network connectivity, while preserving the essential features of the network and identifying recording sites of particular importance. In this paper, we have illustrated how centrality analysis facilitates comparisons between the temporal and spatial features of network dynamics observed during different task phases and conditions. Specifically, the temporal differences in the network are manifested by changes in the most central nodes, which drive the overall network behavior. The spatial distribution of these nodes as observed correlate with the specifics of task performance. While some channels have a high correlation between their centrality and high gamma power, this was not a general trend, as the median correlation was around $r = 0.35$ for both subjects, suggesting centrality is not directly dependent on this single channel feature. A high gamma power LDA decoder was trained using channels selected based on subsets of central electrodes, high gamma power electrodes and all of the electrodes. For subject 1 centrality generally outpeformed the control condition. For subject 2, who had more dense sensorimotor coverage, the central channels also performed as good as or better than the high gamma electrodes in all cases on average. Together, these analyses can help inform neuroscientific understanding of brain function, in addition to allowing for a more practical BCI application resulting in a reduction in decoder input feature size.

Chapter 6

Brain State Detection in Human ECoG Using Stability Clustering

6.1 Abstract

The determination of underlying brain activation patterns during the execution of a complex task generally involves presupposition of the number of processing phases for the task, and the timing of each phase, based on when the stimuli were presented. For a complex task such as object naming, the stimulus processing and response execution can vary in timing and duration across trials, while the exact number of measurable distinct processing phases is electrode coverage dependent. Six subjects were presented with a series of images of unique objects, and were subsequently required to name the objects displayed during an electrocorticography (ECoG) recording session.

K-means clustering, with the number of clusters determined by the optimization of the cluster label stability between subsets was performed on high gamma power in an unsupervised fashion. High-gamma activation separated into a limited number of unique clusters in a task-related manner, consistent across both sets of trials for all subjects. A hidden Markov model was also trained for each subject, using the most stable number of clusters from k-means. Despite timing information not being accounted for by the clustering method, high consistency between the labels of localized time-windows was observed. This supports the clustering methodology's potential usefulness for the determination of task engagement, in addition to its utility in separation of activity based on underlying unobservable variables in a reliable time-locked manner across trials. Localized changes in brain activity with repeat performance were detectable in the clustering analysis, restricted to a confined subset of electrodes for each subject, though with varying location. The described method has wide-spread applicability to cortical mapping analysis and to the study of complex cognitive tasks.

6.2 Introduction

The execution of an object naming task requires the precise coordination of multiple cortical regions [Sinai et al., 2005]. While trial-averaged analyses reveals cortical processing in relation to task stage, variability in the timing and duration of cortical processing and response articulation can result in blurring. Single trial analyses is not susceptible to this effect, and so can lead to deeper understanding of network activity during task execution [Flinker et al., 2010b]. If such information was available for clinical decision-making, it could be useful for quantifying the importance of a region to normal function prior to epileptic resection surgery.

Analysis of ECoG signals often focuses on activity in specific frequency bands. In this work we focus on high gamma (70-120 Hz). High gamma power modulation has been shown to reflect firing rate changes underlying neuronal populations and has been demonstrated across many functional domains to be a robust index of cortical activation [Crone et al., 2011]. Additionally, changes in high gamma power are detectable in single trials [Flinker et al., 2010a], and are commonly used as inputs to decoding models for brain-machine interfaces (BMIs) [Schalk et al., 2008].

Clustering analysis in ECoG has been shown to overlay stimulation mapping areas' functions with good specificity in gamma band when correlation is used to measure connectivity [Ko et al., 2013]. Clustering analysis of resting state spectral features has been shown to accurately cluster in isolation the areas expected to show modulation in the particular frequency bands implicated in their functional role [Groppe et al., 2013], though this analysis was limited to sub-gamma band features. Clustering analysis has been applied to the problem of seizure detection in the high gamma band, successfully localizing the region of seizure onset [Liu et al., 2015].

For clustering to meaningfully partition the data, a logical choice for the number of clusters should be imposed [Sneath et al., 1973]. There exist a multitude of techniques for determining the appropriate number of clusters in a data-dependent manner [Milligan and Cooper, 1985]. One such technique involves minimizing the average distance between each cluster centroid and its members [Ball and Hall, 1965]. A similar technique involves minimizing a function of the spread of each cluster's members [Hubert and Levin, 1976]. A common optimization technique involves minimizing an information criteria [Goutte et al., 2001], such as Akaike Information Criteria [Akaike, 1974, Burnham and Anderson, 2002], as in [Pelleg et al., 2000] and [Žalik, 2008].

It has been shown that when the same stimuli are presented in a response task multiple times to subjects, their response times are reduced [Forbach et al., 1974, Scarborough et al., 1977]. It has been suggested that this is the result of the engagement of distinct cortical pathways which are activated for primed stimuli retrieval [Hayman and Tulving, 1989, Schacter et al., 1991]. Specifically, this "perceptual representation system" is distinct from the episodic memory implicated in the response to the initial unprimed stimulus [Tulving and Schacter, 1990], a suggestion supported by the reduction in reaction time upon repeat presentation.

Our hypothesis is that by separately clustering over the ECoG recordings during initial and repeat single trial performance, it will be possible to detect functional differences in brain activity during task performance based on the cluster memberships and time-courses. To test this hypothesis, we utilize ECoG recordings acquired during the performance of a picture naming task. To find the most stable clustering over trials, we have selected a stability clustering criteria [Lange et al., 2004, Groppe et al., 2013], which provides the number of clusters with the greatest robustness to trial-related variation in activity. By finding the most stable clusters across trials, we hope to selectively enhance differences related to initial relative to repeat presentation during a picture naming task, in effect deemphasizing trial-related variability.

6.3 Methods

6.3.1 Task Participants

Six subjects were implanted with subdural ECoG electrodes in the left hemisphere (Figure 6.1) for seizure focus and eloquent cortex mapping prior to epilepsy resection surgery. Electrode implantation location was determined solely based on clinical need. Data from this study were recorded from 94 ECoG macroelectrodes from two 4x8 grids and seven strips consisting of four or six electrodes each (0.23 cm diameter, 1 cm center-to-center, company, location). Data were also recorded from 32 ECoG microelectrodes (75 micron diameter, 900 micron center-to-center, PMT Corp., Chanhassen, MN) from two 4x4 grids placed between four adjacent macroelectrodes. Electrode locations were confirmed by volumetric co-registration of the subjects pre-implantation MRI with his post-surgical CT using the BioImage Suite [Duncan et al., 2004]. The subject gave informed consent to participate in this study, which was done in accordance with a protocol approved by the Johns Hopkins Institutional Review Board.

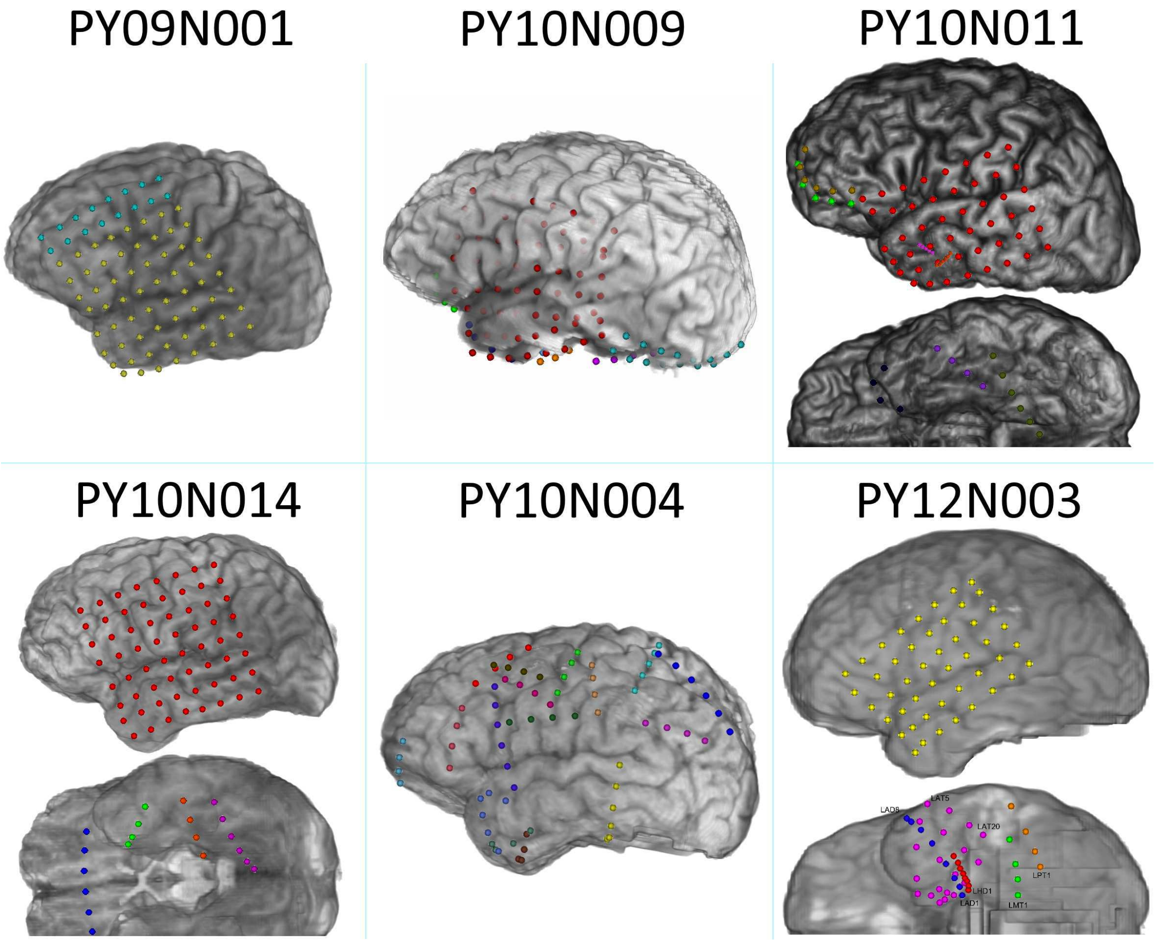

Figure 6.1: ECoG array recording sites for the six subjects participating in the naming priming experiment.

6.3.2 Experimental Design

The subjects reclined comfortably in his hospital bed, while being presented with visual stimuli. The subjects were required to respond verbally with the name of the presented object. The activation of a microphone channel was used to determine response time. Each initial trial consisted of a unique object being presented, with the same object being presented a second time during repeat trials.

6.3.3 Signal Acquisition and Preprocessing

ECoG data were recorded with a 128-channel Neuroport system (Blackrock Microsystems; Salt Lake City, UT) at 1 kHz. Data was initially recorded at 30 kHz with a third-order Butterworth analog bandpass filter with cutoffs of 0.3 Hz and 7.5 kHz, then downsampled to 1 kHz. Noisy channels were visually identified and excluded from subsequent analysis. A common average reference was used to remove noise common to all channels, then data were digitally bandpass filtered from 70-120 Hz and downsampled to 500 Hz.

6.3.4 Clustering

All subsequent analysis was performed using Matlab 2015b (Mathworks, Natick, MA). Two clustering techniques were used. K-means was used in determining the number of inherent clusters, separately for initial and repeat presentations. The cluster number

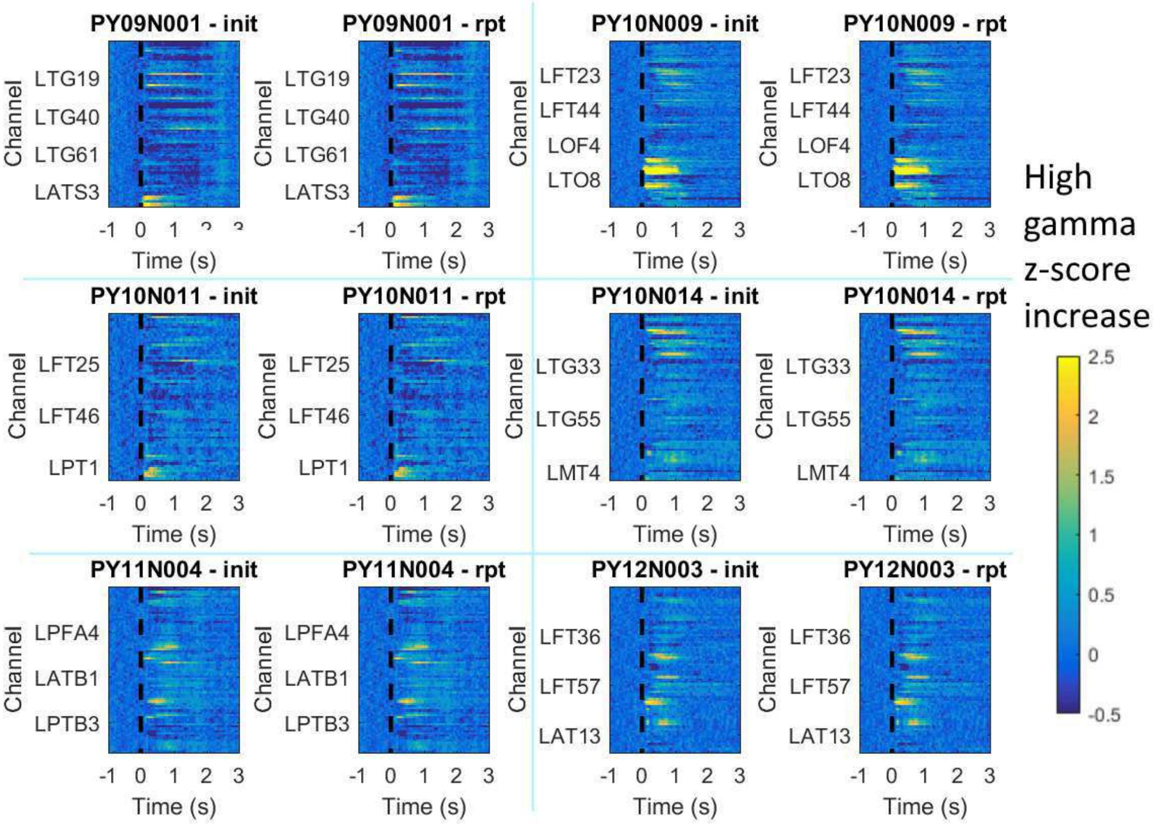

Figure 6.2: High gamma power for each subject's trial averaged spectrogram over initial (init) and repeat (rpt) presentation of each image. Each channel is shown along the vertical axis of the subplots, and is z-scored to the total baseline distribution (-1 to 0 seconds for each trial). Z-score values for individual pixels represent a cue-aligned trial-averaged time window for a single electrode, with the color value corresponding to the z-score on the colorbar.

found for each subject and task-condition was then used in both k-means clustering, and hidden Markov modeling (as the number of states). The high-gamma power amplitude was used as the features for clustering analysis with both the k-means and hidden Markov model approaches.

6.3.4.1 K-means clustering

K-means is a technique to cluster data based on minimizing the distance from each cluster to its center of mass, given a number of clusters k. Because K-means is an NP-hard problem [Drineas et al., 2004], iterative techniques are used to locate the centroid of each cluster [Jain et al., 1999]. Specifically, initial guesses are made for cluster centroids. In this work this is achieved through the use of k-means++ [Arthur and Vassilvitskii, 2007], to help prevent getting stuck in local minima. The centroid guesses are then improved iteratively by assigning membership based on which centroid is closest to each feature, then determining the new center of mass of each cluster based on its membership, and assigning that new value as the centroid. This step is repeated until the centroid no longer moves with successive iterations, within some range of acceptable error. To measure the distance between each centroid and each feature in this process, the square Euclidean distance was used. Correlation distance was also used, but the results were consistent with the square euclidean results, and so were not shown. The entire process was repeated ten times for each condition, and the minimum sum of distances between all cluster members and their centroids was used to find the best clustering.

The centroids were found across all time windows on a continuous time window basis, after removing inter-trial intervals (except for one second of baseline for each trial). Each time window was classified as the cluster with the closest centroid in the high gamma feature space.

To determine the appropriate number of clusters for each subject and task condition, a stability-based clustering validation method was used [Lange et al., 2004, Groppe et al., 2013]. The implementation of the technique is summarized here:

1. The high gamma power for all channels over the continuous trial-centered data was separated into two equal size partitions of time-points (labeled A and B), selected at random.

2. K-means clustering was performed separately for both subsets of time-windows to determine the label of each data point.

3. Step 2 was repeated 10 times, and the centroids and corresponding cluster labels with the minimum spread of data points were kept as that subset's best labels.

4. Cluster centroids from group A were used to reclassify group B, with each datapoint being relabeled as the centroid in A it was closest to.

5. The dissimilarity of the labels for group B from the two conditions: actual group B labels, and group A centroids used to reclassify group B, was measured.

6. Steps 1-5 were repeated 50 times to prevent bias in the selection of group A and

B members from influencing the final results.

7. The process was repeated for k ranging from 2 to 8.
8. The value for k with the corresponding median lowest dissimilarity score was taken as the level of inherent structure for that dataset.

There are many configurable aspects of the stability clustering technique [Von Luxburg, 2010]. Specifically, the data can be partitioned in many different ways, and the partitions can be compared using different measures. In this work, the data was split into two subsets, similar to [Levine and Domany, 2001]. The labels can be compared directly between partitions [Fridlyand and Dudoit, 2001]. To achieve this, the centroids from group A were used to reclassify the members of group B, in this work. Alternatively, the labels of A and B could have been compared directly, but that would require the added assumption that all of the time-windows in both groups come from the same distribution, which may not be the case with randomly sampled heteroscedastic ECoG high gamma power signals [Chang et al., 2015].

Normalized mutual information (NMI) was used to measure similarity between labeled data points [Danon et al., 2005]. The dissimilarity, taken as $1 - NMI$, was minimized as a function of k in determining the optimal number of clusters, as NMI is expressed in the following equation:

$$NMI(A,B) = \frac{-2\sum_{i=1}^{C_A}\sum_{j=1}^{C_B} N_{ij}\log\left(\frac{N_{ij}N}{N_iN_j}\right)}{\sum_{i=1}^{C_A} N_i\log\left(\frac{N_i}{N}\right) + N_j\log\left(\frac{N_j}{N}\right)}, \tag{6.1}$$

where $NMI(A,B)$ is the normalized mutual information between labels A and B, and C_A and C_B are the number of unique labels for A and B respectively, and N_{ij} is the number of data points in A condition's i-th group that appears in B condition's j-th group. NMI is able to select the cluster labels that are the most consistent across sets, despite the value of those labels being variable.

6.3.4.2 Hidden Markov Model

Hidden Markov models (HMM) are a tool for modeling generative sequences that are based on an underlying process generating the observable data [Baum et al., 1970, Blunsom, 2004]. In the case of our experiment, the cognitive execution of the various phases of the complex task are believed to be the underlying process, identified as the hidden states, and the ECoG recordings are the observed data.

To ensure consistency between the K-means and HMM techniques, we used the supplied best fit number of clusters from stability clustering as the number of hidden states in the HMM.

HMM has a state-dependent parameter which determines the likelihood of transitioning from one state to another. By setting this parameter to be very low for transitions, the HMM would better follow the task-progression, without the noise inherent in the k-means approach. If the parameter is set too low between two states, however, there may be a delay in detecting the state transition, or entire states may never be activated. We used expectation-maximization (EM) to optimize this transition matrix [Rabiner, 1989, Gold et al., 2011].

6.4 Results

6.4.1 Cluster number determination

To determine the appropriate number of clusters for each subject and task condition, the stability criteria was compared for a varying number of clusters from one to eight using k-means (Figure 6.3), with square euclidean distance. The centroids were then found that yield the lowest sum of square errors using the corresponding number of clusters. The value of disagreement for each subject and each presentation, taken as $1 - NMI$, is shown in the box plots.

Subjects PY09N001, PY10N011, and PY12N003 had differing numbers of optimal clusters across task conditions. After considering the properties of these additional clusters, however, it was determined that they were spurious activity specific to one to three trials, and not indicative of different task-related states. For subsequent analysis, the minimum number of stable clusters across conditions was used.

While subjects PY09N001 and PY10N009 had three optimal clusters, the remaining four subjects all had two.

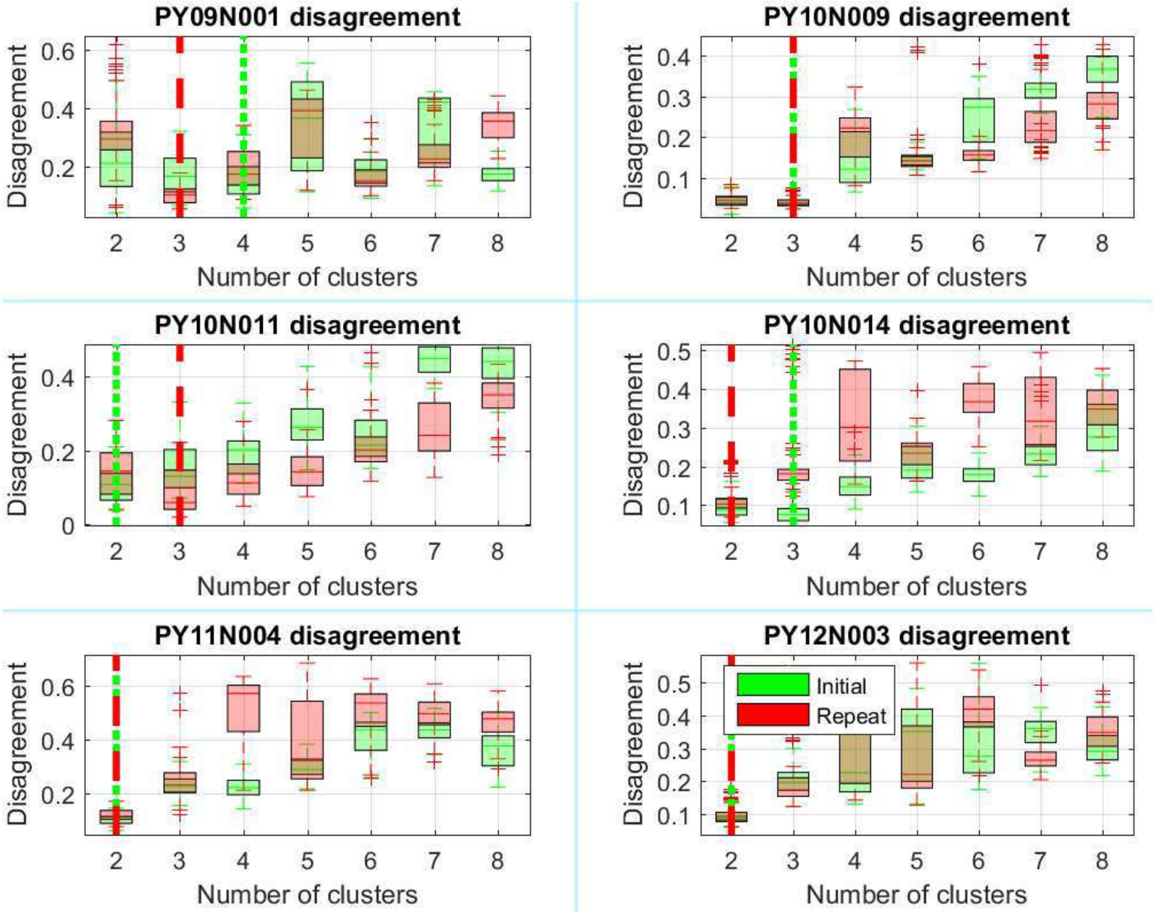

Figure 6.3: Box plots of the number of high gamma power clusters using stability criteria, indicating the normalized mutual information. Green distributions represent initial presentations, while red distributions represent repeats. The colored boxes indicate the 25th and 75th percentiles. Dark bands represent median values. Separate plots indicate unique subjects. Vertical lines indicate the number of clusters for which the disagreement was minimized. The green vertical lines corresponds to the first presentation of a stimulus, while the red lines correspond to the second presentation.

6.4.2 High gamma based single trial k-means clustering

6.4.2.1 Single trial membership

K-means clustering for the six subjects based on the high gamma power was computed using the stability method's suggested number of clusters (Figure 6.4). Assigned membership of a (trial x time-window) pair is indicated by color in the plots. Each pixel was fit to the cluster with the centroid of the smallest Euclidean distance.

It can be seen that pre-cue the electrodes had a nearly-uniform distribution of cluster membership for all subjects except PY10N011, with varying amounts of consistency. Subject PY10N011's clustering does not appear to have any discernible pattern.

For subjects PY09N001 and PY10N009, it can be seen that, after cue there were two distinct phases of cluster membership across trials. For subject PY09N001, the second phase of membership begins shortly after cue and is sustained for the duration of the trial for the majority of trials, but not all. Subject PY10N009, however, had the second cluster occur in almost all trials, and lasted for approximately one second with some variability.

For subject PY09N001, the third cluster occurred approximately one second after response initiation, but only occurred in roughly 1/4th of all trials. This suggests that this cluster was indicative of task completion, prior to the subject returning to

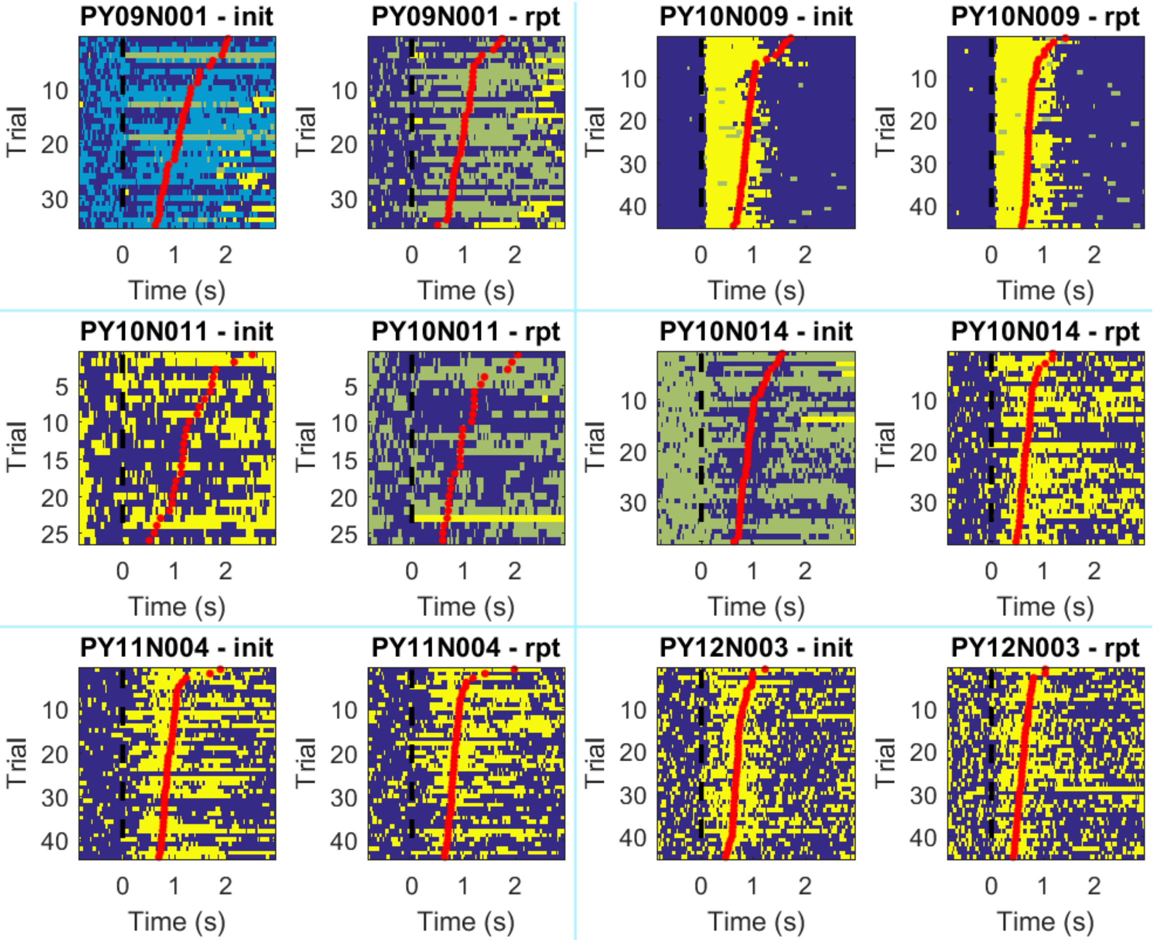

Figure 6.4: Comparison of cluster membership between subjects for high gamma power based clustering. The time on the horizontal axis is relative to the cue timing, with 0 s being the cue presentation. Each row representes a separate trial, sorted by the time between cue presentation and initiation of response. Unique clusters are delineated by different colors. The black horizontal line indicates cue timing and red dots correspond to each trial's response time.

baseline activity, when present.

For subject PY10N009, the third cluster occurred most often immediately after response initiation, and lasted for the remaining duration of the trial. This suggests that this cluster was indicative of response execution. This third cluster was present for approximately 1/3rd of all trials.

6.4.2.2 Frequency of membership

There is inherent variability in how each time window is clustered over trials. To account for this, the frequency of each time window and trial being classified as a particular cluster was determined (Figure 6.5).

All subjects showed a very consistent baseline cluster in dark blue, which dropped in frequency substantially after cue presentation. This baseline cluster had the lowest frequency for subject PY10N011, who had very poor clustering results overall.

There were also very clear post-cue active clusters that drop below baseline frequency several seconds after cue presentation across all subjects.

For subjects PY09N001 and PY10N009, who both had three clusters, the third cluster only ever appears in 40% of trials, never overcoming the second cluster's count in time-windows where it was present.

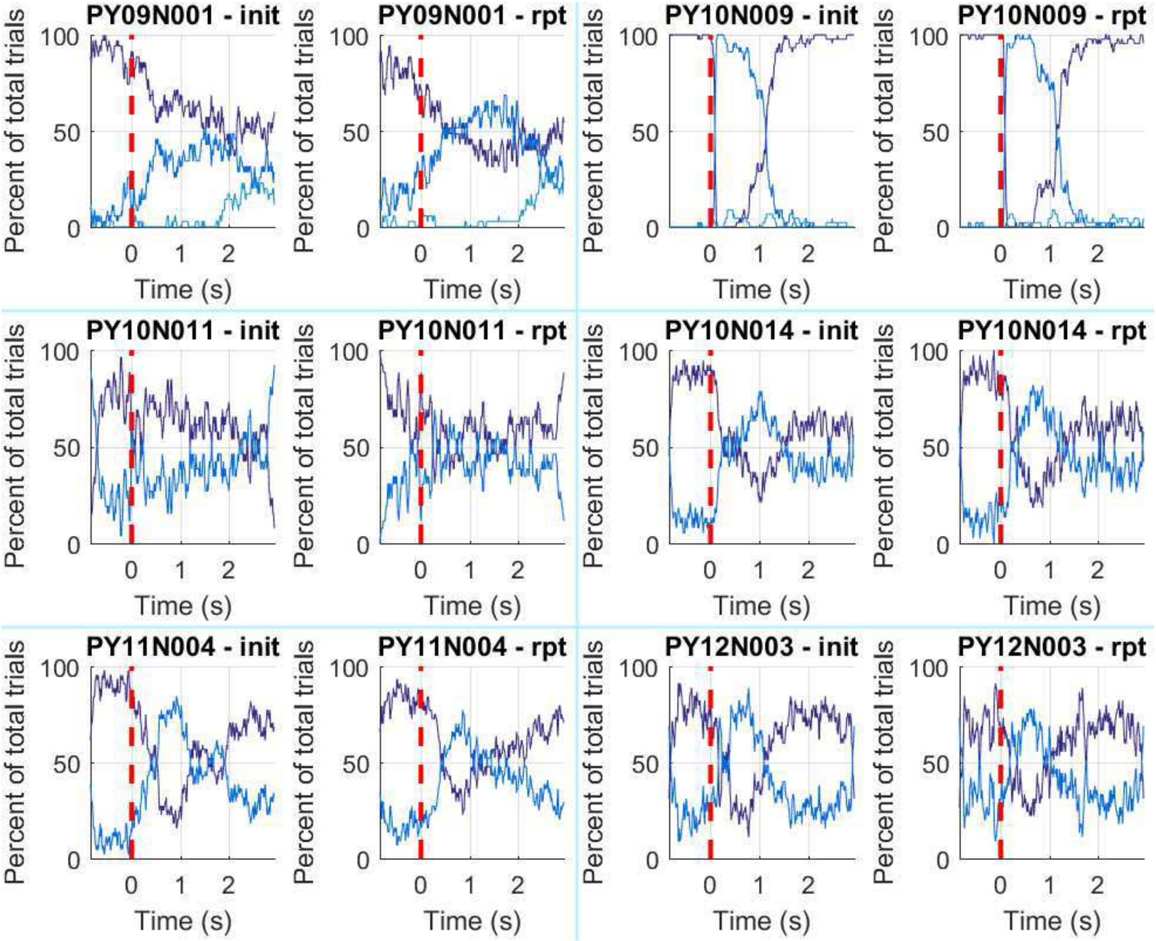

Figure 6.5: Comparison of frequency of cluster membership across all trials in each time window between subjects for gamma power based clustering. The time on the horizontal axis is relative to the event timing, with 0 being cue presentation. Each colored line represents a different cluster.

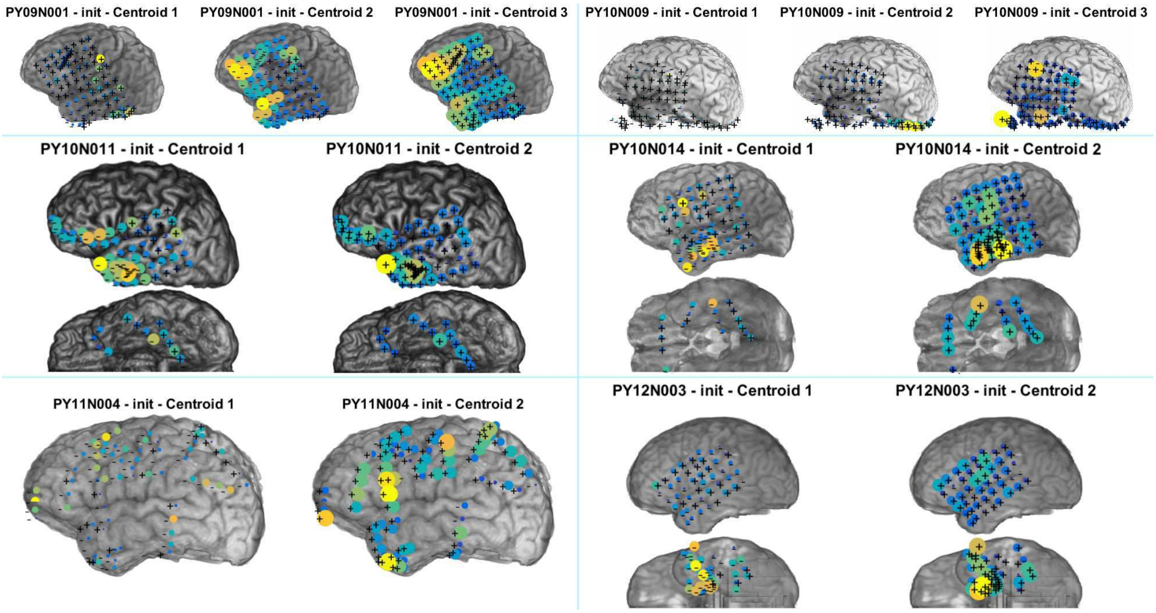

Figure 6.6: Comparison of the cluster centroids for each subject from k-means clustering. The contribution of each electrode to each subject's centroids are shown for each cluster. Size and color of markers indicate the amplitude of that particular electrode to the centroid's corresponding component. Subjects PY09N001 and PY10N011 had three clusters, while the remaining subjects had two. The (+/-) signs indicate whether the location of that component is along the positive or negative axis, respectively.

6.4.3 Anatomical comparison of cluster centroids

The centroids of each cluster, representing the average high gamma power for each individual electrode within its membership is shown (Figure 6.6). These plots contain information about which underlying regions of cortex are active when each time window was classified as a particular cluster member.

All subjects have a cluster with lower activation across the brain. Subjects PY09N001 and PY10N011 have two more active clusters, while the rest have one more active one. Subject PY10N011's more active clusters had very strong contributions by basal electrodes. This was most likely representative of visual processing, and indicates a large increase in basal high gamma power corresponding to classification as a member of one of those clusters.

6.4.4 Initial vs. repeat presentation: k-means centroid comparison

Clustering was performed independently for initial and repeat picture presentation. The distance between those two sets of centroids is shown (Figure 6.7). Because the centroid labels are arbitrary, the distance between all permutations of cluster centroid pairs was determined, and the minimum value was taken as the correct distance. Distances were normalized by the average variability in each channel's activation over all time-windows.

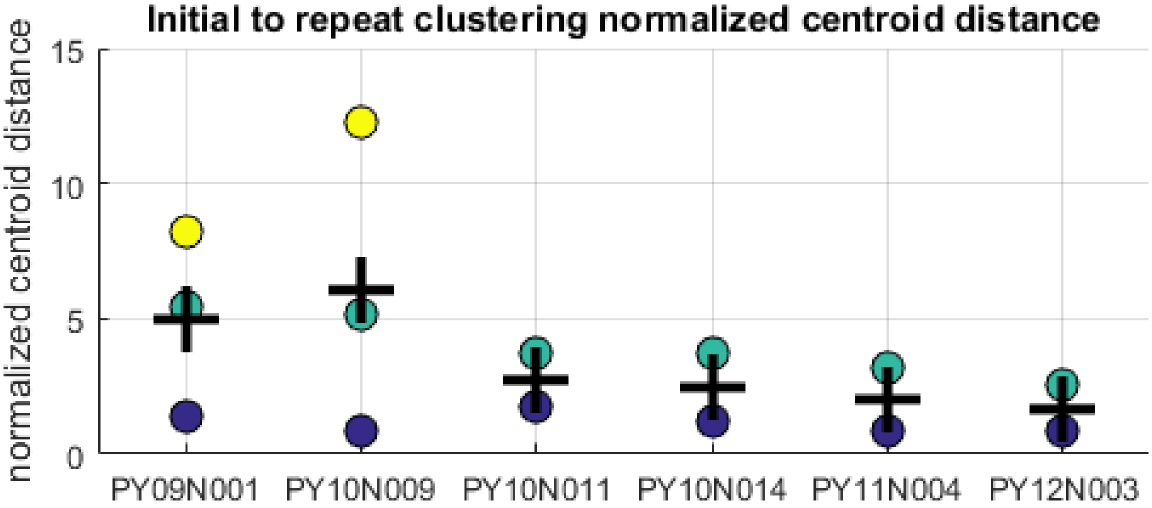

Figure 6.7: Comparison of the mean L_2 norm distance between cluster centroids for each subject from k-means clustering between initial and repeat trials. Distances were corrected by the individual channels' standard deviations across all time-windows, to separate centroid variability from general electrode amplitude variation. The minimum over all possible distances of cluster centroids was determined, due to the labels not being consistent across clusterings. Circles indicate the distance between particular centroids, corresponding to the coloring used in Figure 6.4. Crosses indicate the mean distance across all centroids for each subject.

Subjects PY09N001 and PY10N009 both showed similar centroid average distances to the other subjects, except for their additional third cluster. This third cluster, which only appeared in a minority of the trials, was much less consistent in electrode amplitude across task conditions. This suggests that the most stable state for both conditions supplies consistent centroid locations across clustering for similar data, with the exception of the spurious activity clusters which demonstrated more variability in centroid coordinates.

For all subjects the baseline centroids were nearer across conditions than the response clusters. This is indicative of the baseline period not containing task-specific activity, since the subject was not prepared before cue presentation.

Overall these distances were extremely small, and were consistent across subjects. This consistency is a result of correcting for channel variability, by reducing the impact of noisier channels on the distance between task conditions, the cross-condition distances appeared consistent between subjects. This suggests that the clustering reveals task-phase specific differences which were consistent across trials, whether the picture was presented initially or repeated.

6.4.5 Relative change of cluster centroids between task conditions

The relative change in centroid components is shown for the two subjects with three distinct clusters (Figure 6.8). Both subjects showed highly localized component dif-

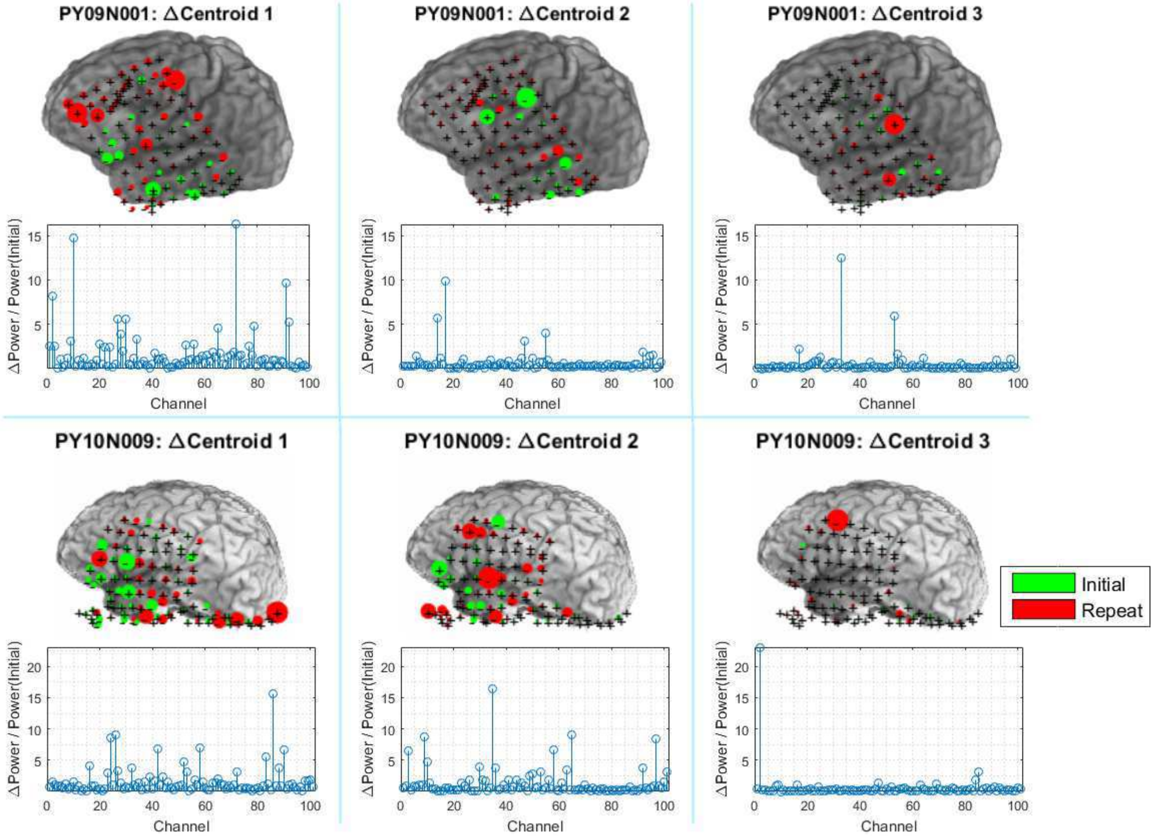

Figure 6.8: Relative change in cluster centroids corresponding to the same state across initial and repeat trials. (Top) Subject PY09N001 and (bottom) PY10N009 are shown, since they had three separate task-related clusters. The top half of both plots show the individual electrode activations within each cluster centroid. (+/-) indicates the sign of each electrode's activation. The bottom half of both plots show the magnitude of each channel's relative change between initial and repeats.

ferences in the third, more spurious, state.

The differences in the first centroid, which appeared most frequently during the baseline period, were on the same scale as the other task-based components. Taken in conjunction with Figure 6.7 the change in activation patterns is actually much less substantial when the total channel variability is taken into account.

6.4.6 HMM based single trial clustering

Each subject was clustered using an HMM with the number of hidden states corresponding to the number of clusters from the respective k-means solution, as shown in Figure 6.9. Each subject's results were extremely similar to the k-means solution in terms of cluster activations across trials and time.

Due to the decreased likelihood of transitioning from one state to another over k-means, however, these results were more stable over time. This stability of cluster membership is clearly seen in Figure 6.10, where most subjects had almost 100% of their baseline clusters in a single cluster.

Both subjects PY09N001 and PY10N009 third cluster was present in more trials with the HMM classifier. This suggests that HMM is better at separating out the specific activation pattern present in that cluster.

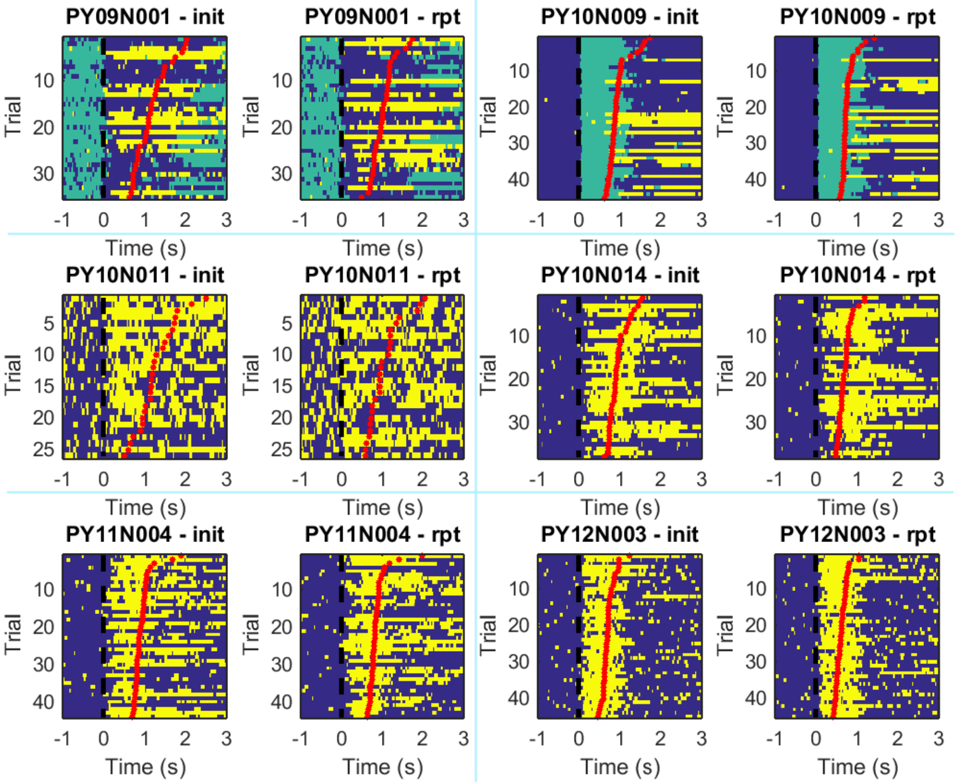

Figure 6.9: Comparison of cluster membership between subjects for the hidden Markov model. The time on the horizontal axis is relative to the cue timing, with 0 s being the cue presentation. Each row representes a separate trial, sorted by the time between cue presentation and initiation of response. The black horizontal line indicates cue timing and red dots correspond to each trial's response time. Unique clusters are delineated by different colors.

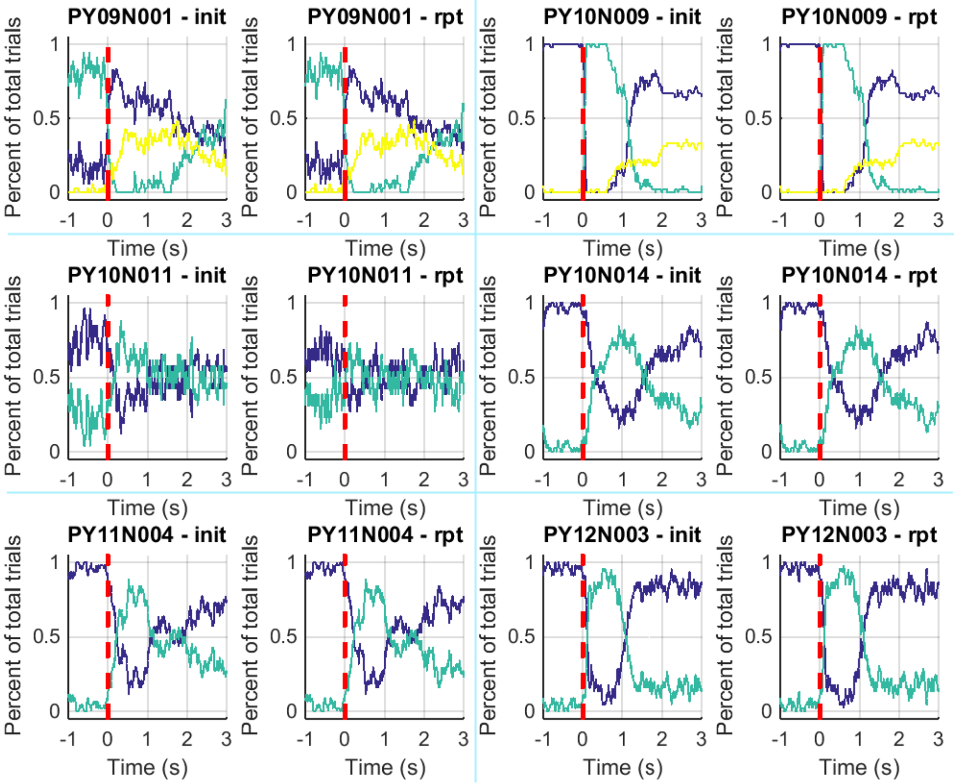

Figure 6.10: Comparison of frequency of cluster membership across all trials in each time window between subjects for the hidden Markov model. The time on the horizontal axis is relative to the event timing, with 0 being cue presentation. Each colored line represents a different cluster membership frequency.

6.5 Discussion

This work involves the use of single trial high gamma power to find clusters across individual time windows of activation, with the stability measure used to determine the number of clusters. Additionally, the most stable number of clusters for k-means was used as the number of hidden states in an HMM, allowing for smoother inter-cluster transitions. These clusters showed trial-timing dependent activation. Across task conditions, selective differences were found in centroid locations, suggesting differing underlying brain activation between initial and repeat trials localized to specific cortical regions.

6.5.1 Single trial clustering

Single trial clustering demonstrated stability with the correct number of clusters, and provided task related activation in a consistent manner across trials. With the exception of subject PY09N001, all subjects showed an increasing trend in stability disagreement with increasing cluster numbers (Figure 6.3). This suggests that these stable states were the most representative of distinct task-related cognitive processing. Subject PY09N001's consistently low disagreement across cluster numbers may be indicative of differing levels of processing occurring simultaneously, causing the most stable state not to result in the only possible clustering.

For most subjects, two clusters were seen as the optimal configuration, between task conditions 6.3. Only two of the 6 subjects had three representative clusters. While three of the subjects had a different number of stable clusters across task conditions, when the time-window classification was examined, it was clear that spurious activity across a very limited number of trials was separated into its own cluster 6.4. To account for this, the number of clusters was constrained to a consistent number across both conditions. This suggests that those few trials may have had some extrinsic factor influencing the subject's activation, which was not accounted for by task conditions.

This suggests that while those two subjects had discrete brain activation patterns corresponding to the evolution of the task, the other four subjects may have had less distinct task-related brain activation, and only showed substantial modulation between the baseline period and the task performance. Alternatively, given the limitations of the recording modality, it's possible a region of cortex corresponding to substantial differential activation was only covered in the two subjects who showed the three unique clusters. The differences of time courses of cluster activation, in addition to the cluster count, support this claim. This further lends support to the suggestion that there are distinct brain-networks that are engaged for different phases of task performance in a consistent manner.

During complex tasks recorded with ECoG, coverage can impact which types of activity can be detected in the signals [Miller et al., 2007]. The first two clusters for all subjects are robust across subjects, in terms of timing of predominant activation. The presence of these clusters was most likely not an artifact of the grid-coverage individual subjects received, since the analysis was consistent across six unique subjects. This supports the claim that these two clusters were fairly robust to differences in coverage, and are indicative of global brain activation phenomenon corresponding to task engagement.

The difference in cluster numbers determined for subjects PY09N001 and PY10N009 suggests grid-coverage may have some impact on clustering, however, since they have very specialized clusters active late in the trial.

6.5.2 Spatial distribution of cluster centroids

While the magnitude of individual component contributions varied between centroids for each subject (Figure 6.6), there was no clear spatial separation of cluster localization, for the most part. With the exception of PY10N011, all subjects showed consistently lower electrode activations across the grids for what is representative of the baseline phase. The second and third centroids, when present, show increased activation, in either the positive or negative direction, depending on the electrode. This is to be expected, however, due to the Z-scoring used to separate task-related modulation from channel dependent noise.

All subjects show a focus of activation in the more rostral electrodes along the grid, for the non-baseline clusters, with the exception of PY10N011 who shows that increased modulation in the baseline cluster, as well. Subjects with basal electrodes, including PY10N011, PY10N014 and PY12N003 also show increased activation in those for response-period centroids. This task required semantic processing and auditory response, suggesting both centroids two and three, when present, represented task-specific processing.

Subject PY10N009 had very strong and sparsely distributed contributions to the third, more spurious centroid. The timing of this centroid is very constrained, and inconsistent across trials, indicative of some task-independent short-lasting process. The focus of this activation in certain electrodes suggests it may have been some high order processing requiring the coordination of multiple cortical regions.

6.5.3 Task condition specific clustering differences

The comparison of cluster centroids for corresponding task phases for two subjects showed sparse and widely distributed changes in activation (Figure 6.8). While Subject PY09N001 showed the largest decreases in activation with repeat presentation, Subject PY10N009 showed greater increases in activation, but also some electrodes with decreases, in a non-spatially specific manner. This may have indicated changes in neural processing occurring with the repeat presentation of a stimulus, as suggested in [Hayman and Tulving, 1989, Schacter et al., 1991].

For both subjects, the third cluster showed greater increases in activation with repeat stimulus confined to one to two electrodes. This third cluster was only present in a small portion of trials, suggesting the activity underlying this response, when present, was locally modulated across task conditions.

The third cluster showed different properties for each subject, however. While Subject PY09N001 showed late response time-locking, Subject PY10N009 showed sparse activation with inconsistent trial-locked timing. This suggests that these clusters represented different cognitive processes, so they were not directly comparable.

6.5.4 Reduction of dimensionality of ECoG recordings

The cluster centroids for each subject were in the high gamma power space, with dimensionality equal to the number of electrodes. Since all electrodes without noticeable noise were used for this analysis, these clusters existed in very high-dimensional space, of subject-dependent dimensionality.

Dimensionality reduction techniques, such as principal component analysis (PCA) with thresholding of the components based on their contribution to the variance of the data should be useful for selecting task related activity [Jolliffe, 2005]. This technique has been successfully applied to channel selection for ECoG separation of task related activity [Naeem et al., 2009].

It should be expected that computing the clustering on the lower-dimensional representation of the data would improve the results, possibly increasing the number of clusters, and the consistency of cluster membership across trials. PCA was attempted, however, with 8 components kept. This would both decrease the dimensionality of the features substantially, and allow for all subjects to have a consistent number of features. The results are not shown, since they showed no improvement in any noticeable quality. All subjects had the same number of stable clusters as in the electrode-space clustering, but a general decrease in clustering disagreement was seen for low numbers of clusters.

When PCA was attempted, the first component generally explained 20-40% of the variance, with subsequent components only explaining 1-4% each, which is very unusual. This is most likely due to the very high dimensional space of the raw ECoG recordings, as opposed to preselected task-specific electrodes (varying between 60 and 90 electrodes per subject).

6.5.5 Consistency across k-means and HMM clustering

The high gamma based clustering results, as summarized in Figure 6.5 for k-means, and Figure 6.10 for HMM, show surprising consistency. This suggests that both methods emphasized similar criteria when determining the constituent time-window activation patterns for the electrodes.

The HMM method allows for the tuning of a transition probability matrix, which in this work was done using EM, but other methods could have been applied [Ford and Moore, 1998]. By further emphasizing stationarity of cluster membership, it is possible to decrease the noise in cluster determination over time, even for single trial data.

These results already show improved consistency over k-means classification, however. All subjects show a higher frequency baseline period, which is further subdued during task performance, suggesting the HMM method has better consistency in detecting the actual task-phase.

6.6 Conclusions

This study examined the time-evolution and spatial distribution of clusters found across neural data obtained from ECoG arrays during a picture naming task. The method successfully detects two or more clusters in six subjects performing a picture naming task. One of the clusters overlays baseline period activation for all six subjects, while the remaining cluster shows a clear task-related time-course modulation. For the two unique subjects, the third cluster showed post-response activation, with timing dependent on response initiation.

The methodology was able to separate both task-phase specific variation in brain activation, and show how this underlying activation was modulated with task conditions, over initial and repeat presentation of a stimulus. Using the stability clustering method, it is possible to detect subtle changes in brain activation pattern modulation with the conditions of task performance.

Chapter 7

Identifying neuron communities during a reach and grasp task using an unsupervised clustering analysis

7.1 Abstract

Recent advances in brain-machine interfaces (BMIs) have allowed for high density recordings using microelectrode arrays. However, these large datasets present a challenge in how to practically identify features of interest and discard non-task-related neurons. Thus, we apply a previously reported unsupervised clustering analysis to neural data acquired from a non-human primate as it performed a center-out reach-and-grasp task. Although neurons were recorded from multiple arrays across motor

and premotor areas, neurons were found to cluster into only two groups which differ by their mean firing rate. No spatial distribution of neurons was evident in different groups, either across arrays or at different depths. Using a Kalman filter to decode arm, hand, and finger kinematics, we find that using neurons from only one of the groups resulted in higher decoding accuracy (r=0.73) than using randomly selected neurons ($r = 0.68$). This suggests that the proposed method can be used to prune the input space and identify an optimal population of neurons for BMI tasks.

7.2 Introduction

Brain-machine interfaces (BMIs) have been developed to successfully decode upper arm movements of monkeys in both open-loop [Taylor et al., 2002] and with real-time feedback [Velliste et al., 2008]. Traditionally, BMI researchers have recorded from single cortical sites and been limited to decoding from individual neurons that are found to be tuned to the movement or otherwise task-related [Schwartz et al., 2001]. However, recent advances in neural recording now allow for single session datasets with multiple signals obtained at high sampling rates using microelectrode arrays. This increased data has led to the decoding of more complex, multiple-DoF movements [Vargas-Irwin et al., 2010].

Even in cases where multiple neurons are decoded, only individual contributions to the decoding accuracy are considered and not how neurons function as a group. Neuronal interactions are generally assumed to be stationary, and their groupings constant. In order to extend the capabilities of BMIs, the behavior of neurons as dynamically evolving communities must be considered. For example, although a particular group of neurons may show the highest decoding accuracy during one component of a task, there is no reason to expect the same group will decode a different component similarly well. Furthermore, not all single units from multichannel recordings are task-related and thus potentially contribute only noise to the decoding filter. Presumably, neurons that are not relevant to the task would exhibit different firing rate profiles and could thus be identified and pruned from the input space ahead of time.

Finding community structure in neuronal data is complicated by several factors. First, the true number of neuronal groups is not known - and thus methods that specify the number of groups a priori artificially bias the observed structure. Second, most grouping techniques are semi-supervised and thus require the specification of additional initial parameters [Slonim et al., 2005]. In order to overcome these issues, we employ a novel clustering technique described by Humphries [Humphries, 2011], which identifies neuronal communities based on similarities between spike trains. This technique is also robust in that it self-determines the number of groups and clusters neurons accordingly.

We apply this clustering technique to spiking data collected from primates as they perform a center-out reach-and-grasp task. This paper has three goals: (1) we will group across all trials for each neuron to determine whether neurons have a stereotypical response for identical motor movements, (2) we will then group across all neurons and investigate how neurons are grouped spatially across arrays, and whether this grouping is different for each movement type, and (3) we will see if the resultant grouping can be used for feature selection in decoding arm, hand, and finger kinematics. Thus, this work aims to provide a better understanding of neuronal behavior across multiple cortical regions during a BMI motor task.

7.3 Methods

7.3.1 Experimental Setup

A male rhesus monkey (M mulatta) was visually cued to reach towards and grasp four different objects at different spatial locations (Figure 7.1, middle). After grasping, the monkey was required to rotate the sphere 45, pull the perpendicularly mounted cylinder (mallet), depress the pushbutton, or pull the coaxial cylinder. Single-unit activity was recorded using a Plexon (Dallas, TX) data acquisition system from five floating microelectrode arrays (FMA) in the primary motor cortex (M1), one each in dorsal (PMd) and ventral (PMv) premotor cortex, and one in the primary somatosensory cortex (S1). Each FMA consisted of 16 electrodes and up to four single-units could be discriminated per electrode. Upper-limb kinematics were simultaneously tracked using a Vicon (Oxford, UK) motion capture system with 30 markers on the forearm, palm, and individual fingers. Joint angles of the hand, wrist, and fingers were calculated using methods described in [Aggarwal et al., 2011].

7.3.2 Clustering Algorithm

Neurons were grouped using the clustering algorithm described in detail by Humphries [Humphries, 2011] and implemented in Matlab 7.4 (MathWorks, Inc., Natick, MA). A summary of the key steps is presented here.

As a pre-processing step, individual spike trains were first binned at different time scales. The similarity between any two spike trains was assessed by computing the Hamming distance, which is defined as the proportion of identical bins in each spike train. In this fashion, a similarity matrix Formula was constructed for all pair-wise comparisons of spike trains,

$$C_{ij} = C_{ji} = 1 - h_{ij} \tag{7.1}$$

where h_{ij} is the Hamming distance between the i-th and j-th spike trains. The diagonal of C was set to zero, so that self-similarity would not influence grouping.

The clustering technique uses network theory to describe the similarity matrix as an undirected network, where each spike train represents a node. The goal is to thus maximize the modularity Q over all possible divisions of the network,

$$Q = Trace(S^T(C - P)S) \tag{7.2}$$

where C is the similarity matrix from before; P is the null-network model that captures the expected number of links within each community, and S is a matrix denoting which group that a node belongs to. In other words, P represents the pair-wise probability of spike trains forming connections with each other and is defined as,

$$P_{ij} = \frac{d_i d_j}{m}, \tag{7.3}$$

where d_i is the total strength of connections from node i, and m is the total strength of all of the connections.

S represents the grouping matrix and is defined as,

$$S_{ij} = \begin{cases} 1, & \text{if } nodeiisingroupj \\ 0, & \text{otherwise} \end{cases} \tag{7.4}$$

Rather than fixing the number of groups a priori, both the number of groups and group memberships of all nodes are determined iteratively. To determine an upper bound on the number of possible groups, we performed singular value decomposition on the modularity matrix $B = C - P$, and retained all N eigenvectors with positive eigenvalues. We then performed K-mean clustering for $K = 2...N + 1$ possible groupings and calculated Q_K for each case.

In order to account for spurious groupings due to patterned firing of individual neurons, the same grouping analysis was performed after randomly shuffling the inter-spike intervals (ISIs) of each spike train to form new spike trains [Humphries, 2011]. While the mean and variance of the firing rates are unaltered, cross-correlations between spike trains are eliminated. The shuffling was repeated 20 times and the maximum modularity score Q_C was used as an upper-bound for the control case. The grouping matrix S that results in the maximum difference $\Delta Q_{\max}$ between the modularity score for the experimental data and the control data is retained.

$$\Delta Q_{\max} = \max_k (Q_K - Q_C) \tag{7.5}$$

In order to determine the optimal number of groups and time scale for the clustering analysis, a golden-section search with parabolic interpolation [Forsythe et al., 1977, Brent, 1973] was used to repeat the clustering with varying bin sizes until it converged to a maximal $\Delta Q_{\max}$, i.e. the maximally effective grouping.

7.3.3 Decoding Hand and Finger Kinematics

For continuous prediction of arm, hand, and finger kinematics, a single Kalman filter was used to model the relationship between neural activity and the 18 joint angles. In the Kalman framework described in detail in [Schieber and Hibbard, 1993], each joint angle is modeled as the system state, X, and the mean spike firing rate during the previous 100 ms is modeled as the observation, Y. At each discrete 20 ms time step Formula, the observed neural activity is modeled as,

$$X(t_k) = H(t_k)Y(t_k) + q(t_k) \tag{7.6}$$

and the state estimate model is defined as,

$$Y(t_{k+1}) = A(t_k)Y(t_k) + w(t_k) \tag{7.7}$$

where H and A are coefficient matrices, and $q(t)$ $N(0, Q)$ and $w(t)$ $N(0, W)$. Neurons with a mean firing rate of less than 1 Hz were removed from the population. Mutually exclusive feature sets were used for training and testing, and results were averaged using fivefold cross-validation.

7.4 Results

7.4.1 Single Neuron Analysis

Figure 7.1 shows the activity of a single neuron recorded from an array in M1, grouped across all trials for each of the four object types (cylinder, pushbutton, mallet, sphere). Individual trials were aligned to the time at which the monkey grasped the instructed object. To facilitate comparison across movement types, a fixed bin size of 100 ms was used for clustering. As can be seen, the neuron exhibited two different firing rate responses (green, red) for each of the movements. This suggests that some extrinsic factor unrelated to differences in the task conditions may affect the modulation of that neuron.

This particular neuron shows a stereotypical increase in firing rate during the period immediately preceding object grasp ($t = 0$), as did others from M1. Visual inspection of the neural response for each group suggests that trials are separated primarily

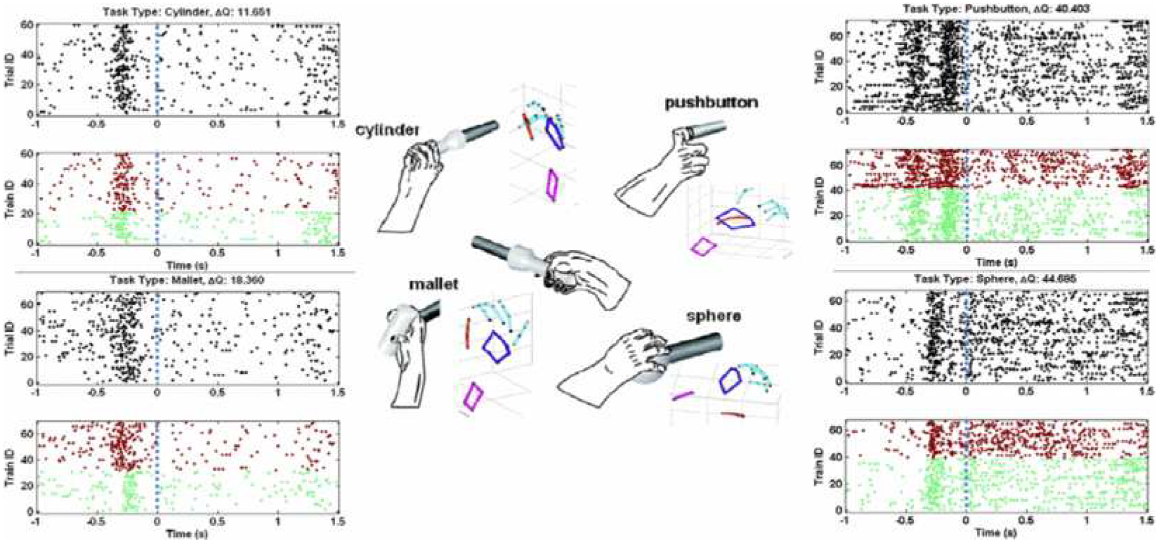

Figure 7.1: Simultaneous neural and kinematic activity was recorded from a non-human primate as it reached towards and grasped four different objects in space (middle). Activity of a single neuron (sig 099a, M1) was grouped across all trials for each of the four object types (clockwise from top left: cylinder, pushbutton, mallet, sphere). The spike trains are ordered by trial number and by group assignment from the clustering analysis Formula. The vertical dashed line at Formula indicates time of object grasp.

based on differences in the firing patterns prior to grasping. Specifically, trials in the green group appear to have a lower firing rate during the reach period than trials in the red group.

7.4.2 Multiple Neurons, Combined Movements

Figure 7.2 shows the grouping across all neurons recorded from the eight FMAs. For each neuron, all trials for the four object types were concatenated to form a single continuous spike train. As can be seen in neurons were grouped into one of two groups: neurons that fire sporadically (green, mean firing rate of 4.2 Hz) and neurons with patterned activity or high firing rate (red, mean firing rate of 16.7 Hz). Grouping across all movement types yielded an optimal bin size of 93 ms and a corresponding ΔQ of 218.4.

To investigate spatial patterns in the neuron groupings the location of each neuron, colored according to its group membership. Neuron locations were determined from the positions of each array and the known length of each electrode. The sphere size for each neuron represents how strongly the neuron belongs to its group, and is inversely proportional to the square of the Euclidian distance between the neuron's location in the eigenspace and the K-means centroid of the group. No clear spatial organization is evident as neurons from both groups are distributed across all arrays and at different cortical depths.

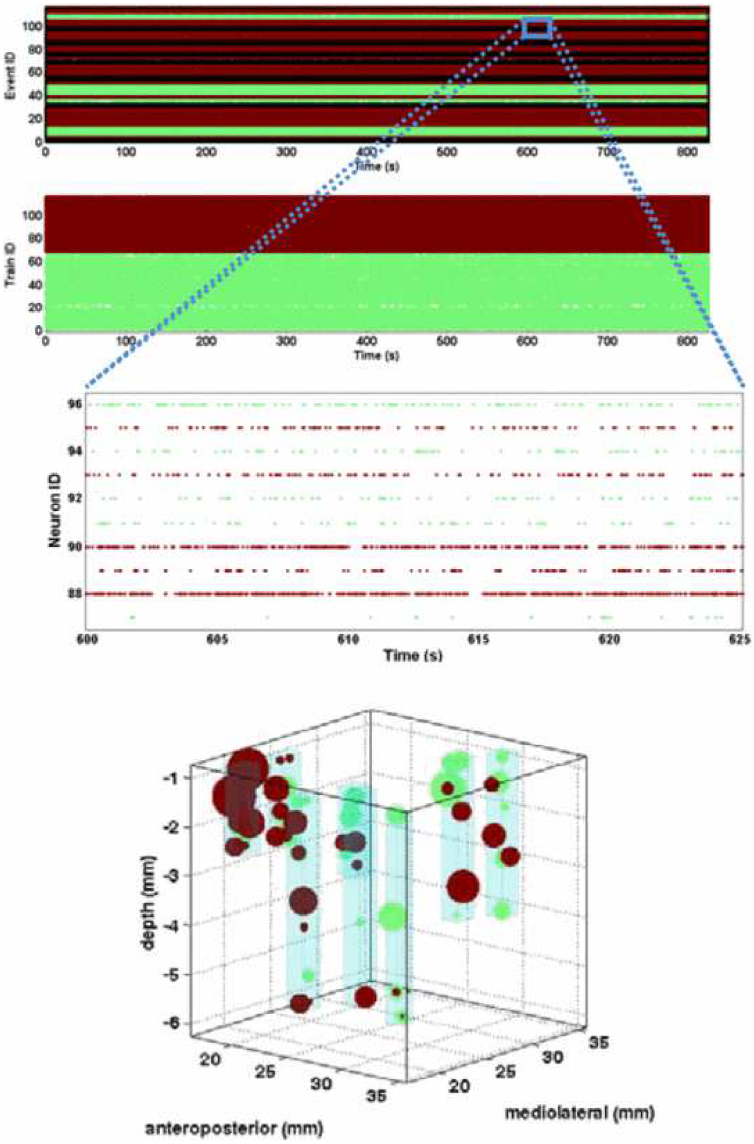

Figure 7.2: A) Grouping of neurons from all seven arrays into one of two groups (green, red), ordered by neuron number in each array (top) and group number (bottom). B) Zooming in on a 25 sec window for sample M1 neurons reveals differences in neuronal response for members of each group, primarily based on firing rate. C) Spatial distribution of neurons across all eight arrays. The size of each sphere represents how strongly the neuron belongs to its group, and color indicates group membership. Light blue cubes indicate the volume occupied by each FMA.

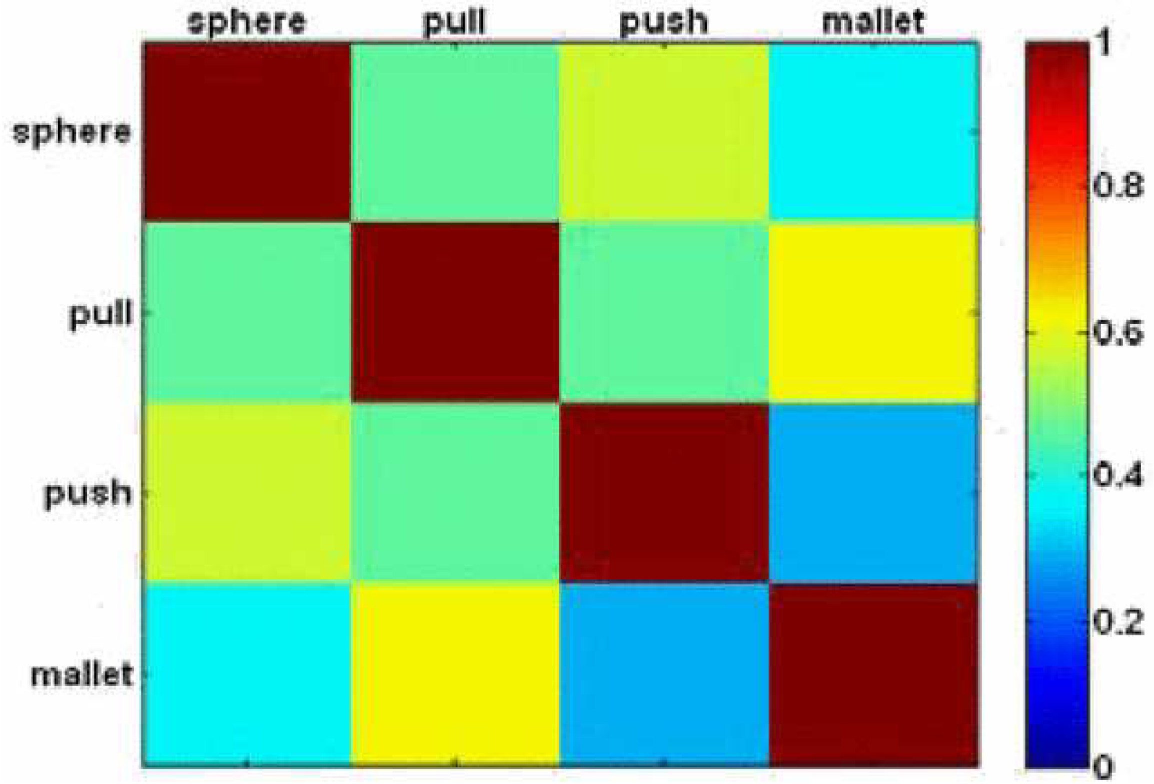

Figure 7.3: Normalized mutual information (MI) between group assignments (i.e. distribution of neurons assigned to group 1 or group 2) for grasping of each of the four different objects.

7.4.3 Comparing Group Membership

To compare how the same population of neurons was assigned to groups for each of the different task conditions separately, we calculated the normalized mutual information (MI) which provides a measure of how similar a group assignment from one set of data is to another set of data through the following equation [Danon et al., 2005]:

$$MI(A,B) = \frac{-2\sum_{i=1}^{C_A}\sum_{j=1}^{C_B} N_{ij}\log\left(\frac{N_{ij}N}{N_i N_j}\right)}{\sum_{i=1}^{C_A} N_i \log\left(\frac{N_i}{N}\right) + N_j \log\left(\frac{N_j}{N}\right)} \tag{7.8}$$

where N is a confusion matrix whose rows are group assignments for the first task condition and columns are group assignments for the second task condition. N_{ij} is the number of nodes (i.e. neurons) in the first task condition's i-th group that appears in the second task condition's j-th group. As seen in Figure 7.3, neurons were assigned to relatively similar groups across all four task conditions, with the smallest MI between the pushbutton and mallet object types.

7.4.4 Decoding Results

Figure 7.4 shows the Pearson correlation coefficients (r) for continuous prediction of arm, hand, and finger kinematics as a function of high firing group 1 neurons (red), low firing group 2 neurons (green), or randomly selected neurons (blue). The correlation values shown are averaged across all 18 joint angles. As can be seen, the average decoding accuracy using group 1 neurons was statistically significantly higher than

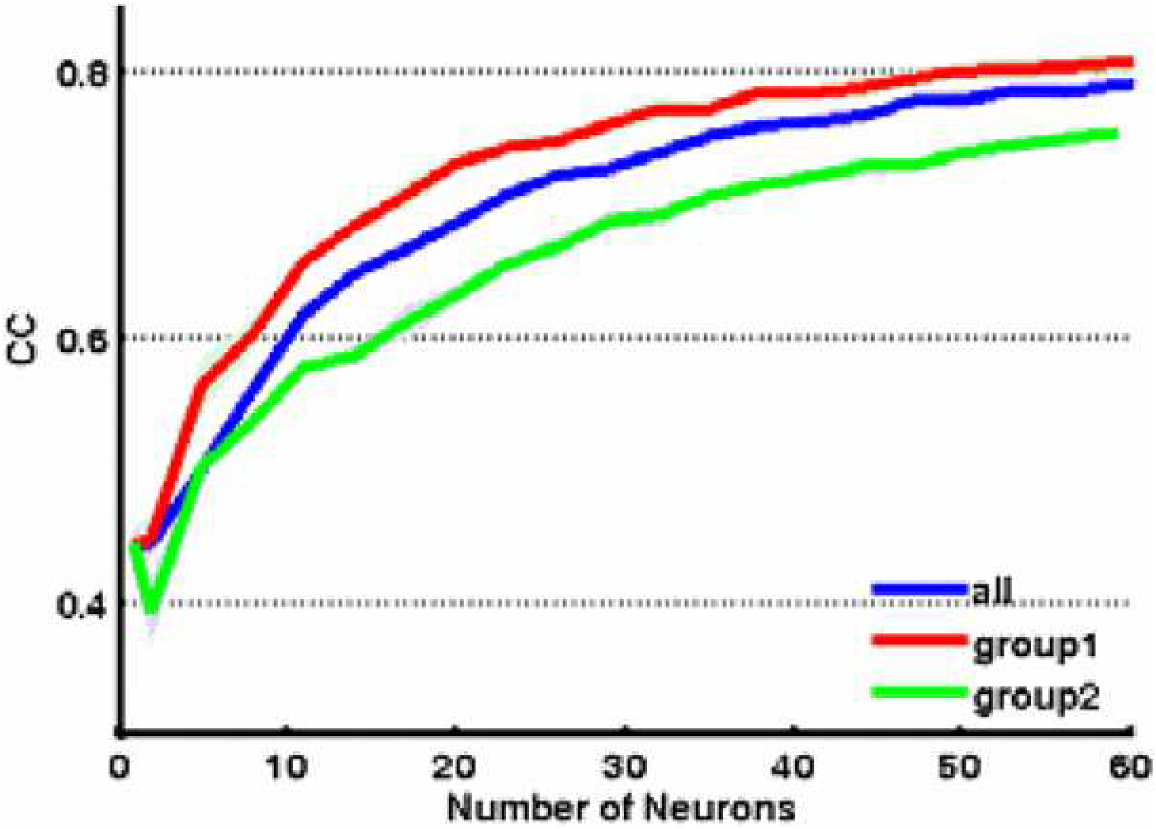

Figure 7.4: Correlation coefficients (r) for prediction of arm, hand, and finger kinematics, as a function of group 1 neurons (red), group 2 neurons (green), or randomly selected neurons (blue).

that using group 2 neurons or randomly selected neurons ($p < 0.05$). This difference was more evident with fewer neurons (for $n = 20$: group 1, $avgr = 0.73$; group 2, $avgr = 0.63$; random, $avgr = 0.68$). Therefore, this clustering method could help prune the input space to use neurons that are optimal for decoding.

7.5 Discussion and Conclusions

It is somewhat surprising to discover that an individual neuron's firing rate response varied over time for a given movement, even though the monkey performed fairly stereotypical movements for each object type. From the grouping analysis, we find that neurons are separated based on how they respond to certain phases of the task, which facilitates comparison of firing properties during a single response type. It is also informative that the optimal grouping resulted in two groups, which suggests that the elicited response may actually be influenced by some extrinsic binary factor independent of the object being grasped, e.g., whether the monkey was gazing at the target object during grasp or elsewhere. Without this grouping analysis, these trial-to-trial variations in neuronal response would be hidden by the more global response archetypes that are distributed over repeated trials.

Grouping across neurons from all arrays, however, no longer distinguishes groups based on event-locked responses, but instead selects for differences in firing rate profiles over a longer timescale. In addition, this grouping analysis reveals that there is no obvious spatial distribution of neurons from different groups, either across arrays or at different depths. This provides more evidence for a complex and heterogeneous organization of the motor cortex, which has been found to lack strict somatotopy at a fine scale [Schieber and Hibbard, 1993].

Lastly, it is important to note that the current clustering technique does not take into account delays between different cortical areas. To account for this, we can compute adjacency matrices for different sets of lags across arrays, and select for the optimal lag that gives the largest ΔQ. This could reveal additional information about network structure and also what delays exist between discrete cortical regions.

Chapter 8

General Discussion

8.1 Summary and Significance of Results

The work presented here has demonstrated that effective connectivity models of neural recordings can be efficiently summarized with network measures. First, we showed that EEG mu-band modulation can effectively restore smooth movement control to spinocerebellar ataxia patients, with near-parity to control subjects' control capabilities. We then used PageRank centrality to determine how the important task-relevant brain regions evolve over time based on connectivity measures in ECoG subjects. Next we demonstrate that clustering using k-means on these ECoG signals can reveal task-relevant functional units in single trial analysis. An unsupervised clustering method found inherent network structure without any a priori assumptions. Finally, we identified functional communities from single unit activity using an eigenspectral clustering technique. These communities were used to improve decoding accuracy of reach and grasp movements. The network methods utilized in this work showed modulation with various aspects of the behavioral task. These results suggest that BCI control could be improved through the appropriate implementation of network measures.

8.1.1 Variation of EEG during BCI control

Mu band (7-12 Hz) power changes over left and right hand area of motor cortex were shown to allow a severe spinocerebellar ataxia (SCA) patient to control a three-state BCI system with nearly the accuracy of a healthy control. This control did not require actual movements to be produced, but instead for the subject to imagine the intended movement, bypassing the diseased motor-output pathway of the ataxia subject.

8.1.1.1 Limitations of three-state EEG BCI

While any improvement in the smoothness and accuracy of control achievable through the use of a BCI is beneficial to the most severe spinocerebellar ataxia (SCA) patients, further improvements in accuracy and degrees-of-freedom would increase the utility of the system. The spatial resolution of EEG is limited, it is unlikely to be able to differentiate between independent dimensions of movement control directly from M1 cortical recordings. Additionally, as has been discussed, high gamma power shows high spatial specificity with modulation to highly specific movements, but this feature is not present in EEG recordings due to the low-pass filter effect of the skull.

To extend analysis to connectivity models, it is necessary to use recordings of higher spatial and temporal resolution. This has led to the use of invasive ECoG recordings to allow for improved signal properties which are amenable to connectivity analysis.

8.1.1.2 ECoG Network Analysis

8.1.1.2.1 Connectivity

The increased recording site density and higher frequency feature content of ECoG recordings allows for the TV-DBN model to measure, with high specificity, the influence regions of the brain have on each other. These TV-DBN models were generated in a phase-specific fashion with the performance of a reach-to-grasp task. By applying network measures to these connectivity models, it has been shown that the central electrodes for task performance are localized to areas of the brain previously implicated in the specific aspect of task performance occurring throughout task execution.

These findings are consistent across multiple subjects, despite variation in coverage and recording site density, suggesting that these responses are rather robust and involve the coordination of multiple distinct cortical regions. These phase-specific central electrode subsets also show modulation with task conditions, i.e., the configuration of the object being manipulated in a center-out reach-to-grasp task. These findings suggest that the PageRank centrality measure reveals the network involvement of brain regions as they evolve with the experimental task phases of visual processing, reaching, grasping, and object manipulation.

8.1.1.2.2 Stability Clustering

Stability clustering of ECoG high gamma power determined the number of inherent brain states for a visual naming task. This number of states was then used as input to k-means clustering to find functional units as they vary with task progression, at single trial resolution. The centroids for the most stable number of clusters provide an estimate of average activation patterns for the discrete cognitive processing phases. As a result of the successful application of the method, stability clustering could be used as the input to an unsupervised control system to allow for context-dependent task-switching, in effect increasing the degrees-of-freedom of a BCI system.

The final consistency of the clustering across trials and the number of inherent clusters varied between patients. This variability suggests that differing cognitive processes are occurring for the same task across the subject population. However, it is also possible that the areas contributing mainly to the modulation of the additional state did not receive coverage for the majority of subjects.

8.1.2 Limitations of ECoG Network Analysis

While ECoG has substantially improved spatial and temporal revolution relative to EEG, the main drawback is the inability to obtain global coverage with ECoG arrays. For the majority of studies, ECoG placement is determined by clinical need, making it impossible to target areas for implantation of specific importance to the BCI control task of interest.

ECoG is the recording of summed activity of large populations of neurons as they synchronize firing, creating a dipole. As a result of the summed activity of large groups of neurons modulating synchronously being detected by the electrode, it's impossible to infer the activity of small subsets of those neurons as they are implicated in task execution. To localize activity to minimal functional units in a cortical region, it became necessary to analyze single neuron recordings from microelectrode arrays.

8.1.2.1 Spike Community Detection

Eigenspectral clustering revealed that individual neurons were separated into distinct functional units during the performance of a reach-to-grasp task in a task specific manner.

These communities were not based on any obvious pattern, despite spatial distributions both with array location and depth of electrode penetration were analyzed. This supports the understanding that M1 cortex does not have a clear somatotopic representation at the individual digit resolution.

8.1.3 Limitations of Spikes

Spikes provide the highest possible spatial and temporal resolution of any electrophysiological recording. Coverage is even more limited with spikes than with ECoG, unfortunately, due to multielectrode arrays only being implantable within a single contiguous region of cortical gray matter. Due to hardware limitations, it's only possible to record from a small number of arrays simultaneously, and even if that weren't a limitation, implanting of arrays requires invasive surgery, so comprehensive coverage is not feasible. The combined effect of these limitations is that determining the information flow across all of the cortical regions relevant to a particular task is impractical at the single neuron level.

Connectivity models require measurement of the modulation of activity in disparate regions as they co-occur, suggesting that it's not possible to perfectly predict which areas are of value to record from for a particular task. With a given set of array placements, it's possible to infer that an area drives the activity of another area. With an additional area being covered simultaneously, however, it may become clear that this area actually serves as an intermediary, driving activity in one area, and being driven by the other area. Indirect connections such as these are not possible to detect without full coverage, as suggested by this example, as a result these methods cannot provide a full picture of the function of the brain given limitations of the extent and consistency of cortical coverage.

With technological improvements, it may be expected that electrode density will continue to increase, allowing for a better representation of the global cortical activity. As an alternative, the recordings of EEG, ECoG, microelectrodes, and even imaging could potentially be co-registered and overlaid to establish a global multiscale perspective. This would require either that the recordings are obtained simultaneously, or that the subject completes the task repeatedly under different recording methodologies, and the corresponding trials from the differing modalities are combined.

8.2 Future Work

There are many practical extensions of this connectivity work, for both online control of a BCI, and for neuroscientific discovery or clinical implementation of network-based activity mapping. Some direct extensions of this work are highlighted in this section.

8.2.1 Online Decoding

Centrality can improve online decoding in terms of efficiency and accuracy. A few training trials would first be run to find the connectivity networks. Centrality could then be used to determine which electrodes contribute most to the network. Those channels could then be selected in use for an online classifier or decoder.

This implementation could consist of directly using the centrality values that show the greatest task-relevant modulation. Alternatively, the connections between the most central channels could be used for decoding. A third approach would be to use the high-gamma power of the most central channels to decode directly. This final option is the most similar to current techniques, but improves upon them by using an unsupervised method for feature down-selection.

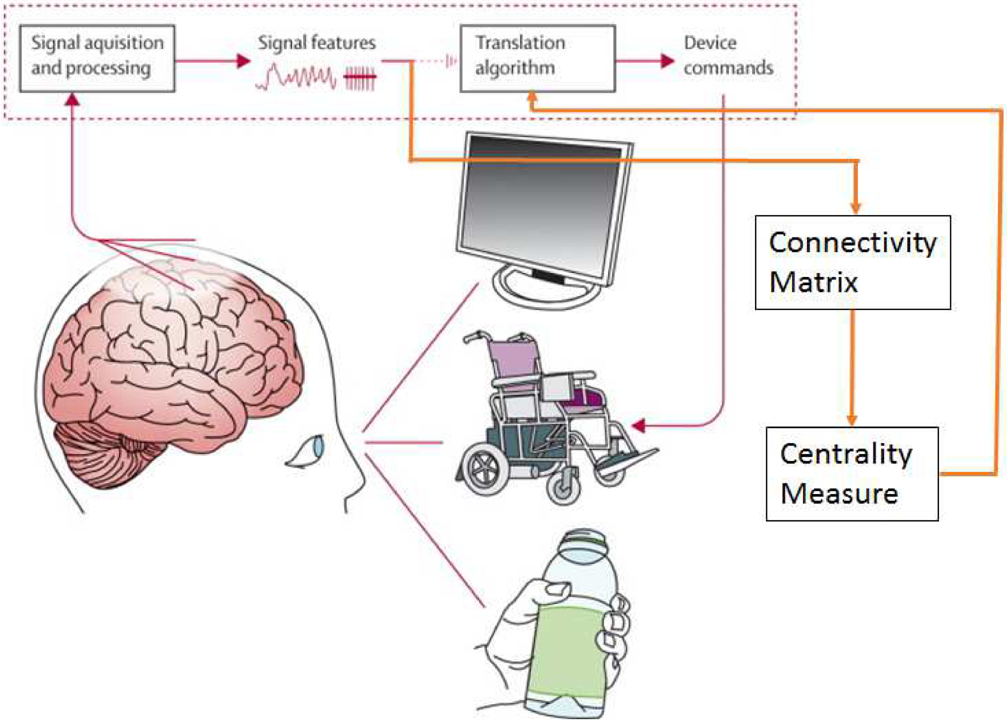

Figure 8.1: Basic overview of implementation of centrality decoder. The output of the centrality measure is fed directly into the translation algorithm in real-time in place of the signal features. Adapted from [Daly and Wolpaw, 2008]. (©Lancet, 2008)

8.2.2 Online Mapping

A system has been proposed for passive spatial-temporal functional mapping during a language task [Wang et al., 2016]. As ECoG patients perform the specified task, the high-gamma spectral power at each electrode is compared to baseline. This technique is used to localize task-related modulation in the cortex.

A similar system could be designed utilizing network measures. Connectivity models with centrality can be calculated on single trials. Upon each additional trial, the connectivity results can be averaged, and the centrality can be recalculated. As the connectivity structure converges to a stable network structure, the analysis can be completed for a predetermined statistical confidence level, without requiring additional training trials. This could be useful for seizure monitoring and localization, as well as for online BCI control feature selection.

8.2.2.1 Personalized PageRank

Personalized PageRank is a hybrid centrality measure which finds clusters based on the local structure of a network [Fogaras et al., 2005]. It is based on finding the connectivity structure of each individual node, and clustering based on locally strong connections [Haveliwala, 2002, Jeh and Widom, 2003].

Through the application of personalized PageRank to the connectivity measures of ECoG recordings, it becomes possible to combine the techniques utilized separately throughout this thesis, i.e., centrality and clustering. The personalized PageRank technique will find both which electrodes overlay task-specific cortical modulation drivers, as well as which electrodes they communicate most strongly with.

Through the application of this technique, a more holistic view of the network involvement of the electrodes to the task would be provided. One case where this could be useful could be in determining the specific network structure underlying a particular cortical area for a specific task phase. By limiting the analysis to performing the personalized pagerank calculation on the electrode of interest, it's possible to perform this analysis in real-time during ECoG recording sessions.

8.2.2.2 Centrality of Predetermined Clusters

Once clustering is found, e.g., using the eigenspectral clustering method, a cluster ordered adjacency matrix can be formed through a permutation.

$$A' = P^* A P, \tag{8.1}$$

where P is the permutation matrix consisting of all zeros except 1 for each element i, j where i is the original row and j is the row corresponding to the new ordering.

Each ordered sub-block of this matrix, consisting of n blocks, indicating the number of clusters, can then be separated into its own matrix, containing only the connectivity structure within that cluster. Centrality could then be found separately for each new matrix. This would indicate which electrodes contribute the most to the network structure of each cluster.

This can be seen as an inversion of the previously described personalized PageRank method. Instead of finding the connectivity structure of predetermined highly-central electrodes to elucidate localized clustering, the network would first be partitioned, and then centrality would be determined.

Techniques designed for segregated networks, which the partitioned network would become, have been described [Carreras et al., 2007]. Partitioning of the network prior to centrality calculation allows for the separate subnetworks to be analyzed independently in parallel [Bader and Madduri, 2008]. This could lead to substantially reduced computation time, and an increase in the feature space, e.g., number of electrodes included in the model, in a real-time system.

Bibliography

[Abele et al., 1997] Abele, M., Bürk, K., Andres, F., Topka, H., Laccone, F., Bösch, S., Brice, A., Cancel, G., Dichgans, J., and Klockgether, T. (1997). Autosomal dominant cerebellar ataxia type i. *Brain*, 120:2141–2148.

[Ackermann and Riecker, 2004] Ackermann, H. and Riecker, A. (2004). The contribution of the insula to motor aspects of speech production: a review and a hypothesis. *Brain and language*, 89(2):320–328.

[Adamos et al., 2008] Adamos, D. A., Kosmidis, E. K., and Theophilidis, G. (2008). Performance evaluation of pca-based spike sorting algorithms. *Computer methods and programs in biomedicine*, 91(3):232–244.

[Aggarwal et al., 2001] Aggarwal, C. C., Hinneburg, A., and Keim, D. A. (2001). *On the surprising behavior of distance metrics in high dimensional space*. Springer.

[Aggarwal et al., 2011] Aggarwal, V., Kerr, M., Davidson, A. G., Davoodi, R., Loeb, G. E., Schieber, M. H., and Thakor, N. V. (2011). Cortical control of reach and grasp kinematics in a virtual environment using musculoskeletal modeling software.

In *Neural Engineering (NER), 2011 5th International IEEE/EMBS Conference on*, pages 388–391. IEEE.

[Ahmad et al., 2012] Ahmad, I., Ansari, F., and Dey, U. (2012). A review of emg recording technique. *International Journal of Engineering Science and Technology*, 4(2):530–539.

[Akaike, 1974] Akaike, H. (1974). A new look at the statistical model identification. *Automatic Control, IEEE Transactions on*, 19(6):716–723.

[Allison et al., 2007] Allison, B. Z., Wolpaw, E. W., and Wolpaw, J. R. (2007). Brain–computer interface systems: progress and prospects. *Expert review of medical devices*, 4(4):463–474.

[Ameri et al., 2014] Ameri, A., Kamavuako, E. N., Scheme, E. J., Englehart, K. B., Parker, P., et al. (2014). Support vector regression for improved real-time, simultaneous myoelectric control. *Neural Systems and Rehabilitation Engineering, IEEE Transactions on*, 22(6):1198–1209.

[Andersen et al., 1992] Andersen, R. A., Brotchie, P. R., and Mazzoni, P. (1992). Evidence for the lateral intraparietal area as the parietal eye field. *Current opinion in neurobiology*, 2(6):840–846.

[Andersen et al., 1997] Andersen, R. A., Snyder, L. H., Bradley, D. C., and Xing, J. (1997). Multimodal representation of space in the posterior parietal cortex and its use in planning movements. *Annual review of neuroscience*, 20(1):303–330.

[Anthonisse, 1971] Anthonisse, J. M. (1971). The rush in a directed graph. *Stichting Mathematisch Centrum. Mathematische Besliskunde*, (BN 9/71):1–10.

[Arai et al., 2003] Arai, M., Tanaka, H., Pascual-Marqui, R. D., and Hirata, K. (2003). Reduced brain electric activities of frontal lobe in cortical cerebellar atrophy. *Clinical neurophysiology*, 114(4):740–747.

[Arslan and Sakarya, 2000] Arslan, G. and Sakarya, F. A. (2000). A unified neural-network-based speaker localization technique. *Neural Networks, IEEE Transactions on*, 11(4):997–1002.

[Arthur and Vassilvitskii, 2007] Arthur, D. and Vassilvitskii, S. (2007). k-means++: The advantages of careful seeding. In *Proceedings of the eighteenth annual ACM-SIAM symposium on Discrete algorithms*, pages 1027–1035. Society for Industrial and Applied Mathematics.

[Austin, 2006] Austin, D. (2006). How Google finds your needle in the webs haystack. *American Mathematical Society Feature Column*, 10:12.

[Baccala et al., 1998] Baccala, L., Sameshima, K., Ballester, G., Do Valle, A., and Timo-Iaria, C. (1998). Studying the interaction between brain structures via directed coherence and granger causality. *Applied Signal Processing*, 5(1):40.

[Baccalá et al., 2004] Baccalá, L. A., Alvarenga, M. Y., Sameshima, K., Jorge, C. L., and Castro, L. H. (2004). Graph theoretical characterization and tracking of the effective neural connectivity during episodes of mesial temporal epileptic seizure. *Journal of integrative neuroscience*, 3(04):379–395.

[Bader and Madduri, 2008] Bader, D. A. and Madduri, K. (2008). Snap, small-world network analysis and partitioning: an open-source parallel graph framework for the exploration of large-scale networks. In *Parallel and Distributed Processing, 2008. IPDPS 2008. IEEE International Symposium on*, pages 1–12. IEEE.

[Ball and Hall, 1965] Ball, G. H. and Hall, D. J. (1965). Isodata, an iterative method of multivariate analysis and pattern classification. In *IFIPS Congress*, pages 1–6.

[Bansal et al., 2012] Bansal, A. K., Truccolo, W., Vargas-Irwin, C. E., and Donoghue, J. P. (2012). Decoding 3d reach and grasp from hybrid signals in motor and premotor cortices: spikes, multiunit activity, and local field potentials. *Journal of neurophysiology*, 107(5):1337–1355.

[Battaglia et al., 2006] Battaglia, F., Quartarone, A., Ghilardi, M. F., Dattola, R., Bagnato, S., Rizzo, V., Morgante, L., and Girlanda, P. (2006). Unilateral cerebellar stroke disrupts movement preparation and motor imagery. *Clinical Neurophysiology*, 117(5):1009–1016.

[Baum et al., 1970] Baum, L. E., Petrie, T., Soules, G., and Weiss, N. (1970). A maximization technique occurring in the statistical analysis of probabilistic functions of markov chains. *The annals of mathematical statistics*, pages 164–171.

[Beauchamp et al., 2002] Beauchamp, M. S., Lee, K. E., Haxby, J. V., and Martin, A. (2002). Parallel visual motion processing streams for manipulable objects and human movements. *Neuron*, 34(1):149–159.

[Benz et al., 2012a] Benz, H., Collard, M., Tsimpouris, C., Acharya, S., Crone, N., Thakor, N., and Bezerianos, A. (2012a). Directed causality of the human electrocorticogram during dexterous movement. In *Engineering in Medicine and Biology Society (EMBC), 2012 Annual International Conference of the IEEE*, pages 1872–1875.

[Benz et al., 2012b] Benz, H. L., Zhang, H., Bezerianos, A., Acharya, S., Crone, N. E., Zheng, X., and Thakor, N. V. (2012b). Connectivity analysis as a novel approach to motor decoding for prosthesis control. *Neural Systems and Rehabilitation Engineering, IEEE Transactions on*, 20(2):143–152.

[Blackwood, 2000] Blackwood, D. (2000). P300, a state and a trait marker in schizophrenia. *The Lancet*, 355(9206):771–772.

[Blunsom, 2004] Blunsom, P. (2004). Hidden markov models. *Lecture notes*, 15:18–19.

[Bonacich, 1987] Bonacich, P. (1987). Power and centrality: A family of measures. *American Journal of Sociology*, 92(5):pp. 1170–1182.

[Bos et al., 2002] Bos, R., De Waele, S., and Broersen, P. M. (2002). Autoregressive spectral estimation by application of the burg algorithm to irregularly sampled data. *Instrumentation and Measurement, IEEE Transactions on*, 51(6):1289–1294.

[Boudrias et al., 2006] Boudrias, M.-H., Belhaj-Saïf, A., Park, M. C., and Cheney, P. D. (2006). Contrasting properties of motor output from the supplementary motor area and primary motor cortex in rhesus macaques. *Cerebral Cortex*, 16(5):632–638.

[Brent, 1973] Brent, R. P. (1973). *Algorithms for minimization without derivatives.* Courier Dover Publications.

[Brooks, 1986] Brooks, V. B. (1986). *The neural basis of motor control.* Oxford University Press.

[Brovelli et al., 2004] Brovelli, A., Ding, M., Ledberg, A., Chen, Y., Nakamura, R., and Bressler, S. L. (2004). Beta oscillations in a large-scale sensorimotor cortical network: directional influences revealed by granger causality. *Proceedings of the National Academy of Sciences of the United States of America*, 101(26):9849–9854.

[Brown, 1959] Brown, J. R. (1959). Degenerative cerebellar ataxias. *Neurology*, 9(12):799–799.

[Bullmore and Sporns, 2012] Bullmore, E. and Sporns, O. (2012). The economy of brain network organization. *Nature Reviews Neuroscience*, 13(5):336–349.

[Burnham and Anderson, 2002] Burnham, K. P. and Anderson, D. R. (2002). *Model selection and multimodel inference: a practical information-theoretic approach.* Springer Science & Business Media.

[Burns et al., 2012] Burns, S. P., Sritharan, D., Jouny, C., Bergey, G., Crone, N., Anderson, W. S., and Sarma, S. V. (2012). A network analysis of the dynamics of seizure. In *Engineering in Medicine and Biology Society (EMBC), 2012 Annual International Conference of the IEEE*, pages 4684–4687. IEEE.

[Bushnell et al., 1981] Bushnell, M. C., Goldberg, M. E., and Robinson, D. L. (1981). Behavioral enhancement of visual responses in monkey cerebral cortex. i. modulation in posterior parietal cortex related to selective visual attention. *Journal of Neurophysiology*, 46(4):755–772.

[Buzsáki et al., 2012] Buzsáki, G., Anastassiou, C. A., and Koch, C. (2012). The origin of extracellular fields and currentseeg, ecog, lfp and spikes. *Nature reviews neuroscience*, 13(6):407–420.

[Canolty et al., 2006] Canolty, R. T., Edwards, E., Dalal, S. S., Soltani, M., Nagarajan, S. S., Kirsch, H. E., Berger, M. S., Barbaro, N. M., and Knight, R. T. (2006). High gamma power is phase-locked to theta oscillations in human neocortex. *science*, 313(5793):1626–1628.

[Carreras et al., 2007] Carreras, I., Miorandi, D., Canright, G. S., and Engø-Monsen, K. (2007). Eigenvector centrality in highly partitioned mobile networks: Principles and applications. In *Advances in biologically inspired information systems*, pages 123–145. Springer.

[Center et al., 2013] Center, N. S. C. I. S. et al. (2013). Spinal cord injury facts and figures at a glance. *The journal of spinal cord medicine*, 36(1):1.

[Ceyssens et al., 2013] Ceyssens, F., van Kuyck, K., Nuttin, B., and Puers, R. (2013). Long term lfp measurements with ultra-fine neural electrodes embedded in porous resorbable carrier. In *Solid-State Sensors, Actuators and Microsystems (TRANSDUCERS & EUROSENSORS XXVII), 2013 Transducers & Eurosensors XXVII: The 17th International Conference on*, pages 868–871. IEEE.

[Chang et al., 2015] Chang, S.-Y., Edwards, E., Morgan, N., Ellis, D., Mesgarani, N., and Chang, E. (2015). Phone recognition for mixed speech signals: Comparison of human auditory cortex and machine performance.

[Chao et al., 1999] Chao, L. L., Haxby, J. V., and Martin, A. (1999). Attribute-based neural substrates in temporal cortex for perceiving and knowing about objects. *Nature neuroscience*, 2(10):913–919.

[Chao and Martin, 2000] Chao, L. L. and Martin, A. (2000). Representation of manipulable man-made objects in the dorsal stream. *Neuroimage*, 12(4):478–484.

[Chatterjee et al., 2007] Chatterjee, A., Aggarwal, V., Ramos, A., Acharya, S., and Thakor, N. V. (2007). Journal of neuroengineering and rehabilitation. *Journal of NeuroEngineering and Rehabilitation*, 4:40.

[Chen et al., 2007] Chen, P., Xie, H., Maslov, S., and Redner, S. (2007). Finding scientific gems with googles pagerank algorithm. *Journal of Informetrics*, 1(1):8–15.

[Chestek et al., 2013] Chestek, C. A., Gilja, V., Blabe, C. H., Foster, B. L., Shenoy, K. V., Parvizi, J., and Henderson, J. M. (2013). Hand posture classification using electrocorticography signals in the gamma band over human sensorimotor brain areas. *Journal of Neural Engineering*, 10(2):026002.

[Childress, 1969] Childress, D. S. (1969). A myoelectric three-state controller using rate sensitivity. In *Digest of the International Conference on Medical and Biological Engineering*, volume 8.

[Chu et al., 2007] Chu, J.-U., Moon, I., Lee, Y.-J., Kim, S.-K., and Mun, M.-S. (2007). A supervised feature-projection-based real-time emg pattern recognition for multifunction myoelectric hand control. *Mechatronics, IEEE/ASME Transactions on*, 12(3):282–290.

[Cisek, 2006] Cisek, P. (2006). Integrated neural processes for defining potential actions and deciding between them: a computational model. *The Journal of Neuroscience*, 26(38):9761–9770.

[Clementz et al., 1997] Clementz, B. A., Geyer, M. A., and Braff, D. L. (1997). P50 suppression among schizophrenia and normal comparison subjects: a methodological analysis. *Biological psychiatry*, 41(10):1035–1044.

[Cox, 1996] Cox, D. D. (1996). Spectral analysis for physical applications: Multitaper and conventional univariate techniques. *Technometrics*, 38(3):294–294.

[Crone and Hao, 2002] Crone, N. E. and Hao, L. (2002). The functional significance of event-related spectral changes (erd/ers) from the perspective of electrocorticography. *Supplements to Clinical Neurophysiology*, 54:435–442.

[Crone et al., 2011] Crone, N. E., Korzeniewska, A., and Franaszczuk, P. J. (2011). Cortical gamma responses: Searching high and low. *International Journal of Psychophysiology*, 79(1):9 – 15. Special Issue: Correlations between gamma-band oscillations and human behaviour.

[Crone et al., 1998] Crone, N. E., Miglioretti, D. L., Gordon, B., and Lesser, R. P.

(1998). Functional mapping of human sensorimotor cortex with electrocorticographic spectral analysis. ii. *Brain*, 121:2301–2315.

[Curran and Stokes, 2003] Curran, E. A. and Stokes, M. J. (2003). Learning to control brain activity: a review of the production and control of eeg components for driving brain–computer interface (bci) systems. *Brain and cognition*, 51(3):326–336.

[Daly and Wolpaw, 2008] Daly, J. J. and Wolpaw, J. R. (2008). Brain–computer interfaces in neurological rehabilitation. *The Lancet Neurology*, 7(11):1032–1043.

[Danon et al., 2005] Danon, L., Diaz-Guilera, A., Duch, J., and Arenas, A. (2005). Comparing community structure identification. *Journal of Statistical Mechanics: Theory and Experiment*, 2005(09):P09008.

[Dawson et al., 1988] Dawson, G., Finley, C., Phillips, S., Galpert, L., and Lewy, A. (1988). Reduced p3 amplitude of the event-related brain potential: Its relationship to language ability in austism. *Journal of autism and developmental disorders*, 18(4):493–504.

[de Vico Fallani et al., 2015] de Vico Fallani, F., Corazzol, M., Sternberg, J., Wyart, C., and Chavez, M. (2015). Hierarchy of neural organization in the embryonic spinal cord: Granger-causality graph analysis of in vivo calcium imaging data. *Neural Systems and Rehabilitation Engineering, IEEE Transactions on*, 23(3):333–341.

[del Ama et al., 2012] del Ama, A. J., Koutsou, A. D., Moreno, J. C., de-los Reyes, A., Gil-Agudo, A., and Pons, J. L. (2012). Review of hybrid exoskeletons to restore gait following spinal cord injury. *Journal of Rehabilitation Research and Development*, 49(4):497–514.

[Dhamala et al., 2008] Dhamala, M., Rangarajan, G., and Ding, M. (2008). Analyzing information flow in brain networks with nonparametric granger causality. *NeuroImage*, 41(2):354–362.

[Donoghue et al., 1998] Donoghue, J. P., Sanes, J. N., Hatsopoulos, N. G., and Gaál, G. (1998). Neural discharge and local field potential oscillations in primate motor cortex during voluntary movements. *Journal of Neurophysiology*, 79(1):159–173.

[Drineas et al., 2004] Drineas, P., Frieze, A., Kannan, R., Vempala, S., and Vinay, V. (2004). Clustering large graphs via the singular value decomposition. *Machine learning*, 56(1-3):9–33.

[Dum and Strick, 2002] Dum, R. P. and Strick, P. L. (2002). Motor areas in the frontal lobe of the primate. *Physiology & behavior*, 77(4):677–682.

[Duncan et al., 2004] Duncan, J. S., Papademetris, X., Yang, J., Jackowski, M., Zeng, X., and Staib, L. H. (2004). Geometric strategies for neuroanatomic analysis from mri. *Neuroimage*, 23:S34–S45.

[Englehart et al., 2001] Englehart, K., Hudgin, B., Parker, P., et al. (2001). A wavelet-based continuous classification scheme for multifunction myoelectric control. *Biomedical Engineering, IEEE Transactions on*, 48(3):302–311.

[Englehart et al., 1999a] Englehart, K., Hudgins, B., Parker, P., and Stevenson, M. (1999a). Improving myoelectric signal classification using wavelet packets and principal components analysis. *Proc. IEEE*, 1:569–570.

[Englehart et al., 1999b] Englehart, K., Hudgins, B., Parker, P. A., and Stevenson, M. (1999b). Classification of the myoelectric signal using time-frequency based representations. *Medical engineering & physics*, 21(6):431–438.

[Ermann et al., 2013] Ermann, L., Frahm, K. M., and Shepelyansky, D. L. (2013). Spectral properties of google matrix of wikipedia and other networks. *The European Physical Journal B*, 86(5):1–10.

[Flinker et al., 2010a] Flinker, A., Chang, E. F., Kirsch, H. E., Barbaro, N. M., Crone, N. E., and Knight, R. T. (2010a). Single-trial speech suppression of auditory cortex activity in humans. *The Journal of Neuroscience*, 30(49):16643–16650.

[Flinker et al., 2010b] Flinker, A., Chang, E. F., Kirsch, H. E., Barbaro, N. M., Crone, N. E., and Knight, R. T. (2010b). Single-trial speech suppression of auditory cortex activity in humans. *The Journal of Neuroscience*, 30(49):16643–16650.

[Fogaras et al., 2005] Fogaras, D., Rácz, B., Csalogány, K., and Sarlós, T. (2005). Towards scaling fully personalized pagerank: Algorithms, lower bounds, and experiments. *Internet Mathematics*, 2(3):333–358.

[Forbach et al., 1974] Forbach, G. B., Stanners, R. F., and Hochhaus, L. (1974). Repetition and practice effects in a lexical decision task. *Memory & Cognition*, 2(2):337–339.

[Ford and Moore, 1998] Ford, J. J. and Moore, J. B. (1998). Adaptive estimation of hmm transition probabilities. *Signal Processing, IEEE Transactions on*, 46(5):1374–1385.

[Forsythe et al., 1977] Forsythe, G. E., Malcolm, M. A., and Moler, C. B. (1977). *Computer methods for mathematical computations*. Prentice Hall Professional Technical Reference.

[Fougner et al., 2012] Fougner, A., Stavdahl, Ø., Kyberd, P. J., Losier, Y. G., Parker, P., et al. (2012). Control of upper limb prostheses: terminology and proportional myoelectric controla review. *Neural Systems and Rehabilitation Engineering, IEEE Transactions on*, 20(5):663–677.

[Franaszczuk et al., 1994] Franaszczuk, P. J., Bergey, G. K., and Kamiski, M. J. (1994). Analysis of mesial temporal seizure onset and propagation using the directed transfer function method. *Electroencephalography and Clinical Neurophysiology*, 91(6):413 – 427.

[Freeman, 1977] Freeman, L. C. (1977). A set of measures of centrality based on betweenness. *Sociometry*, pages 35–41.

[Freeman, 1979] Freeman, L. C. (1979). Centrality in social networks conceptual clarification. *Social networks*, 1(3):215–239.

[Freeman and Zhai, 2009] Freeman, W. J. and Zhai, J. (2009). Simulated power spectral density (psd) of background electrocorticogram (ecog). *Cognitive neurodynamics*, 3(1):97–103.

[Fridlyand and Dudoit, 2001] Fridlyand, J. and Dudoit, S. (2001). Applications of resampling methods to estimate the number of clusters and to improve the accuracy of a clustering method. Technical report, Citeseer.

[Frodl et al., 2002] Frodl, T., Hampel, H., Juckel, G., Bürger, K., Padberg, F., Engel, R. R., Möller, H.-j., and Hegerl, U. (2002). Value of event-related p300 subcomponents in the clinical diagnosis of mild cognitive impairment and alzheimer's disease. *Psychophysiology*, 39(2):175–181.

[Geweke, 1982] Geweke, J. (1982). Measurement of linear dependence and feedback between multiple time series. *Journal of the American Statistical Association*, 77(378):304–313.

[Ghosh et al., 2012] Ghosh, S., Viswanath, B., Kooti, F., Sharma, N. K., Korlam, G., Benevenuto, F., Ganguly, N., and Gummadi, K. P. (2012). Understanding and combating link farming in the twitter social network. In *Proceedings of the 21st international conference on World Wide Web*, pages 61–70. ACM.

[Gold et al., 2011] Gold, B., Morgan, N., and Ellis, D. (2011). *Speech and audio signal processing: processing and perception of speech and music*. John Wiley & Sons.

[González et al., 2005] González, B., Rodríguez, M., Ramirez, C., and Sabaté, M. (2005). Disturbance of motor imagery after cerebellar stroke. *Behavioral neuroscience*, 119(2):622.

[Goodale, 1998] Goodale, M. A. (1998). Visuomotor control: Where does vision end and action begin? *Current Biology*, 8(14):R489–R491.

[Goodale, 2011] Goodale, M. A. (2011). Transforming vision into action. *Vision research*, 51(13):1567–1587.

[Goodale and Milner, 1992] Goodale, M. A. and Milner, A. D. (1992). Separate visual pathways for perception and action. *Trends in neurosciences*, 15(1):20–25.

[Goutte et al., 2001] Goutte, C., Hansen, L. K., Liptrot, M. G., and Rostrup, E. (2001). Feature-space clustering for fmri meta-analysis. *Human brain mapping*, 13(3):165–183.

[Granger, 1969a] Granger, C. W. (1969a). Investigating causal relations by econometric models and cross-spectral methods. *Econometrica: Journal of the Econometric Society*, pages 424–438.

[Granger, 1969b] Granger, C. W. (1969b). Investigating causal relations by econometric models and cross-spectral methods. *Econometrica: Journal of the Econometric Society*, pages 424–438.

[Granger, 1988] Granger, C. W. (1988). Some recent development in a concept of causality. *Journal of econometrics*, 39(1):199–211.

[Graziano et al., 1994] Graziano, M., Andersen, R. A., and Snowden, R. J. (1994). Tuning of mst neurons to spiral motions. *The Journal of neuroscience*, 14(1):54–67.

[Grimme et al., 2011] Grimme, B., Fuchs, S., Perrier, P., and Schöner, G. (2011).

Limb versus speech motor control: A conceptual review. *Motor control*, 15(1):5–33.

[Groppe et al., 2013] Groppe, D. M., Bickel, S., Keller, C. J., Jain, S. K., Hwang, S. T., Harden, C., and Mehta, A. D. (2013). Dominant frequencies of resting human brain activity as measured by the electrocorticogram. *Neuroimage*, 79:223–233.

[Grunau and Low, 1987] Grunau, R. V. and Low, M. D. (1987). Cognitive and task-related eeg correlates of arithmetic performance in adolescents. *Journal of clinical and experimental neuropsychology*, 9(5):563–574.

[Guger et al., 2003] Guger, C., Edlinger, G., Harkam, W., Niedermayer, I., and Pfurtscheller, G. (2003). How many people are able to operate an eeg-based brain-computer interface (bci)? *Neural Systems and Rehabilitation Engineering, IEEE Transactions on*, 11(2):145–147.

[Hall and Wellman, 1985] Hall, A. and Wellman, B. (1985). Social networks and social support.

[Haveliwala et al., 2003] Haveliwala, T., Kamvar, S., Klein, D., Manning, C., and Golub, G. (2003). Computing pagerank using power extrapolation. *Stanford University Technical Report.*

[Haveliwala, 2002] Haveliwala, T. H. (2002). Topic-sensitive pagerank. In *Proceedings of the 11th international conference on World Wide Web*, pages 517–526. ACM.

[Hayman and Tulving, 1989] Hayman, C. G. and Tulving, E. (1989). Is priming in fragment completion based on a" traceless" memory system? *Journal of Experimental Psychology: Learning, Memory, and Cognition*, 15(5):941.

[Heldman et al., 2006] Heldman, D., Wang, W., Chan, S. S., Moran, D. W., et al. (2006). Local field potential spectral tuning in motor cortex during reaching. *Neural Systems and Rehabilitation Engineering, IEEE Transactions on*, 14(2):180–183.

[Hickok and Poeppel, 2007] Hickok, G. and Poeppel, D. (2007). The cortical organization of speech processing. *Nature Reviews Neuroscience*, 8(5):393–402.

[Hirtz et al., 2007] Hirtz, D., Thurman, D., Gwinn-Hardy, K., Mohamed, M., Chaudhuri, A., and Zalutsky, R. (2007). How common are the common neurologic disorders? *Neurology*, 68(5):326–337.

[Hubel and Wiesel, 1968] Hubel, D. H. and Wiesel, T. N. (1968). Receptive fields and functional architecture of monkey striate cortex. *The Journal of physiology*, 195(1):215–243.

[Hubert and Levin, 1976] Hubert, L. J. and Levin, J. R. (1976). A general statistical framework for assessing categorical clustering in free recall. *Psychological bulletin*, 83(6):1072.

[Humphries, 2011] Humphries, M. D. (2011). Spike-train communities: finding groups of similar spike trains. *The Journal of Neuroscience*, 31(6):2321–2336.

[Jaccard, 1912] Jaccard, P. (1912). The distribution of the flora in the alpine zone. 1. *New phytologist*, 11(2):37–50.

[Jain et al., 1999] Jain, A. K., Murty, M. N., and Flynn, P. J. (1999). Data clustering: a review. *ACM computing surveys (CSUR)*, 31(3):264–323.

[Jeannerod, 1994] Jeannerod, M. (1994). Motor representations and reality. *Behavioral and Brain sciences*, 17(02):229–245.

[Jeh and Widom, 2003] Jeh, G. and Widom, J. (2003). Scaling personalized web search. In *Proceedings of the 12th international conference on World Wide Web*, pages 271–279. ACM.

[Jing and Baluja, 2008] Jing, Y. and Baluja, S. (2008). Visualrank: Applying pagerank to large-scale image search. *Pattern Analysis and Machine Intelligence, IEEE Transactions on*, 30(11):1877–1890.

[Jolliffe, 2005] Jolliffe, I. (2005). *Principal component analysis*. Wiley Online Library.

[Jung et al., 2006] Jung, H. K., Choi, J. H., and Kim, T. (2006). Solving alignment problems in neural spike sorting using frequency domain pca. *Neurocomputing*, 69(7):975–978.

[Kaminski and Blinowska, 1991] Kaminski, M. and Blinowska, K. (1991). A new method of the description of the information flow in the brain structures. *Biological cybernetics*, 65(3):203–210.

[Kamvar et al., 2003] Kamvar, S. D., Haveliwala, T. H., Manning, C. D., and Golub, G. H. (2003). Extrapolation methods for accelerating pagerank computations. In *Proceedings of the 12th international conference on World Wide Web*, pages 261–270. ACM.

[Karlsson et al., 1999] Karlsson, S., Yu, J., and Akay, M. (1999). Enhancement of spectral analysis of myoelectric signals during static contractions using wavelet methods. *Biomedical Engineering, IEEE Transactions on*, 46(6):670–684.

[Katyal et al., 2013] Katyal, K. D., Johannes, M. S., McGee, T. G., Harris, A. J., Armiger, R. S., Firpi, A. H., McMullen, D., Hotson, G., Fifer, M. S., Crone, N. E., et al. (2013). Harmonie: A multimodal control framework for human assistive robotics. In *Neural Engineering (NER), 2013 6th International IEEE/EMBS Conference on*, pages 1274–1278. IEEE.

[KERMADI, 1997] KERMADI, Y. LIU, A. T. E. R. I. (1997). Effects of reversible inactivation of the supplementary motor area (sma) on unimanual grasp and bimanual pull and grasp performance in monkeys. *Somatosensory & motor research*, 14(4):268–280.

[Kermadi, 2000] Kermadi, Y. Liu, E. R. I. (2000). Do bimanual motor actions involve the dorsal premotor (pmd), cingulate (cma) and posterior parietal (ppc) cortices? comparison with primary and supplementary motor cortical areas. *Somatosensory & motor research*, 17(3):255–271.

[Kim and McNames, 2007] Kim, S. and McNames, J. (2007). Automatic spike detection based on adaptive template matching for extracellular neural recordings. *Journal of neuroscience methods*, 165(2):165–174.

[Knight et al., 2007] Knight, R. T. et al. (2007). Neural networks debunk phrenology. *SCIENCE-NEW YORK THEN WASHINGTON-*, 316(5831):1578.

[Ko et al., 2013] Ko, A. L., Weaver, K. E., Hakimian, S., and Ojemann, J. G. (2013). Identifying functional networks using endogenous connectivity in gamma band electrocorticography. *Brain Connect*, 3(5):491–502.

[Koike et al., 2015] Koike, Y., Yoshimura, N., Shin, D., and Kambara, H. (2015). Motor control theory and brain-machine interfaces. In *Clinical Systems Neuroscience*, pages 67–81. Springer.

[Komatsu and Wurtz, 1988] Komatsu, H. and Wurtz, R. H. (1988). Relation of cortical areas mt and mst to pursuit eye movements. i. localization and visual properties of neurons. *Journal of Neurophysiology*, 60(2):580–603.

[Korzeniewska et al., 2008] Korzeniewska, A., Crainiceanu, C. M., Kuś, R., Franaszczuk, P. J., and Crone, N. E. (2008). Dynamics of event-related causality in brain electrical activity. *Human brain mapping*, 29(10):1170–1192.

[Korzeniewska et al., 2011] Korzeniewska, A., Franaszczuk, P. J., Crainiceanu, C. M., Kuś, R., and Crone, N. E. (2011). Dynamics of large-scale cortical interactions at high gamma frequencies during word production: event related causality (ERC) analysis of human electrocorticography (ecog). *Neuroimage*, 56(4):2218–2237.

[Kuiken et al., 2004] Kuiken, T. A., Dumanian, G., Lipschutz, R., Miller, L., and Stubblefield, K. (2004). The use of targeted muscle reinnervation for improved myoelectric prosthesis control in a bilateral shoulder disarticulation amputee. *Prosthetics and Orthotics International*, 28(3):245–253.

[Kuiken et al., 2009] Kuiken, T. A., Li, G., Lock, B. A., Lipschutz, R. D., Miller,

L. A., Stubblefield, K. A., and Englehart, K. B. (2009). Targeted muscle reinnervation for real-time myoelectric control of multifunction artificial arms. *Jama*, 301(6):619–628.

[Kuiken et al., 2007a] Kuiken, T. A., Marasco, P. D., Lock, B. A., Harden, R. N., and Dewald, J. P. (2007a). Redirection of cutaneous sensation from the hand to the chest skin of human amputees with targeted reinnervation. *Proceedings of the National Academy of Sciences*, 104(50):20061–20066.

[Kuiken et al., 2007b] Kuiken, T. A., Miller, L. A., Lipschutz, R. D., Lock, B. A., Stubblefield, K., Marasco, P. D., Zhou, P., and Dumanian, G. A. (2007b). Targeted reinnervation for enhanced prosthetic arm function in a woman with a proximal amputation: a case study. *The Lancet*, 369(9559):371–380.

[Kunegis et al., 2009] Kunegis, J., Lommatzsch, A., and Bauckhage, C. (2009). The slashdot zoo: mining a social network with negative edges. In *Proceedings of the 18th international conference on World wide web*, pages 741–750. ACM.

[Kwon et al., 1999] Kwon, J. S., O'Donnell, B. F., Wallenstein, G. V., Greene, R. W., Hirayasu, Y., Nestor, P. G., Hasselmo, M. E., Potts, G. F., Shenton, M. E., and McCarley, R. W. (1999). Gamma frequency–range abnormalities to auditory stimulation in schizophrenia. *Archives of general psychiatry*, 56(11):1001–1005.

[Lacquaniti, 1989] Lacquaniti, F. (1989). Central representations of human limb movement as revealed by studies of drawing and handwriting. *Trends in neurosciences*, 12(8):287–291.

[Lange et al., 2004] Lange, T., Roth, V., Braun, M. L., and Buhmann, J. M. (2004). Stability-based validation of clustering solutions. *Neural computation*, 16(6):1299–1323.

[Lau et al., 1995] Lau, H.-K., Liu, J., Pereira, B. P., Kumar, V. P., and Pho, R. W. (1995). Fatigue reduction by sequential stimulation of multiple motor points in a muscle. *Clinical orthopaedics and related research*, 321:251–258.

[Lebedev et al., 2005] Lebedev, M. A., Carmena, J. M., O'Doherty, J. E., Zacksenhouse, M., Henriquez, C. S., Principe, J. C., and Nicolelis, M. A. (2005). Cortical ensemble adaptation to represent velocity of an artificial actuator controlled by a brain-machine interface. *The Journal of neuroscience*, 25(19):4681–4693.

[Lemon, 2008] Lemon, R. N. (2008). Descending pathways in motor control. *Annu. Rev. Neurosci.*, 31:195–218.

[Letelier and Weber, 2000] Letelier, J. C. and Weber, P. P. (2000). Spike sorting based on discrete wavelet transform coefficients. *Journal of neuroscience methods*, 101(2):93–106.

[Levine and Domany, 2001] Levine, E. and Domany, E. (2001). Resampling method for unsupervised estimation of cluster validity. *Neural computation*, 13(11):2573–2593.

[Liu et al., 2015] Liu, S., Ince, N. F., Sabanci, A., Aydoseli, A., Aras, Y., Sencer, A., Bebek, N., Sha, Z., and Gurses, C. (2015). Detection of high frequency oscillations in epilepsy with k-means clustering method. In *Neural Engineering (NER), 2015 7th International IEEE/EMBS Conference on*, pages 934–937. IEEE.

[Liversedge and Emery, 1961] Liversedge, L. and Emery, V. (1961). Electroencephalographic changes in cerebellar degenerative lesions. *Journal of neurology, neurosurgery, and psychiatry*, 24(4):326.

[Marsden et al., 2000] Marsden, J., Werhahn, K., Ashby, P., Rothwell, J., Noachtar, S., and Brown, P. (2000). Organization of cortical activities related to movement in humans. *The Journal of Neuroscience*, 20(6):2307–2314.

[McFarland et al., 1997] McFarland, D. J., McCane, L. M., David, S. V., and Wolpaw, J. R. (1997). Spatial filter selection for eeg-based communication. *Electroencephalography and clinical Neurophysiology*, 103(3):386–394.

[McFarland et al., 2010] McFarland, D. J., Sarnacki, W. A., and Wolpaw, J. R. (2010). Electroencephalographic (eeg) control of three-dimensional movement. *Journal of Neural Engineering*, 7(3):036007.

[McLachlan, 2004] McLachlan, G. (2004). *Discriminant analysis and statistical pattern recognition*, volume 544. John Wiley & Sons.

[McMullen et al., 2015] McMullen, D. P., Fifer, M. S., Wester, B. A., Hotson, G., Katyal, K. D., Johannes, M. S., McGee, T. G., Harris, A., Ravitz, A. D., McLoughlin, M. P., et al. (2015). Semi-autonomous hybrid brain-machine interface. In *Brain-Computer Interface Research*, pages 89–104. Springer.

[McMullen et al., 2014] McMullen, D. P., Hotson, G., Katyal, K. D., Wester, B., Fifer, M. S., McGee, T. G., Harris, A., Johannes, M. S., Vogelstein, R. J., Ravitz, A. D., et al. (2014). Demonstration of a semi-autonomous hybrid brain–machine interface using human intracranial eeg, eye tracking, and computer vision to control a robotic upper limb prosthetic. *Neural Systems and Rehabilitation Engineering, IEEE Transactions on*, 22(4):784–796.

[McPhedran et al., 1965] McPhedran, A. M., Wuerker, R. B., and Henneman, E. (1965). Properties of motor units in a homogeneous red muscle (soleus) of the cat. *Journal of Neurophysiology*, 28(1):71–84.

[Melssen and Epping, 1987] Melssen, W. and Epping, W. (1987). Detection and estimation of neural connectivity based on crosscorrelation analysis. *Biological cybernetics*, 57(6):403–414.

[Mihalcea et al., 2004] Mihalcea, R., Tarau, P., and Figa, E. (2004). Pagerank on semantic networks, with application to word sense disambiguation. In *Proceedings of the 20th international conference on Computational Linguistics*, page 1126. Association for Computational Linguistics.

[Miller et al., 2009] Miller, K., Zanos, S., Fetz, E., Den Nijs, M., and Ojemann, J. (2009). Decoupling the cortical power spectrum reveals real-time representation of individual finger movements in humans. *The Journal of Neuroscience*, 29(10):3132–3137.

[Miller et al., 2007] Miller, K. J., Leuthardt, E. C., Schalk, G., Rao, R. P., Anderson,

N. R., Moran, D. W., Miller, J. W., and Ojemann, J. G. (2007). Spectral changes in cortical surface potentials during motor movement. *The Journal of neuroscience*, 27(9):2424–2432.

[Miller et al., 2008] Miller, L., Stubblefield, K., Lipschutz, R. D., Lock, B., Kuiken, T., et al. (2008). Improved myoelectric prosthesis control using targeted reinnervation surgery: a case series. *Neural Systems and Rehabilitation Engineering, IEEE Transactions on*, 16(1):46–50.

[Milligan and Cooper, 1985] Milligan, G. W. and Cooper, M. C. (1985). An examination of procedures for determining the number of clusters in a data set. *Psychometrika*, 50(2):159–179.

[Milner and Goodale, 1995] Milner, A. D. and Goodale, M. A. (1995). *The visual brain in action*, volume 27. England.

[Mizruchi et al., 1986] Mizruchi, M. S., Mariolis, P., Schwartz, M., and Mintz, B. (1986). Techniques for disaggregating centrality scores in social networks. *Sociological methodology*, 16(26-48):30.

[Modha and Spangler, 2003] Modha, D. S. and Spangler, W. S. (2003). Feature weighting in k-means clustering. *Machine learning*, 52(3):217–237.

[Mollazadeh et al., 2008] Mollazadeh, M., Aggarwal, V., Singhal, G., Law, A., Davidson, A., Schieber, M., and Thakor, N. (2008). Spectral modulation of lfp activity in m1 during dexterous finger movements. In *Engineering in Medicine and Biology*

Society, 2008. EMBS 2008. 30th Annual International Conference of the IEEE, pages 5314–5317. IEEE.

[Moran, 2010] Moran, D. (2010). Evolution of brain–computer interface: action potentials, local field potentials and electrocorticograms. *Current opinion in neurobiology*, 20(6):741–745.

[Murata et al., 2000] Murata, A., Gallese, V., Luppino, G., Kaseda, M., and Sakata, H. (2000). Selectivity for the shape, size, and orientation of objects for grasping in neurons of monkey parietal area aip. *Journal of neurophysiology*, 83(5):2580–2601.

[Naeem et al., 2009] Naeem, M., Brunner, C., and Pfurtscheller, G. (2009). Dimensionality reduction and channel selection of motor imagery electroencephalographic data. *Computational intelligence and neuroscience*, 2009.

[Nangini et al., 2006] Nangini, C., Ross, B., Tam, F., and Graham, S. (2006). Magnetoencephalographic study of vibrotactile evoked transient and steady-state responses in human somatosensory cortex. *Neuroimage*, 33(1):252–262.

[Newman, 2010] Newman, M. (2010). *Networks: an introduction.* Oxford University Press.

[Newman, 2006] Newman, M. E. (2006). Modularity and community structure in networks. *Proceedings of the National Academy of Sciences*, 103(23):8577–8582.

[Ng et al., 2002] Ng, A. Y., Jordan, M. I., Weiss, Y., et al. (2002). On spectral clustering: Analysis and an algorithm. *Advances in neural information processing systems*, 2:849–856.

[Nicolelis and Lebedev, 2009] Nicolelis, M. A. and Lebedev, M. A. (2009). Principles of neural ensemble physiology underlying the operation of brain–machine interfaces. *Nature Reviews Neuroscience*, 10(7):530–540.

[Ortega et al., 2008] Ortega, G. J., Sola, R. G., and Pastor, J. (2008). Complex network analysis of human ECoG data. *Neuroscience letters*, 447(2):129–133.

[Owings and Kozak, 1998] Owings, M. F. and Kozak, L. J. (1998). Ambulatory and inpatient procedures in the united states, 1996. *Vital and health statistics. Series 13, Data from the National Health Survey*, 13(139):1–119.

[Page et al., 1999] Page, L., Brin, S., Motwani, R., and Winograd, T. (1999). The pagerank citation ranking: Bringing order to the web. Technical Report 1999-66, Stanford InfoLab. Previous number = SIDL-WP-1999-0120.

[Parker et al., 2006] Parker, P., Englehart, K., and Hudgins, B. (2006). Myoelectric signal processing for control of powered limb prostheses. *Journal of electromyography and kinesiology*, 16(6):541–548.

[Parker and Scott, 1985] Parker, P. A. and Scott, R. (1985). Myoelectric control of prostheses. *Critical reviews in biomedical engineering*, 13(4):283–310.

[Patel and Mehta, 2012] Patel, V. R. and Mehta, R. G. (2012). Data clustering: integrating different distance measures with modified k-means algorithm. In *Proceedings of the International Conference on Soft Computing for Problem Solving (SocProS 2011) December 20-22, 2011*, pages 691–700. Springer.

[Pelleg et al., 2000] Pelleg, D., Moore, A. W., et al. (2000). X-means: Extending k-means with efficient estimation of the number of clusters. In *ICML*, pages 727–734.

[Pfurtscheller et al., 2003] Pfurtscheller, G., Graimann, B., Huggins, J., Levine, S., and Schuh, L. (2003). Spatiotemporal patterns of beta desynchronization and gamma synchronization in corticographic data during self-paced movement. *Clinical Neurophysiology*, 114(7):1226 – 1236.

[Pistohl et al., 2012] Pistohl, T., Schulze-Bonhage, A., Aertsen, A., Mehring, C., and Ball, T. (2012). Decoding natural grasp types from human ecog. *Neuroimage*, 59(1):248–260.

[Plow et al., 2010] Plow, E. B., Arora, P., Pline, M. A., Binenstock, M. T., and Carey, J. R. (2010). Within-limb somatotopy in primary motor cortex–revealed using fmri. *Cortex*, 46(3):310–321.

[Popovic et al., 2001] Popovic, M., Curt, A., Keller, T., and Dietz, V. (2001). Functional electrical stimulation for grasping and walking: indications and limitations. *Spinal Cord*, 39(8):403–412.

[Rabiner, 1989] Rabiner, L. R. (1989). A tutorial on hidden markov models and selected applications in speech recognition. *Proceedings of the IEEE*, 77(2):257–286.

[Rasmussen et al., 2001] Rasmussen, A., Matsuura, T., Ruano, L., Yescas, P., Ochoa, A., Ashizawa, T., and Alonso, E. (2001). Clinical and genetic analysis of 4 mexican families with spinocerebellar ataxia type 10. *Annals of neurology*, 50(2):234–239.

[Robinson et al., 1978] Robinson, D. L., Goldberg, M. E., and Stanton, G. B. (1978). Parietal association cortex in the primate: sensory mechanisms and behavioral modulations. *Journal of neurophysiology*, 41(4):910–932.

[Rokni et al., 2007] Rokni, U., Richardson, A. G., Bizzi, E., and Seung, H. S. (2007). Motor learning with unstable neural representations. *Neuron*, 54(4):653–666.

[Royer et al., 2010] Royer, A. S., Doud, A. J., Rose, M. L., and He, B. (2010). Eeg control of a virtual helicopter in 3-dimensional space using intelligent control strategies. *Neural Systems and Rehabilitation Engineering, IEEE Transactions on*, 18(6):581–589.

[Rubinov and Sporns, 2010] Rubinov, M. and Sporns, O. (2010). Complex network measures of brain connectivity: Uses and interpretations. *NeuroImage*, 52(3):1059 – 1069. Computational Models of the Brain.

[Sakata and Taira, 1994] Sakata, H. and Taira, M. (1994). Parietal control of hand action. *Current opinion in neurobiology*, 4(6):847–856.

[Sanchez et al., 2012] Sanchez, J. C., Erdogmus, D., Nicolelis, M. A., Wessberg, J., and Principe, J. C. (2012). Spinal Cord Injury Facts and Figures at a Glance.

[Saur et al., 2008] Saur, D., Kreher, B. W., Schnell, S., Kümmerer, D., Kellmeyer, P., Vry, M.-S., Umarova, R., Musso, M., Glauche, V., Abel, S., et al. (2008). Ventral and dorsal pathways for language. *Proceedings of the national academy of Sciences*, 105(46):18035–18040.

[Scarborough et al., 1977] Scarborough, D. L., Cortese, C., and Scarborough, H. S. (1977). Frequency and repetition effects in lexical memory. *Journal of Experimental Psychology: Human perception and performance*, 3(1):1.

[Schacter et al., 1991] Schacter, D. L., Cooper, L. A., Delaney, S. M., Peterson, M. A., and Tharan, M. (1991). Implicit memory for possible and impossible objects: constraints on the construction of structural descriptions. *Journal of Experimental Psychology: Learning, Memory, and Cognition*, 17(1):3.

[Schalk et al., 2008] Schalk, G., Miller, K., Anderson, N., Wilson, J., Smyth, M., Ojemann, J., Moran, D., Wolpaw, J., and Leuthardt, E. (2008). Two-dimensional movement control using electrocorticographic signals in humans. *Journal of neural engineering*, 5(1):75.

[Scherberger et al., 2005] Scherberger, H., Jarvis, M. R., and Andersen, R. A. (2005). Cortical local field potential encodes movement intentions in the posterior parietal cortex. *Neuron*, 46(2):347–354.

[Schieber, 2001] Schieber, M. H. (2001). Constraints on somatotopic organization in the primary motor cortex. *Journal of neurophysiology*, 86(5):2125–2143.

[Schieber and Hibbard, 1993] Schieber, M. H. and Hibbard, L. S. (1993). How somatotopic is the motor cortex hand area? *Science*, 261(5120):489–492.

[Schöls et al., 1997] Schöls, L., Amoiridis, G., Büttner, T., Przuntek, H., Epplen, J. T., and Riess, O. (1997). Autosomal dominant cerebellar ataxia: phenotypic differences in genetically defined subtypes? *Annals of neurology*, 42(6):924–932.

[Schöls et al., 2008] Schöls, L., Linnemann, C., and Globas, C. (2008). Electrophysiology in spinocerebellar ataxias: spread of disease and characteristic findings. *The cerebellum*, 7(2):198–203.

[Schwartz, 2004] Schwartz, A. B. (2004). Cortical neural prosthetics. *Annu. Rev. Neurosci.*, 27:487–507.

[Schwartz et al., 2006] Schwartz, A. B., Cui, X. T., Weber, D., and Moran, D. W. (2006). Brain-controlled interfaces: Movement restoration with neural prosthetics. *Neuron*, 52(1):205 – 220.

[Schwartz et al., 2001] Schwartz, A. B., Taylor, D. M., and Tillery, S. I. H. (2001). Extraction algorithms for cortical control of arm prosthetics. *Current opinion in Neurobiology*, 11(6):701–708.

[Scott and Dorcas, 1966] Scott, R. and Dorcas, D. (1966). A three-state myoelectric control system. *Med Biol Eng*, 4:367.

[Scott and Parker, 1988] Scott, R. and Parker, P. (1988). Myoelectric prostheses: state of the art. *Journal of medical engineering & technology*, 12(4):143–151.

[Sinai et al., 2005] Sinai, A., Bowers, C. W., Crainiceanu, C. M., Boatman, D., Gordon, B., Lesser, R. P., Lenz, F. A., and Crone, N. E. (2005). Electrocorticographic high gamma activity versus electrical cortical stimulation mapping of naming. *Brain*, 128(7):1556–1570.

[Singh and Chauhan, 2011] Singh, S. S. and Chauhan, N. (2011). K-means v/s k-medoids: A comparative study. In *National Conference on Recent Trends in Engineering & Technology*, volume 13.

[Slonim et al., 2005] Slonim, N., Atwal, G. S., Tkačik, G., and Bialek, W. (2005). Information-based clustering. *Proceedings of the National Academy of Sciences of the United States of America*, 102(51):18297–18302.

[Smith et al., 2008] Smith, R. J., Tenore, F., Huberdeau, D., Cummings, R. E., and Thakor, N. V. (2008). Continuous decoding of finger position from surface emg signals for the control of powered prostheses. In *Engineering in Medicine and Biology Society, 2008. EMBS 2008. 30th Annual International Conference of the IEEE*, pages 197–200. IEEE.

[Smith et al., 2011] Smith, S. M., Miller, K. L., Salimi-Khorshidi, G., Webster, M., Beckmann, C. F., Nichols, T. E., Ramsey, J. D., and Woolrich, M. W. (2011). Network modelling methods for fmri. *Neuroimage*, 54(2):875–891.

[Sneath et al., 1973] Sneath, P. H., Sokal, R. R., et al. (1973). *Numerical taxonomy. The principles and practice of numerical classification.*

[Song et al., 2009] Song, L., Kolar, M., and Xing, E. P. (2009). Time-varying dynamic bayesian networks. In *Advances in Neural Information Processing Systems*, pages 1732–1740.

[Srinivasan et al., 1998] Srinivasan, R., Nunez, P. L., and Silberstein, R. B. (1998). Spatial filtering and neocortical dynamics: estimates of eeg coherence. *Biomedical Engineering, IEEE Transactions on*, 45(7):814–826.

[Stark and Abeles, 2007] Stark, E. and Abeles, M. (2007). Predicting movement from multiunit activity. *The Journal of neuroscience*, 27(31):8387–8394.

[Stephenson and Zelen, 1989] Stephenson, K. and Zelen, M. (1989). Rethinking centrality: Methods and examples. *Social Networks*, 11(1):1–37.

[Strehl et al., 2000] Strehl, A., Ghosh, J., and Mooney, R. (2000). Impact of similarity measures on web-page clustering. In *Workshop on Artificial Intelligence for Web Search (AAAI 2000)*, pages 58–64.

[Su and Chou, 2001] Su, M.-C. and Chou, C.-H. (2001). A modified version of the k-means algorithm with a distance based on cluster symmetry. *IEEE Transactions on Pattern Analysis & Machine Intelligence*, (6):674–680.

[Sugata et al., 2014] Sugata, H., Hirata, M., Yanagisawa, T., Shayne, M., Matsushita, K., Goto, T., Yorifuji, S., and Yoshimine, T. (2014). Alpha band functional connectivity correlates with the performance of brain–machine interfaces to decode real and imagined movements. *Frontiers in human neuroscience*, 8.

[Sun et al., 2015] Sun, H., Blakely, T. M., Darvas, F., Wander, J. D., Johnson, L. A., Su, D. K., Miller, K. J., Fetz, E. E., and Ojemann, J. G. (2015). Sequential activation of premotor, primary somatosensory and primary motor areas in humans during cued finger movements. *Clinical Neurophysiology.*

[Tanji, 2001] Tanji, J. (2001). Sequential organization of multiple movements: Involvement of cortical motor areas. *Annual Review of Neuroscience*, 24(1):631–651. PMID: 11520914.

[Taylor et al., 2002] Taylor, D. M., Tillery, S. I. H., and Schwartz, A. B. (2002). Direct cortical control of 3d neuroprosthetic devices. *Science*, 296(5574):1829–1832.

[Theys et al., 2015] Theys, T., Romero, M. C., van Loon, J., and Janssen, P. (2015). Shape representations in the primate dorsal visual stream. *Frontiers in Computational Neuroscience*, 9(43).

[Thier and Erickson, 1992] Thier, P. and Erickson, R. (1992). Responses of visual-tracking neurons from cortical area mst-i to visual, eye and head motion. *European Journal of Neuroscience*, 4(6):539–553.

[Towle et al., 2008] Towle, V. L., Yoon, H.-A., Castelle, M., Edgar, J. C., Biassou, N. M., Frim, D. M., Spire, J.-P., and Kohrman, M. H. (2008). Ecog gamma activity during a language task: differentiating expressive and receptive speech areas. *Brain*, 131(8):2013–2027.

[Trouillas et al., 1997] Trouillas, P., Takayanagi, T., Hallett, M., Currier, R., Subramony, S., Wessel, K., Bryer, A., Diener, H., Massaquoi, S., Gomez, C., et al. (1997). The ataxia neuropharmacology committee of the world federation of neurology. international cooperative ataxia rating scale for pharmacological assessment of the cerebellar syndrome. *J Neurol Sci*, 145(2):205–211.

[Tulving and Schacter, 1990] Tulving, E. and Schacter, D. L. (1990). Priming and human memory systems. *Science*, 247(4940):301–306.

[Ungerleider and Mishkin, 1982] Ungerleider, L. and Mishkin, M. (1982). Analysis of visual behavior.

[Van Bogaert and Szliwowski, 1996] Van Bogaert, P. and Szliwowski, H. (1996). Eeg findings in acetazolamide-responsive hereditary paroxysmal ataxia. *Neurophysiologie Clinique/Clinical Neurophysiology*, 26(5):335–340.

[van den Broek et al., 1998] van den Broek, S. P., Reinders, F., Donderwinkel, M., and Peters, M. (1998). Volume conduction effects in eeg and meg. *Electroencephalography and clinical neurophysiology*, 106(6):522–534.

[Van Den Heuvel and Pol, 2010] Van Den Heuvel, M. P. and Pol, H. E. H. (2010). Exploring the brain network: a review on resting-state fmri functional connectivity. *European Neuropsychopharmacology*, 20(8):519–534.

[Varela et al., 2001] Varela, F., Lachaux, J.-P., Rodriguez, E., and Martinerie, J. (2001). The brainweb: phase synchronization and large-scale integration. *Nature reviews neuroscience*, 2(4):229–239.

[Vargas-Irwin et al., 2010] Vargas-Irwin, C. E., Shakhnarovich, G., Yadollahpour, P., Mislow, J. M., Black, M. J., and Donoghue, J. P. (2010). Decoding complete reach and grasp actions from local primary motor cortex populations. *The Journal of Neuroscience*, 30(29):9659–9669.

[Velliste et al., 2008] Velliste, M., Perel, S., Spalding, M. C., Whitford, A. S., and Schwartz, A. B. (2008). Cortical control of a prosthetic arm for self-feeding. *Nature*, 453(7198):1098–1101.

[Von Luxburg, 2007] Von Luxburg, U. (2007). A tutorial on spectral clustering. *Statistics and computing*, 17(4):395–416.

[Von Luxburg, 2010] Von Luxburg, U. (2010). *Clustering stability: an overview*. Now Publishers Inc.

[Wang et al., 2009] Wang, W., Degenhart, A. D., Collinger, J. L., Vinjamuri, R., Sudre, G. P., Adelson, P. D., Holder, D. L., Leuthardt, E. C., Moran, D. W., Boninger, M. L., Schwartz, A. B., Crammond, D. J., Tyler-Kabara, E. C., and Weber, D. J. (2009). Human motor cortical activity recorded with Micro-ECoG electrodes, during individual finger movements. *Conf Proc IEEE Eng Med Biol Soc*, 2009:586–589.

[Wang et al., 2016] Wang, Y., Fifer, M. S., Flinker, A., Korzeniewska, A., Cervenka, M. C., Anderson, W. S., Boatman-Reich, D. F., and Crone, N. E. (2016). Spatial-temporal functional mapping of language at the bedside with electrocorticography. *Neurology*, 86(13):1181–1189.

[Wasserman and Faust, 1994] Wasserman, S. and Faust, K. (1994). *Social network analysis: Methods and applications*, volume 8. Cambridge university press.

[Whang et al., 2015] Whang, J. J., Lenharth, A., Dhillon, I. S., and Pingali, K. (2015). Scalable data-driven pagerank: Algorithms, system issues, and lessons learned. In *Euro-Par 2015: Parallel Processing*, pages 438–450. Springer.

[Wilke et al., 2009] Wilke, C., Van Drongelen, W., Kohrman, M., and He, B. (2009). Identification of epileptogenic foci from causal analysis of ecog interictal spike activity. *Clinical Neurophysiology*, 120(8):1449–1456.

[Wilke et al., 2011] Wilke, C., Worrell, G., and He, B. (2011). Graph analysis of epileptogenic networks in human partial epilepsy. *Epilepsia*, 52(1):84–93.

[Wise et al., 1997] Wise, S. P., Boussaoud, D., Johnson, P. B., and Caminiti, R. (1997). Premotor and parietal cortex: Corticocortical connectivity and combinatorial computations 1. *Annual review of neuroscience*, 20(1):25–42.

[Wu and Hatsopoulos, 2007] Wu, W. and Hatsopoulos, N. G. (2007). Coordinate system representations of movement direction in the premotor cortex. *Experimental brain research*, 176(4):652–657.

[Wuerker et al., 1965] Wuerker, R. B., McPhedran, A. M., and Henneman, E. (1965). Properties of motor units in a heterogeneous pale muscle (m. gastrocnemius) of the cat. *Journal of neurophysiology*, 28(1):85–99.

[Yazdan-Shahmorad et al., 2013] Yazdan-Shahmorad, A., Kipke, D. R., and Lehmkuhle, M. J. (2013). High gamma power in ecog reflects cortical electrical stimulation effects on unit activity in layers v/vi. *Journal of neural engineering*, 10(6):066002.

[Young et al., 2011] Young, A. J., Hargrove, L. J., Kuiken, T., et al. (2011). The effects of electrode size and orientation on the sensitivity of myoelectric pattern recognition systems to electrode shift. *Biomedical Engineering, IEEE Transactions on*, 58(9):2537–2544.

[Young et al., 2012] Young, A. J., Hargrove, L. J., Kuiken, T., et al. (2012). Improving myoelectric pattern recognition robustness to electrode shift by changing interelectrode distance and electrode configuration. *Biomedical Engineering, IEEE Transactions on*, 59(3):645–652.

[Young et al., 2013] Young, A. J., Smith, L. H., Rouse, E. J., and Hargrove, L. J. (2013). Classification of simultaneous movements using surface emg pattern recognition. *Biomedical Engineering, IEEE Transactions on*, 60(5):1250–1258.

[Young et al., 2014] Young, A. J., Smith, L. H., Rouse, E. J., and Hargrove, L. J. (2014). A comparison of the real-time controllability of pattern recognition to conventional myoelectric control for discrete and simultaneous movements. *J Neuroeng Rehabil*, 11(5).

[Žalik, 2008] Žalik, K. R. (2008). An efficient k-means clustering algorithm. *Pattern Recognition Letters*, 29(9):1385–1391.

[Zasorin et al., 1983] Zasorin, N., Baloh, R., and Myers, L. (1983). Acetazolamide-responsive episodic ataxia syndrome. *Neurology*, 33(9):1212–1212.

[Zelnik-Manor and Perona, 2004] Zelnik-Manor, L. and Perona, P. (2004). Self-tuning spectral clustering. In *Advances in neural information processing systems*, pages 1601–1608.

[Zhao et al., 2009] Zhao, Q., Zhang, L., and Cichocki, A. (2009). Eeg-based asynchronous bci control of a car in 3d virtual reality environments. *Chinese Science Bulletin*, 54(1):78–87.

[Ziegler-Graham et al., 2008] Ziegler-Graham, K., MacKenzie, E. J., Ephraim, P. L., Travison, T. G., and Brookmeyer, R. (2008). Estimating the prevalence of limb loss in the united states: 2005 to 2050. *Archives of physical medicine and rehabilitation*, 89(3):422–429.

[Zipser et al., 1996] Zipser, K., Lamme, V. A., and Schiller, P. H. (1996). Contextual modulation in primary visual cortex. *The Journal of Neuroscience*, 16(22):7376–7389.

©2011 IEEE. Reprinted, with permission, from Ying, S.H., Newman, G.I., Choi, Y-S., Kim, H-N, Presacco, A., Kothare, M.V., Thakor, N.V., "Cerebellar ataxia patients are able to use motor imagery to modulate mu-band power in a pilot study of EEG-based brain-computer interface control." Neural Engineering (NER), 2011 5th International IEEE/EMBS Conference, pp. 192–195, Apr. 2011.

©2011 IEEE. Reprinted with permission, from Newman, G.I., Aggarwal, V., Schieber, M.H., Thakor, N.V., "Identifying neuron communities during a reach and grasp task using an unsupervised clustering analysis." Engineering in Medicine and Biology Society, EMBC, 2011 Annual International Conference of the IEEE, pp. 6401–6404, Sep. 2011.

©2015 IEEE. Reprinted with permission, from Newman, G.I., Fifer, M., Benz, H., Crone, N., Thakor, N.V., "Eigenvector centrality reveals the time course of task-specific electrode connectivity in human ECoG." Neural Engineering (NER), 2015 7th International IEEE/EMBS Conference, pp. 336–339, Feb. 2015.

In reference to IEEE copyrighted material which is used with permission in this thesis, the IEEE does not endorse any of Johns Hopkins University's products or services. Internal or personal use of this material is permitted. If interested in reprinting/republishing IEEE copyrighted material for advertising or promotional purposes or for creating new collective works for resale or redistribution, please go to http://www.ieee.org/publications_standards/publications/rights/rights_link.html to learn how to obtain a License from RightsLink.

Vita

Geoffrey Newman was born in 1985 in Bronxville, New York. He went to high school at the Bronx High School of Science in the Bronx. Due to his extensive Advanced Placement coursework, he received the AP Scholar with Distinction award. Concurrent with that, he attended the College Now program at Lehman college where he accumulated 18 credits worth of college level classes. Upon acceptance into the biomedical engineering program, he received a Whitaker Foundation Full Scholarship with a research stipend to attend City College of New York, a member university of the City University of New York. He graduated with a Bachelor's in Engineering Magna Cum Laude in 2008. During his time at City College, Geoffrey was actively engaged in peer-led team learning, leading a total of five semesters' workshops in Chemistry 101 and 102. Eventually Geoffrey helped develop lesson plans and instruct small groups of workshop leaders in their implementation. Geoffrey additionally received a Howard Hughes Undergraduate Award for his research in eye-movement under Dr. Jay Edelman of the

Department of Neuroscience. Geoffrey matriculated into the Johns Hopkins University Biomedical Engineering Ph.D. program in 2008, where he began his research into brain-machine interface and network analysis with neural signals. At the time of this dissertation's submission, Geoffrey has been an author on one peer-reviewed journal publications, one manuscript in submission, six conference papers, and seven conference abstracts. Geoffrey will begin work in October in Pittsburgh at a technology company named Qeexo, where he will have the role of machine learning engineer.